University of Nottingham
UK | CHINA | MALAYSIA

TWO-PHASE FLUID INTERFACIAL INSTABILITIES INDUCED BY AXISYMMETRIC ROTATION UNDER THE INFLUENCE OF AN EXTERNALLY APPLIED MAGNETIC FIELD

Submitted 30th March 2022, in partial fulfillment of
the conditions for the award of the degree **Doctor of Philosophy.**

Bobby Clement[†]
14309386

Supervised by
Matthew M. Scase[†]
Richard J. Hill[††]

School of Mathematical Science[†]
University of Nottingham

School of Physics and Astronomy[††]
University of Nottingham

I hereby declare that this dissertation is all my own work, except as indicated in the text.

I hereby declare that I have all necessary rights and consents to publicly distribute this dissertation via the University of Nottingham's e-dissertation archive.

30th March 2022

Abstract

In this thesis, we discuss the use of a superconducting solenoid magnet to investigate radial interfacial instabilities between two rotating immiscible, incompressible fluids of differing density. The magnetic field produced by the solenoid magnet is used to induce a radial body force on diamagnetic and paramagnetic fluids, providing an effective acceleration in the radial direction that affect the instability growth rate at the interface. The applied rotation is then controlled to induce instability for various wavenumbers, analogous with horizontal gravitational instability. The investigation is focused on a circular Hele-Shaw cell containing two fluids of non-equal density that occupy a small gap between two solid flat plates.

An experimental study is carried out by varying the angular velocity on the two-fluid system at a vertical equilibrium point in the magnetic field. The magnetic force creates an initial condition in which the more dense fluid occupies an inner circular region of a rotating circular cell, centred on the axis, while the less dense fluid occupies the outer region. Under rotation, both fluid layers experience a centripetal acceleration directed towards the axis, causing Rayleigh-Taylor instability to develop.

We were able to extract and analyse the interface between the fluid layers to determine the growth rates for increasing wavenumbers and determine the fastest growth rate. We then derived a linear growth model by approximating a highly viscous three-dimensional Stokes flow to a two-dimensional potential flow problem by taking a depth-averaged velocity over the vertical distance of our experimental cell. The model also allowed us to determine a critical angular velocity for which instability occurs. Comparisons of the fastest growing wavenumber between the model and our experimental results showed a qualitative agreement between the two. The dynamic viscosity of the fluid layers in our experiments caused a quantitative difference in our results, leading us to investigate different viscosity values. By setting the viscosity as an unknown parameter and employing non-linear curve fitting, the viscosity of both fluids layers were found to be

greater than anticipated. However, we were able to show experimentally that the excitation of wavenumbers can be influenced by the angular velocity of the system.

Acknowledgements

"Ask yourself. Will you step, or will you leap?"
– Master Chief Petty Officer John-117

First and foremost, I would like to thank my supervisors, Dr. Matthew M. Scase and Dr. Richard J. Hill, for their unwavering support and guidance throughout this work. Their expertise have been invaluable in my development as a researcher. Dr. Hill's guidance helped me to understand the experimental techniques needed for our experiments in this thesis and they are skills which will be carried forward throughout my career. Dr. Scase's tutelage in fluid dynamics has been a key part of my research development; always ensuring that I am clear, concise and unambiguous in my work. A special mention to Dr. Naresh Sampara for their ideas to improve my experimental technique. Their knowledge and experience has helped me in more ways than one, developing my thought process with regards to experimental intuition.

I could not have performed the experiments in this work without the support of the technical team building the apparatus. In particular, I thank the numerous conversations with Thomas Napier and David Laird. Their inputs helped to develop the final design specification for my experimental process.

I would also like to thank my partner, Dr. Ting-Yun Cheng, for allowing me to vent my frustrations and listen to my ramblings even when neither of us understood what I was saying. Their support throughout this process has been tremendous, and I struggle to find words to express my gratitude. Finally, my mother and father continued to believe that I will succeed, even when I kept telling them my difficulties. I would not be here if I didn't have the drive derived from my family.

Contents

Chapter 1

Introduction

The stability of equilibria at an interface between two fluids may be characterised as either stable, unstable or neutrally stable. If the system undergoes an initial perturbation to the interface, then the equilibrium position is characterised as stable if the amplitude of all wavenumbers of the perturbation decay in time, returning to its initial condition. On the other hand, the equilibrium position is characterised as unstable if at least one wavenumber of the perturbation is unstable, and the perturbation begins to grow exponentially in time. Throughout this work, the wavenumber is used to mean 'angular wavenumber', the spatial frequency of a wave, and is related to wavelength by

$$m = \frac{2\pi}{\lambda},$$

where m is the wavenumber with wavelength λ. A neutrally stable interface is one which, when perturbed, neither returns to its initial steady state, nor grows in time.

A fluid-fluid interface can exhibit complex interfacial instabilities when given a small disturbance. A common method to investigate the behaviour and evolution of such an interface is linear stability analysis. This method is limited to the early stage development of interfacial instability on a system initially in equilibrium,

but one that may shed light on the growth rate of perturbations and determine the most unstable wavelength.

We begin by giving an overview of interfacial instabilities and the motivations behind their study. A historical account from Lord Rayleigh and G. I. Taylor is given, along with a literature review of previous work and motivations with some examples of applications in industry and research. This is then followed by a summary of the thesis content.

1.1 Historical Background

The stability of density stratified fluids has been the topic of much discussion since the late 19th century. Most notably related to the present discussion are the works of Lord Rayleigh (1842-1919) and G. I. Taylor (1886-1975). Rayleigh first derived the properties of density-difference-driven interfacial instability in his 1882 paper titled 'Investigation of the character of the equilibrium of an incompressible heavy fluid of variable density' [33], concerning a dense incompressible fluid supported by a less dense incompressible fluid under the influence of gravity, in horizontal strata. He proved that the interface is always unstable.

Taylor's work [53] generalised the foundations of Rayleigh by noting that the same instability also arises when the system is accelerated in the direction from a less dense (light) fluid to a more dense (heavy) fluid. He considered a horizontal fluid-fluid interface, similar to that in Rayleigh's study, but assumed the configuration to be gravitationally stable. By introducing an additional vertical acceleration, g_1, Taylor derived stability conditions acting co-linearly with gravity. He concluded that a gravitationally stable configuration is unstable if the net vertical acceleration is greater in magnitude and acts anti-parallel than that of gravity. The theoretical derivations and analysis were successfully verified by experimental work carried out by Lewis [31] in a channel-flow geometry. A dia-

gram illustrating Taylor's findings is given in figure 1.1 demonstrating the effect of an additional acceleration.

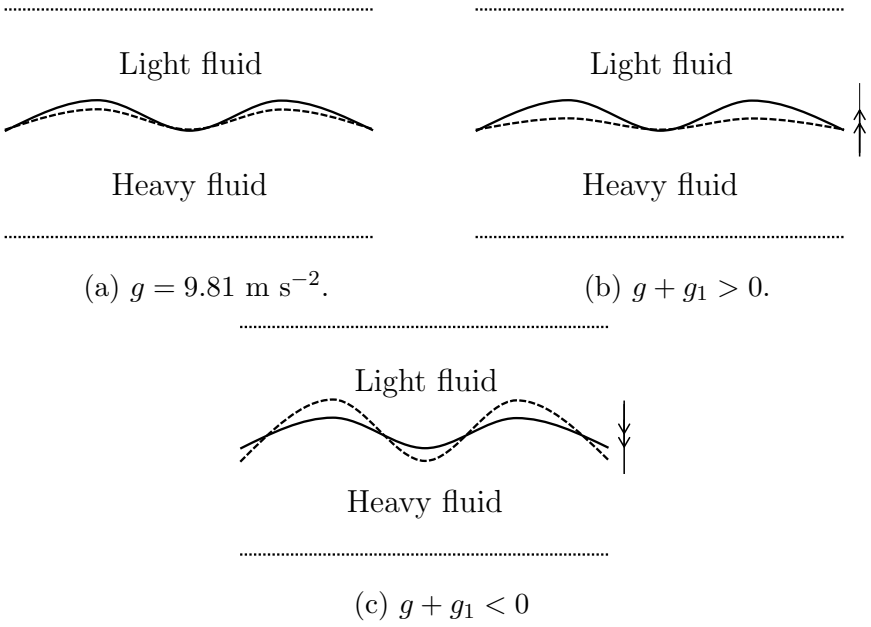

(a) $g = 9.81$ m s^{-2}. (b) $g + g_1 > 0$.

(c) $g + g_1 < 0$

Figure 1.1: Illustration of Taylor's analysis where g is the acceleration of gravity and the double arrows show the direction of effective acceleration in the system. (a) Under gravity only, the system is not accelerating and the interface is in stable equilibrium. When perturbed (solid black line), the disturbance decays in time (dashed line) (b) A vertical acceleration g_1 is applied, using the same symbol for an additional acceleration as Taylor for clarity [53]. g_1 is directed upwards, such that $g_1 > 0$, and the interface stabilises a faster rate than in (a). (c) Perturbations to the interface start to grow in time as the applied acceleration is greater than that of gravity, with $|g_1| > |g|$ and $g_1 < 0$, inducing instability. The dotted lines indicate fluid layer bounds which may be unbounded to neglect effects from a boundary.

The research of both Rayleigh [33] and Taylor [53] combine to describe what is commonly referred to as the Rayleigh-Taylor Instability (RTI); some authors refer to this as Taylor instability.

A good description of RTI is given by Sharp [49], describing the behaviour of a layer of water uniformly plastered against a ceiling in a room. An air layer fails to support the water layer as it fails to maintain flatness of the air-water interface, giving rise to small disturbances (figure 1.2). Any disturbances will increase in magnitude as the air layer fails to support the nonuniform pressure distribution in the water layer.

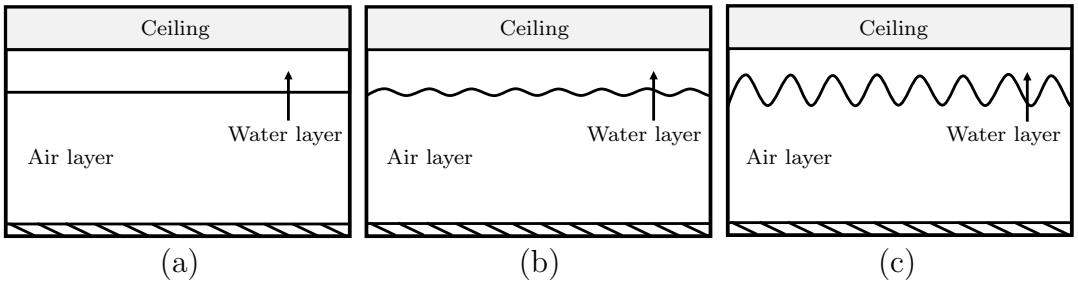

Figure 1.2: Figure reconstructed from Figure 1 in [49]. (a) Air pressure supports a perfectly flat water layer. (b) Air pressure can not keep flatness of air-water interface, so small disturbances will be present. (c) The disturbances grow exponentially in time

A typical example of where RTI can be observed is when making a cup of tea with milk. Milk is more dense than water due to the inclusion of other substances such as proteins and sugars. If milk is poured slowly into a cup of black tea, the instability of Rayleigh-Taylor type can be observed in the formation of 'finger-like' columns. This effect occurs shortly before mixing, as a result of fluid miscibility.

1.2 Motivations and a planar experiment under rotation

In this theses we investigate interfacial instabilities present in density stratified systems which are initially in an unstable configuration. Density stratified instabilities are important in understanding multi-phase flows within many areas of research from the small scale modelling of inertial confinement fusion, to the very large scale modelling of exploding helium stars [20] and supernovae remnants [41, 43].

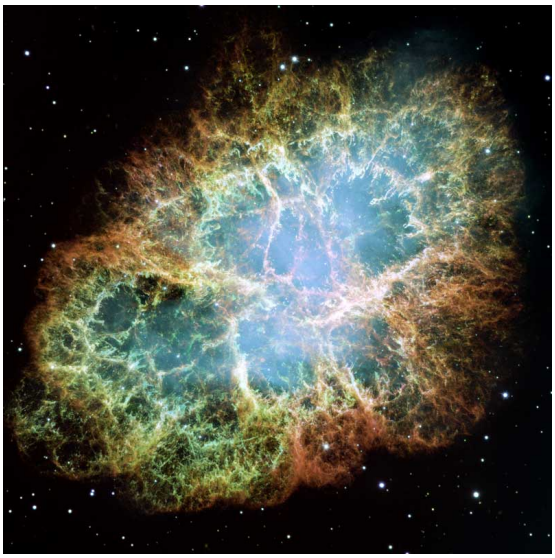

Figure 1.3: Rayleigh-Taylor instability fingers can be observed in the Crab nebula. An expanding supernova remnant of a supernova event recorded by astronomers nearly 1000 years ago. Credit: Hubble Heritage[1]

Interfacial instability can be a hindrance in some technologies. For example, in inertial confinement fusion, a cavity known as a 'hohlraum' is heated by lasers and the resulting x-rays irradiate an outer layer of material surrounding a spherical fuel pellet. The process for inertial confinement fusion is outlined by figure 1.4. Rayleigh-Taylor instabilities can be observed during an implosion stage where the surrounding material is ablated causing a "rocket-like blowoff", compressing the fuel in the centre. The ablation of the material is not a spherically symmetric process. This causes nonuniformity in the temperature of the outer material. The "blowoff" is, consequently, nonuniform and perturbations develop, which grow in time. The presence of the instability reduces the efficiency of the compression stage due to the increased surface area of the interface [7, 45].

On the other hand, some instabilities can be beneficial. A beneficial example can be seen in the process to induce mixing, causing two fluids of differing densities to form a homogenised combination of the two. An example process uses Kelvin-Helmholtz shearing instability, which occur upon a discontinuity in velocity at

[1] https://hubblesite.org/

the interface, inducing a mixing stage [26].

There are different types of fluid-fluid instability, but the instability of greatest relevance to us throughout this thesis is the Rayleigh-Taylor instability.

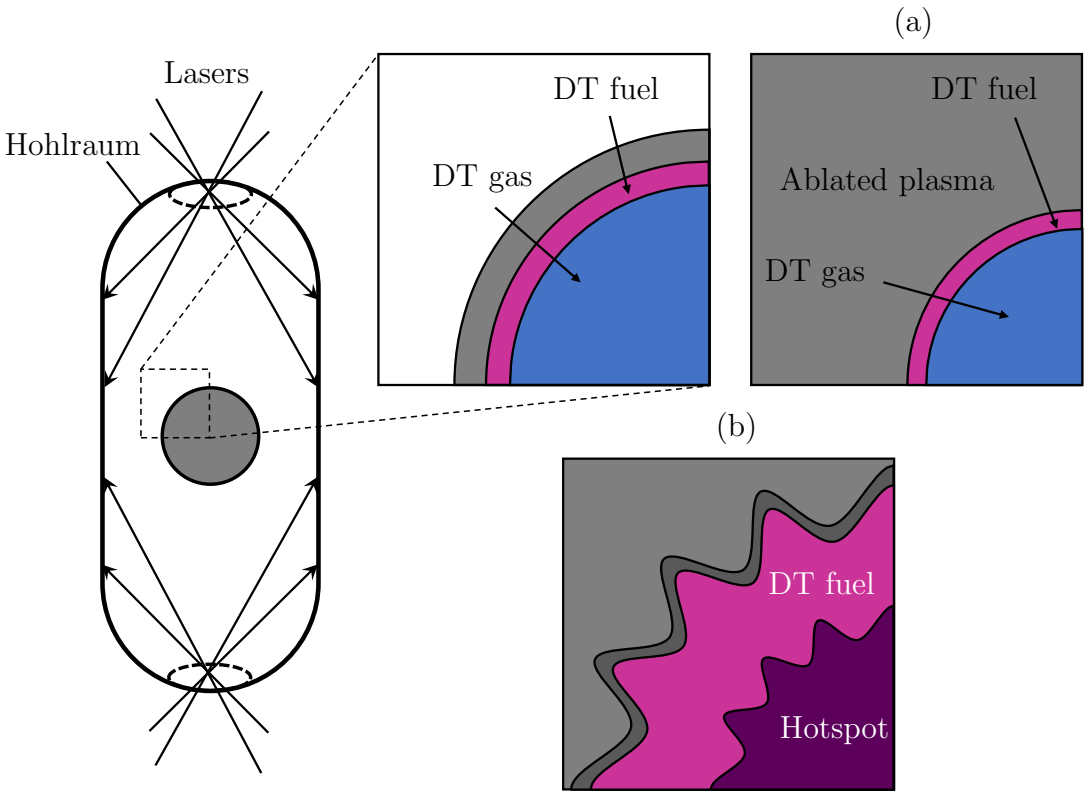

Figure 1.4: Process of inertial confinement fusion by 'indirect drive'. Lasers heat a cavity inside a 'hohlraum', causing radiation to heat the pellet surface. (a) The heat causes the surface to implode. (b) An asymmetric surface forms from a 'hotspot' of DT (Deuterium) being surrounded by colder and denser DT fuel. Image adapted from R. Betti *et al.* [7]

There have been several attempts to study density-driven instabilities experimentally, such as recent experiments by Scase *et al.* [45]. They investigated density-driven Rayleigh-Taylor instabilities by using an external magnetic field to apply a vertical body force to the fluids to induce instability of an otherwise stable configuration in horizontal strata. They were able to verify that the effect of rotation about a vertical axis inhibits the growth rate of perturbations and were able to determine a critical rotation rate for which perturbations are suppressed.

Figure 1.5: Experimental results performed by Baldwin *et al.* [2]. The left image is the RTI development without rotation, while the right image is with rotation. Both images are taken from the complimentary theoretical paper by Scase *et al.* [45]. The time stamps are 1.1 s and 1.2 s respectively, after the onset of instability, showing that rotation inhibits the growth of the instability as well as affecting the wavelength of perturbations.

A supplementary experiment was performed to show the effect of viscosity while keeping a fixed rotation rate at $\Omega \approx 7.8$ rad s^{-1}. By adding glycerol to each fluid layer, the viscosity varied from $\mu = 1.00 \times 10^{-2}$ g cm^{-1}s^{-1} to $\mu = 26.73 \times 10^{-2}$ g cm^{-1}s^{-1}. The observed wavelengths of the structures increased from $\lambda \approx 6$ mm to $\lambda > 17$ mm, respectively, verifying that the effect of viscosity was the suppression of small-scale structures, leading to larger observed structures for increasing viscosity. Applying the effects of rotation resulted in larger structures being suppressed, while smaller structures were suppressed by viscosity.

1.3 Hele-Shaw flow experiments

In addition to RTI in planar geometry, as studied by Rayleigh [33] and Taylor [53], there are many examples in which RTI develops in systems with spherical symmetry such as inertial confinement fusion and supernovae, as described in section 1.2. Experimental studies of RTI at a fluid-fluid interface in spherical geometry can be difficult due to the difficulty of maintaining spherical symmetry throughout the experiment in the presence of gravity. Hence, researchers have

turned to studying interfacial instability in circular symmetry, in a Hele-Shaw cell, which is simpler experimentally, in order to shed light on the spherical case [1, 8, 11].

1.3.1 Hele-Shaw cell geometry

Suppose we have a fluid of density ρ and dynamic viscosity η flowing between two parallel flat plates, separated by a small gap b, see figure 1.6 illustrating a fluid with unidirectional flow, $U(\mathbf{r})$ with $\mathbf{r}$ as the position vector, constrained between two flat plates. The fluid flow between the parallel flat plates is Stokes flow and is termed Hele-Shaw flow. Our work will involve a horizontally aligned Hele-Shaw cell. The aspect ratio describing the relative size of the vertical cell domain compared with the horizontal cell domain is $\varepsilon = b/L \ll 1$, where L is the horizontal length scale of the Hele-Shaw cell. The small gap characteristic allows an averaged velocity to be taken over the vertical direction so that an initially three-dimensional problem may be effectively regarded as two-dimensional. This simplifies the theoretical approach considerably to satisfy two-dimensional potential equations; a more detailed discussion is given in chapter 6.

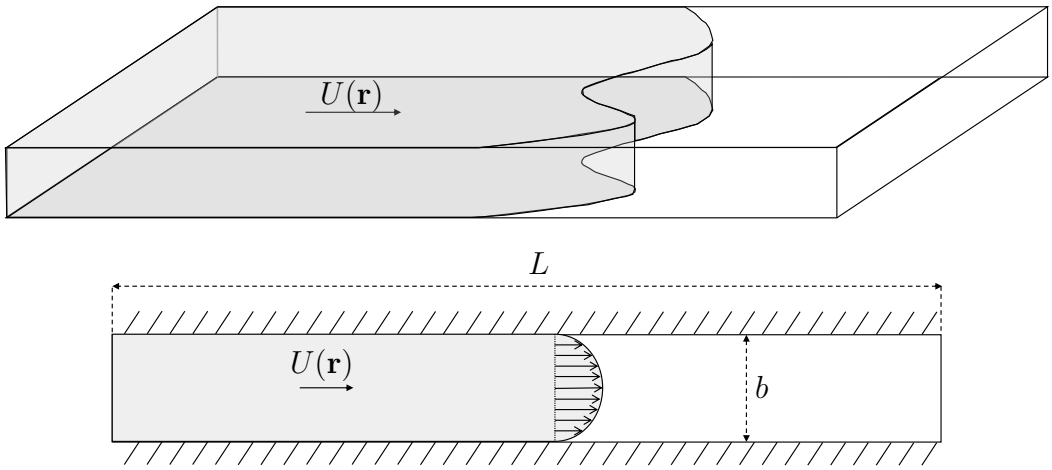

Figure 1.6: Hele-Shaw channel flow with a local parabolic velocity field at the leading edge in the vertical direction. The small gap is characterised by a dimensionless parameter, defined as $\varepsilon = b/L \ll 1$.

1.3.2 Review of experiments on Hele-Shaw flows

Carrillo *et al.* [11] performed experiments using an oil-air interface to investigate instability in Hele-Shaw cells under rotation, i.e. under radial acceleration. Their motivation was to determine the role of the viscosity contrast in the dynamics of radial instabilities in Hele-Shaw cells. They injected an initial volume of oil through a syringe pump located at the centre of a circular cell to an initial radius R_0, as seen in figure 1.7. The outer cell boundary was left open to ambient air leading to a volume of oil being surrounded by air, meaning that their study focused on a high viscosity contrast system. The cell was then rotated to a specified angular velocity. Under rotation, the fluids experienced a centripetal acceleration directed towards the centre of the cell, from air to oil. This resulted in a density-difference-driven instability which is described by RTI. In the study, they performed two variations of the experiment: one without an injection flow rate, $Q = 0$, to maintain mass conservation, and the other with a flow rate, $Q \neq 0$, where mass was no longer conserved.

In the linear regime, where the amplitude of the disturbance is less than or similar to their wavelength in magnitude, they found that there was a discrepancy in the predicted growth of some wavenumbers between experiments with and without mass conservation. They concluded that, with mass conservation, the discrepancy came from the growth of perturbations with smaller wavenumbers being enhanced during the time taken for the cell to reach the specified rotational speed. By the time the specified speed was reached, the enhanced-growth wavenumbers variably dominated over the predicted most unstable wavenumber. This effect was reduced, but still present, when mass was no longer conserved in the oil phase such that $Q \neq 0$.

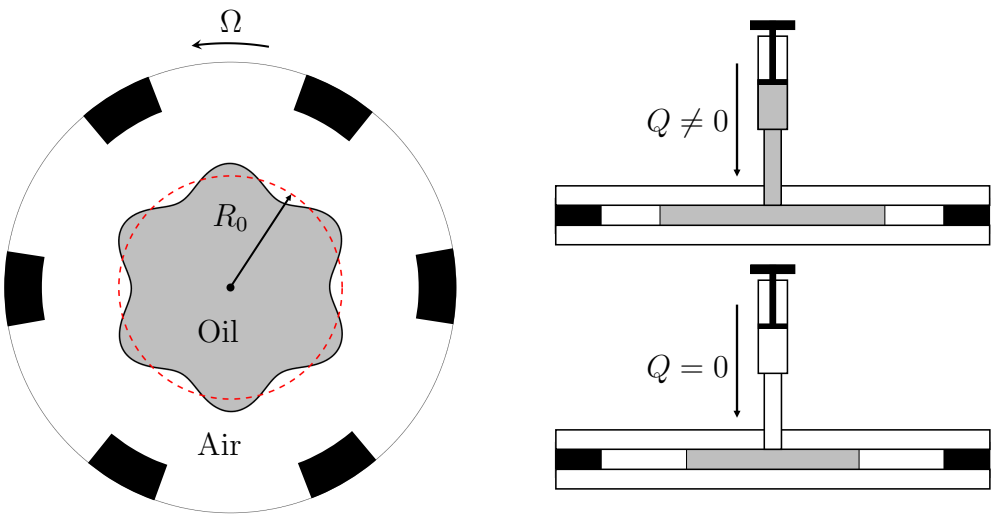

(a) Top view. (b) Side view.

Figure 1.7: A simplified diagram of the cell used in experiments by Carrillo *et al.* [11]. (a) Top view of a circular Hele-Shaw cell with six equispaced spacers separating the two glass discs. Oil occupies the inner region while air is allowed to escape from the open boundary. (b) Side view of both experimental variations. Both situations exhibit an angular velocity with one increasing the mass of oil in the cell such that $Q \neq 0$, and the other with the mass kept constant such that $Q = 0$.

Work done by Alvarez-Lacalle *et al.* [1] built upon Carrillo *et al.* [11] by determining the role of low viscosity contrast between the fluid layers in the dynamics of instability. Their work looked at the nonlinear regime of finger growth, as illustrated in figure 1.8, where the amplitude of the fingers exceeds their lateral size. In the linear regime, experimental verification of the dispersion relation remained uncertain, as there was difficulty in counting the number of fingers present at the end of the experiment. In the nonlinear regime for high viscosity contrast flows, dynamical competition between fingers of differing sizes resulted in a reduction in the number of fingers present. Whereas, low viscosity contrast flows suppressed this behaviour. With this, they were able to match the number of fingers at the end of the experiment with the number of fingers observed at the end of the linear regime, within a 5% error, allowing for the verification of linear stability predictions.

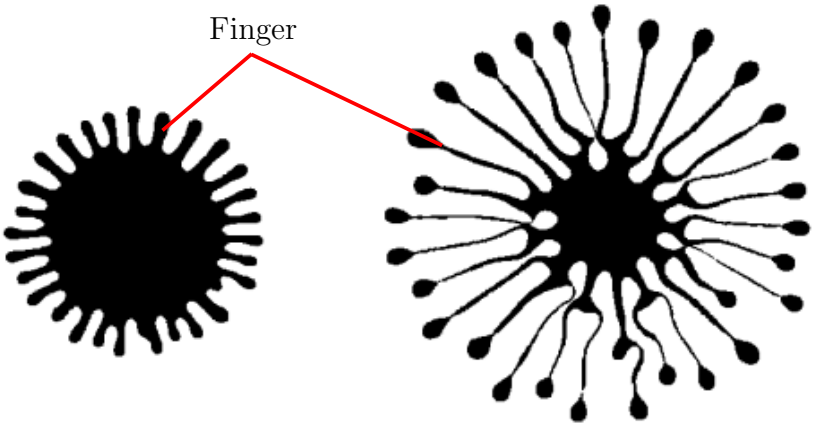

Figure 1.8: Simulation of nonlinear regime for an oil-oil interface with low viscosity contrast, courtesy of Alvarez *et al.* [1]. The long, thin lobes of the instability are typically termed as 'fingers'.

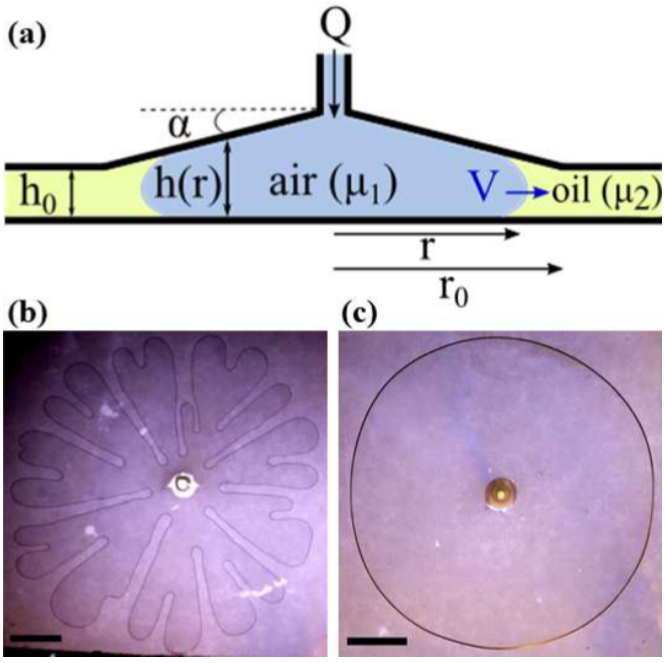

Figure 1.9: Figure and caption taken from G. Bongrand and P. A. Tsai [8]. (a) Schematic diagram of the side view of experimental setup. (b) A snapshot of viscous fingering obtained from air pushing oil in a flat radial Hele-Shaw cell with injection flow rate $Q = 40$ mL/min. (c) A snapshot of the same setup as (b) but the Hele-shaw cell is tapered radially by $\alpha = -6.67 \times 10^{-2}$ radians to the horizontal.

In 2018 an experimental investigation performed by Bongrand and Tsai [8] focused on a method of reducing instabilities in a large viscosity contrast system. The system involved an oil-air interface, similar to Carillo *et al.* [10]. In contrast, however, their cell was initially occupied by oil, with air later injected through a syringe pump at the centre. The instability was induced by injecting air through a syringe with flow rate Q, with the cell remaining stationary such that the angular velocity denoted by Ω is zero. The increasing volume of air was accelerated radially towards the oil phase where perturbations form and grow in time. They looked at the effect of tapering the cell on unstable growth by reducing the gap thickness radially from the centre. Using this design, they found complete suppression of viscous fingering with a suitable flow rate. A schematic of the setup used by Bongrand and Tsai is given in figure 1.9.

The works presented here give an insight into the experimental procedure carried out by previous authors to understand radial fluid instabilities for both low and high viscosity contrasts under radial acceleration. Our objective is to carry out a new experimental technique by using a magnetic field to induce a radial body force on a two-fluid system in a circular Hele-Shaw cell. The magnetic field will provide an opposing body force to the radial acceleration induced by rotation that will affect the instability growth rate at the interface. The rotation rate is then varied to induce instability for various wavenumbers, This experimental technique will also allow for experimental repeatability as the magnetic field will force the fluids to return to their initial state before rotation is applied.

This thesis aims to experimentally verify linear dispersion relations for unstable growth which may lay the foundations for future work into interfacial instabilities for spherical geometries under the influence of an external magnetic field.

1.4 Hydrodynamical simulation overview of interfacial instability

Analytical solutions in fluid dynamics are difficult to formulate, often involving substantial simplifications to the governing model, due to their highly non-linear and coupled nature. In most cases, modelling a the full flow field is split into different regions where different scales are used. An important example is that of flow past a flat plate, figure 1.10. In the outer region, the flow is assumed unidirectional and, in the simplest of cases, inviscid as the inertial momentum is dominant. However, close to the flat plate (the boundary layer), viscous drag becomes a non-negligible component, even dominating the inertia terms. These two regions have differing analytical solutions. It is then in the best interest of the modeller to match the boundary conditions between the outer flow and the boundary layer, completing the picture of the flow field.

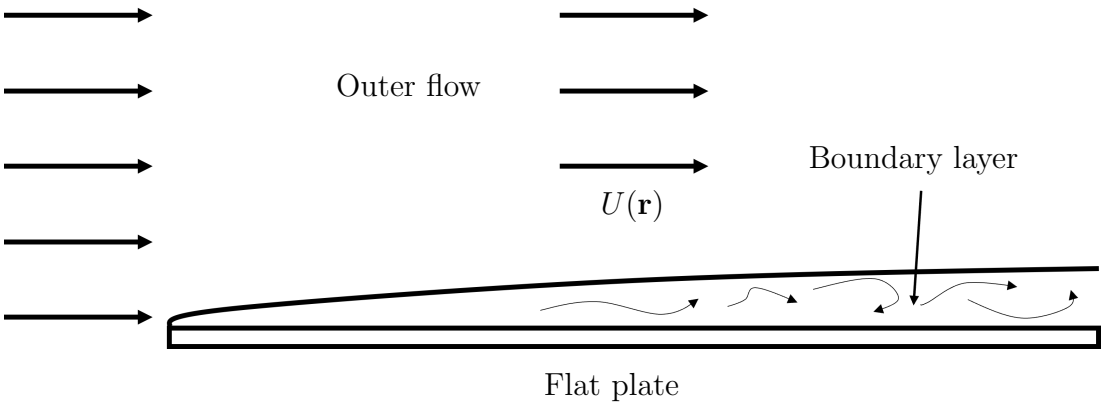

Figure 1.10: Flow past a flat plate. The uniform flow $U(\mathbf{r})$ approaches the leading edge of a flat plate. The flow field is then split into two region, a continuous uniform outer flow and a turbulent boundary layer close to the flat plate.

Although steps can be taken to find analytical solutions of fluid flow, there are still underlying assumptions being made to help find solutions. However, through the aid of numerical simulations, progress can be made to capture the true dynamics of a flow. This is an ongoing field of research and there are a vast number of examples in the realm of Computational Fluid Dynamics (CFD), covering a

wide range of problems. CFD also offer insights into the mechanisms of flow which would otherwise not be attainable through experimental study. Therefore, the application of CFD is an important tool to complement experiments.

Related to this work are simulations involved with fluid-fluid interfacial dynamics. There are a variety of numerical methods employed to tackle this problem. Krüger *et al.* [28] compared some numerical schemes which are appropriate for deformable interfaces. They also discuss the limitations of such algorithms in order for the reader to be aware when applying to their own work. For example, in the case of the 'immersed boundary method', it is discussed that the method is simple to implement as a deformable particle scheme, but has problems when modelling a rigid boundary. The method is in the class of interface tracking methods and is typically used when an additional material forms the interface, but can be used for the case of immiscible flows. As a 'front-tracking' algorithm, the interface is assumed to have zero thickness and is formed or particles represented by nodes. The approach is to then track the dynamics of these nodes as it moves through a mesh representing the fluid.

In comparison with interface tracking methods, there are volume tracking methods. One such example is the Volume of Fluid (VOF) method. This is a widely used method within the CFD community as it is has been tested extensively and compared with experimental results [19, 34]. For incompressible flow, this method makes use of the conservation of mass, which is analogous to the conservation of volume, to track the fluid volume as it interacts with the environment.

A powerful numerical method, especially in the case of two-dimensional geometries, is the Boundary Element Method (BEM). This techniques is favourable over other more traditional CFD methods as it reduces a problem by one dimension [23]. For density stratified flows, this method can offer greater accuracy over volume tracking methods. However, for density ratios closer to unity, the accuracy

of the method degrades, suggesting other numerical methods as a choice for more accurate results

We provided a short overview of a number non-exhaustive numerical methods. In each case there are advantages and disadvantages to their use dependent on the particular situation of their use. In this work, we do not offer an investigation into any particular numerical approach, opting to focus on an experimental study. It is then appropriate to consider the inclusion of this work to offer aid in the investigation of improved numerical simulations.

1.5 Thesis outline

In chapter 2, we discuss the effect that magnetic forces can have on fluids and define a material property known as the 'volume magnetic susceptibility'. A brief description of diamagnetism is given and the conditions for radial stability in a solenoid magnet are derived. As the fluids are restricted vertically, stability in this direction is not important as the effect of gravity on the system are removed by positioning the experimental cell at an 'equilibrium point' in the magnetic field, making the fluids effectively weightless. We will then provide the necessary tools to appropriately model the magnetic body force on fluids with small volume magnetic susceptibility and derive the relevant Cauchy momentum equation.

Chapter 3 describes the experimental procedure and methodology used. The procedure is described in full and our experimental results are given and discussed. The methods used to analyse the data acquired from the previous chapter are the topic in chapter 4. A description of the image processing techniques employed is given, along with the steps taken to reduce erroneous results occurring from artefacts from data acquisition.

In chapter 5 and 6 we introduce the theoretical tools used to predict linear stability growth rates of unstable wavenumbers. A two-dimensional inviscid analysis

is first given, and chapter 6 is the final step in developing the theoretical model used to compare experimental results. A lubrication model is used to derive the Hele-Shaw approximation. We then compare and discuss this model with the experimental results obtained in chapter 4. Chapter 7 provides a summary of the key results and discussion of future work is given.

Chapter 2

Magnetism body forces

This chapter provides an overview of magnetic body forces and their application in fluid dynamics. Though there exist many types of magnetism, the present discussion is limited to the effects of diamagnetism and paramagnetism. Both effects are much weaker forms of magnetism than the more commonly known ferromagnetism, and are the forms of magnetism present in this work.

A brief description of the physics of diamagnetism and paramagnetism are first provided. Then by following the work of Berry and Geim [6], a derivation of the magnetic body force on an object are given. Following this, we discuss the use of diamagnetic forces to balance the force of gravity under an externally applied magnetic field. We then discuss how the same body forces can be similarly applied to exert a radial body force. The conditions for radial stability are then derived for diamagnetic fluids, which are later utilised to set an initially stable fluid-fluid configuration in our experiments. The magneto-Archimedes principle is introduced and we show how this principle applies to the radial stability of two-fluid systems to show how radial stability can be extended to objects when submersed in a medium of non-equal magnetic susceptibility. Lastly, a brief description of superconducting magnets is given to give context to the experimental equipment used.

2.1 Diamagnetism and paramagnetism

Diamagnetism and paramagnetism are magnetic properties of all ordinary materials, including fluids, which result from the electronic configuration of the atoms and molecules of the material. Electrons have a magnetic dipole associated with them due to both their orbital motion and their 'spin'. As the dipole moments are, in general, randomly oriented, the net dipole moment of the material is zero. Ferromagnetic materials on the other hand, can possess a non-zero magnetic moment even in the absence of an external magnetic field. This 'special' form of magnetism is perhaps more familiar but since it is not relevant to this thesis we will not discuss it further here.

In a diamagnetic material, the spins of the electrons in the material are paired parallel and anti-parallel so that only the orbital motion of electrons contribute to the magnetism. When a magnetic field is applied to a diamagnetic material, a magnetic dipole moment is induced in it which opposes that of the externally applied magnetic field (Lenz's law [17]).

In a paramagnetic material on the other hand, the spin of electrons are not all paired parallel and antiparallel. The spin magnetic moment dominates that of the orbital moment. A paramagnetic material placed in an external magnetic field develops a net magnetic moment in the same direction as the externally-applied field. Diagrams of the magnetic field produced by the electron is shown in figure 2.1, while figure 2.2 shows the electron configuration of a diamagnetic and paramagnetic atom

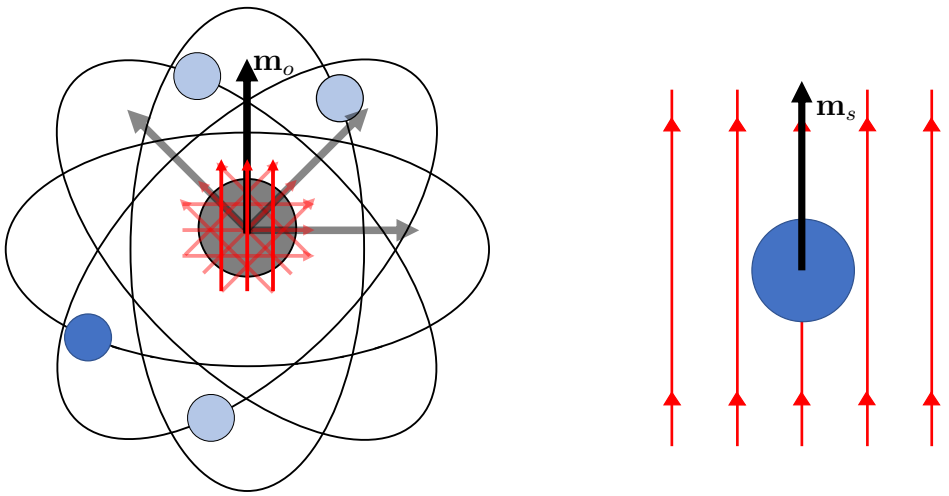

(a) (b)

Figure 2.1: (a) A stylised diagram of the magnetic field produced from electron orbits. Electrons orbit the nuclei of atoms, shown by the grey circle in the centre, causing a magnetic field from the movement of its negative charge. A magnetic dipole moment (dark arrows), $\mathbf{m}_o$, is produced with magnetic field indicated by the red arrows. The random motion of the electrons cancel the magnetic dipole moments. The blue circles represent a stylised representation of electron motion in its orbit. (b) The electron is a point particle producing its own magnetic dipole moment, $\mathbf{m}_s$, from its 'spin', a quantum mechanical effect not discussed here.

The property we exploit here is that paramagnetic materials are weakly *attracted* by a magnetic field, whereas a diamagnetic material is weakly *repelled* by a magnetic field. This force is proportional to the volume magnetic susceptibility χ, a property of the material. Also important to this work is the fact that both paramagnetic and diamagnetic forces are *body forces,* that is to say that they act throughout the body of the material, as the force of gravity does.

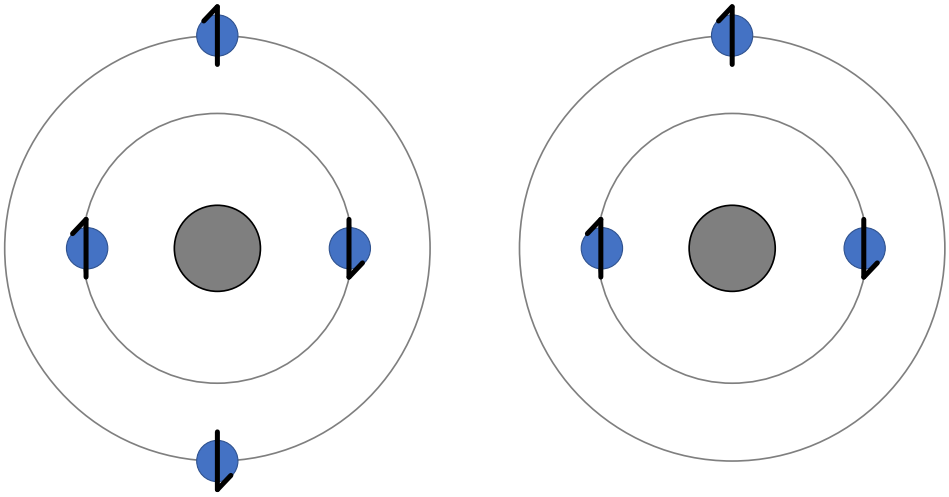

(a) (b)

Figure 2.2: (a) Bohr's atomic model showing the electron configuration for a diamagnetic material. Each electron is part of an electron pair. The net magnetic dipole moments from each electron spin is zero. The notation used on each electron shows the type of spin exhibited by each electron. In this example, each pair exhibit 'spin-up' and 'spin-down', corresponding to the 'spin' component direction. See Feynman *et al.* for a robust description of atomic spin [18]. (b) Electron configuration for a paramagnetic material. There is an unpaired electron present. This will give a net spin in the atom and a magnetic dipole moment which aligns with an external magnetic field. The vertical black lines on the electrons represent the two types of spin an electron can exhibit.

2.2 Magnetic body forces

In this thesis, we show how the magnetic body forces on paramagnetic and diamagnetic fluids can be used to apply radial body forces on fluids confined to a Hele-Shaw cell. We first, however, discuss a more well-known application of such body forces in a strong magnetic field, which is to balance the force of gravity in order to *levitate* materials. This is to derive necessary conditions for vertical stability which will be essential in the coming chapters. Such levitation experiments typically require magnetic fields of order ~ 10 T (Tesla), generated by a superconducting solenoid magnet, or a 'Bitter' magnet [6]. The diagram in figure 2.3 shows the magnetic field generated by a superconducting solenoid.

The work of Berry *et al.* [6] is followed to find equilibrium points for stability. An externally applied magnetic field is used to achieve this by acting on an object located within the field. In this work, the magnetic field inside a solenoid is the external magnetic field under discussion. For simplicity, we refer to the magnetic field inside a solenoid as the 'solenoid magnet'. Figure 2.3 shows a diagram of the solenoid magnet as well as the shape of its magnetic field lines.

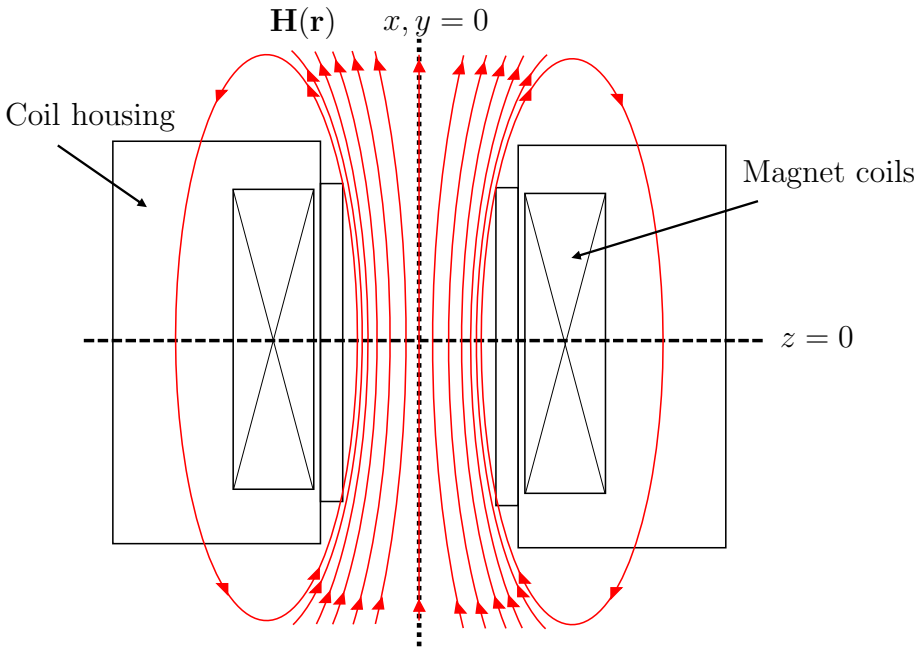

Figure 2.3: Cross-sectional diagram of the magnetic field $\mathbf{H}(\mathbf{r})$, and its field lines used in this work, where $\mathbf{r}$ is a position vector in the respective coordinate system. The red lines are the magnetic field lines. The magnet is cylindrical in shape and axisymmetric about the centre axis. The magnet coils are superconducting materials, discussed in section 2.4, allowing for a high magnetic field to be generated.

By considering the potential energy of an object from gravity and the solenoid magnet, the magnetic body force can be derived and the criteria for radial stability can be given.

2.2.1 The balance of gravity

In this section we derive equations for the body force acting on a diamagnetic or paramagnetic material in a magnetic field. The derivation here closely follows that of Berry and Geim. [6].

The point at which force due to gravity is balanced by a magnetic field can depend upon various parameters such as the magnitude of volume magnetic susceptibility, as well as properties such as density, temperature and volume. For a positive magnetic susceptibility, $\chi > 0$, the material is said to be paramagnetic. That is to say, the magnetic dipole moments from the electrons in the material align with the externally applied magnetic field inducing an attractive force. Conversely, for negative magnetic susceptibility, $\chi < 0$, the material is said to be diamagnetic. This is when the magnetic dipole moments are directed against the externally applied magnetic field and so feel a repulsive force. The alignment of the magnetic dipole moment is represented for groups of atoms in figure 2.4.

Let us assume an isothermal system and consider the total potential energy held by an object under the influence of an externally applied magnetic field, in a gravitational field. The magnetic induction vector field, $\mathbf{B}(\mathbf{r})$, with units Tesla (T), is defined as

$$\mathbf{B}(\mathbf{r}) = \mu_0(\mathbf{H}(\mathbf{r}) + \mathbf{M}(\mathbf{r})),$$

where we use cylindrical polar coordinates (r, θ, z) with basis vectors $\mathbf{e}_r$, $\mathbf{e}_\theta$, and $\mathbf{e}_z$ respectively. Here, r and z are as defined in figure 2.3 and θ is the azimuthal angle. The vector field $\mathbf{H}(\mathbf{r})$ is the externally applied magnetic field (i.e. the field generated by the solenoid magnet) and $\mathbf{M}(\mathbf{r})$ is the magnetisation of the material within the field, i.e. the magnetic moment per unit volume. $\mu_0 = 4\pi \times 10^{-7}$ N A^{-2} is the magnetic permeability of free space, with units Newtons (N) per square Ampère (A). The $\mathbf{B}(\mathbf{r})$ field can thus be thought of as the total magnetic field; the magnetic field generated by the solenoid plus the magnetic field generated by

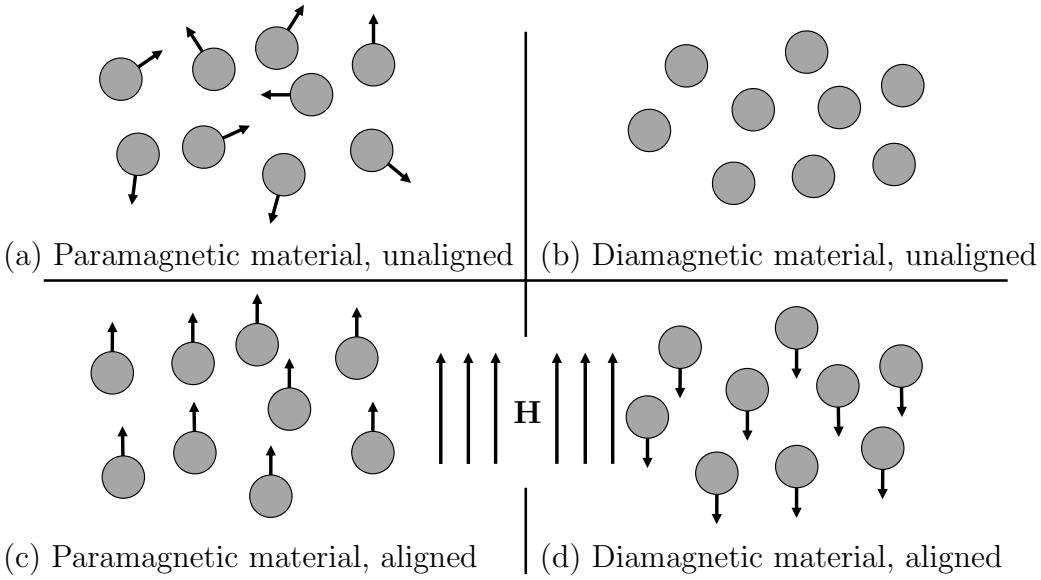

(a) Paramagnetic material, unaligned (b) Diamagnetic material, unaligned

(c) Paramagnetic material, aligned (d) Diamagnetic material, aligned

Figure 2.4: Diagram of magnetic dipole moment alignment when subjected to an externally applied field $\mathbf{H}(\mathbf{r})$. The grey circles represent an atom. (a) and (c), magnetic dipole moments exist in a material from unpaired electrons. The $\mathbf{H}(\mathbf{r})$ field aligns the magnetic dipole moments parallel to field. (b) and (d), magnetic dipole moments are cancelled in the material from averaged effect of electron motion. The $\mathbf{H}(\mathbf{r})$ field induces magnetic dipole moments antiparallel to field as a consequence of Lenz's law.

the magnetisation of the object.

For diamagnetic and paramagnetic materials, the magnetisation holds a linear relationship with $\mathbf{H}(\mathbf{r})$ [44]. Written in terms of the volume magnetic susceptibility χ, we have

$$\mathbf{M}(\mathbf{r}) = \chi \mathbf{H}(\mathbf{r}). \tag{2.1}$$

For paramagnetic materials, $\chi > 0$, whereas for diamagnetic materials, $\chi < 0$.

The linearity of magnetisation with an external magnetic field allows the magnetic induction vector to be written as

$$\mathbf{B}(\mathbf{r}) = \mu_0(1 + \chi)\mathbf{H}(\mathbf{r}). \tag{2.2}$$

In the experiments presented here, the volume magnetic susceptibility is small, of order $|\chi| \sim 10^{-5}$. Therefore, this relationship is well-approximated as

$$\mathbf{B}(\mathbf{r}) = \mu_0 \mathbf{H}(\mathbf{r}). \tag{2.3}$$

The induced magnetic dipole moment, on an object of volume V, is then given by

$$\mathbf{m}(\mathbf{r}) = \frac{\chi V}{\mu_0} \mathbf{B}(\mathbf{r}), \tag{2.4}$$

which is used to determine the magnetic potential energy of the object in the external magnetic field by integrating the work done, as given in Berry and Geim [6]. For consistency with Berry *et al.* [6], we use Cartesian coordinates with $\mathbf{r} = (x, y, z)$ unless otherwise specified.

The gravitational potential energy is denoted by $U_g(z)$ and given as

$$U_g(z) = \rho g z V, \tag{2.5}$$

where ρ is the constant density of an object of volume V, z is the vertical coordinate and $g = 9.81$ m s^{-2} is acceleration due to gravity. Adding the gravitational potential energy to the magnetic potential energy gives the total potential energy as [6]

$$U(\mathbf{r}) = \rho V g z - \frac{\chi V}{2\mu_0} B^2(\mathbf{r}), \tag{2.6}$$

where $B(\mathbf{r}) = |\mathbf{B}(\mathbf{r})|$ is the strength of the magnetic induction field and ρV is the mass of the object with volume V. The net force on the object is then given by the gradient of the potential energy as

$$\mathbf{F}(\mathbf{r}) = -\boldsymbol{\nabla} U(\mathbf{r}) = -\rho g V \mathbf{e}_z + \frac{\chi}{2\mu_0} V \boldsymbol{\nabla} B^2(\mathbf{r}), \tag{2.7}$$

where the first term represents the gravitational force on the object and the second term represents the magnetic force acting on an object.

Beaugnon and Tournier [5] demonstrated that, given a sufficiently strong magnetic field $B(\mathbf{r})$, and sufficiently large field gradient, $\boldsymbol{\nabla} B(\mathbf{r})$, organic materials and water ($\chi \sim -9 \times 10^{-6}$) could be levitated in stable equilibrium at a point in the magnetic field where these two terms balance, i.e. where $\mathbf{F}(\mathbf{r}) = 0$, and where there is a local minimum (a 'well') in the potential energy $U(\mathbf{r})$. By taking the components of (2.7), the equilibrium points are when

$$\mathbf{e}_x : \quad \frac{\partial}{\partial x} B^2(\mathbf{r}) = 0, \tag{2.8}$$

$$\mathbf{e}_y : \quad \frac{\partial}{\partial y} B^2(\mathbf{r}) = 0. \tag{2.9}$$

$$\mathbf{e}_z : \quad -\rho g + \frac{\chi}{2\mu_0} \frac{\partial}{\partial z} B^2(\mathbf{r}) = 0, \tag{2.10}$$

Equations (2.8) and (2.9) can only be satisfied when $B(\mathbf{r}) = f(z)$, showing that the equilibrium point is dependent on z. As the magnetic field is symmetric about the z-axis, the equilibrium point must also exist along the z-axis. By rearranging (2.10) we see that the equilibrium point satisfies the condition

$$B(0,0,z) \left. \frac{\partial}{\partial z} B(\mathbf{r}) \right|_{\substack{x=0 \\ y=0}} = \frac{\rho}{\chi} g \mu_0. \tag{2.11}$$

The equilibrium condition is independent of an object's volume, depending only on the ratio between magnetic susceptibility, density, and the acceleration of gravity. As might be anticipated, for small susceptibilities, $|\chi| \ll 1$, the magnetic field gradient must be large for (2.11) to be satisfied. In the case of water, with $\chi_{water} \approx -9.04 \times 10^{-6}$ [29], and density $\rho_{water} \approx 998$ kg m^{-3} [22] at 20°C , the magnitude of the left hand side of (2.11) must be approximately 1290 T^{2}m^{-1}; it requires a powerful magnet to balance gravity for dense, weakly magnetic objects.

To illustrate the location of the equilibrium points, we use the example of water levitating in a vacuum. Figure 2.5 shows the equilibrium points along the axis of the magnetic field where (2.11) is satisfied. We can see that the equilibrium points lie above the centre of the solenoid magnet that is located at $z = 0$. It is

impossible to balance the force due to gravity below the centre of a solenoid for the example provided due to the diamagnetic nature of water. It is *repelled* by the magnetic field, so below $z = 0$ the magnetic force acts to 'push' the water away from the region of high field strength, directed vertically down. The force of gravity also acts in this direction, without significant opposing forces resisting the downward motion. Therefore, the equilibrium positions, if they exist, for all diamagnetic objects, are located above $z = 0$. As shown, there are two points for vertical equilibrium. To understand the stability of these points, we must consider some additional criteria.

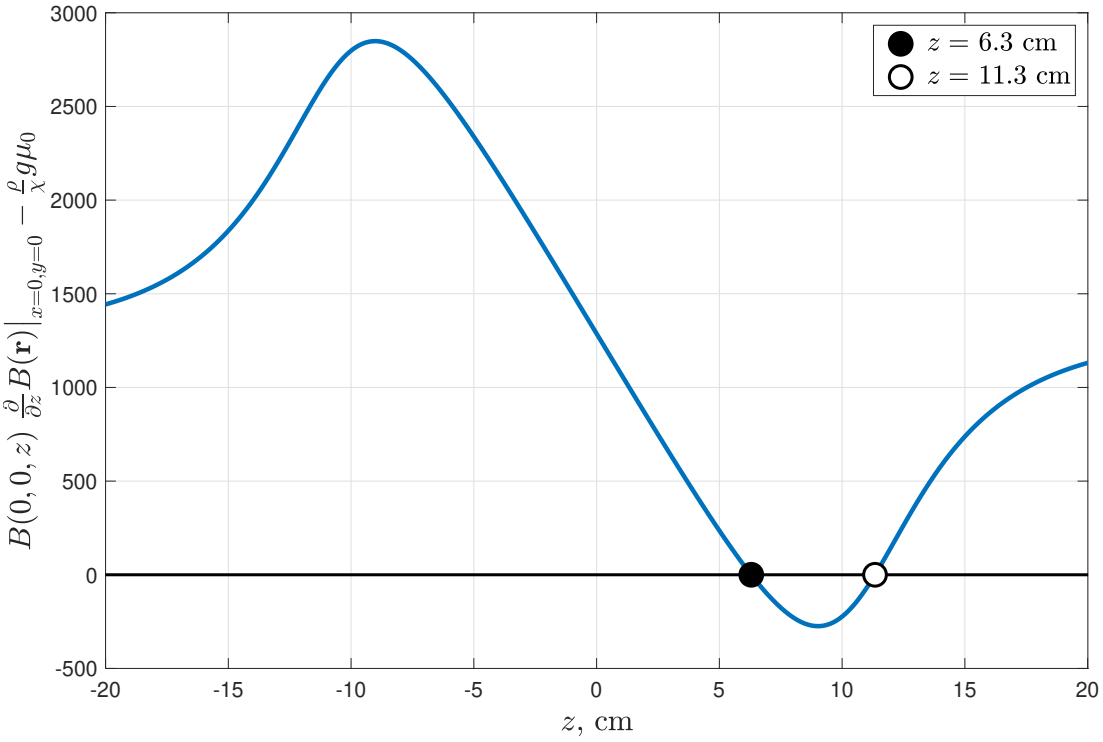

Figure 2.5: Equilibrium positions in the magnet bore with a central field strength $B(0,0) = 18.5$ T for a water droplet surrounded by air. The force due to gravity is balanced along the vertical centre axis when $z = 6.3$ cm and $z = 11.3$ cm.

2.2.2 Criterion for radial stability of diamagnetic volumes

The equilibrium points given by equation (2.11) give the locations where the force of gravity and magnetism on an object are balanced. The stability of the equilibria are determined by the integral over a closed surface surrounding each

equilibrium point [6]. A stable equilibrium point must satisfy the necessary condition

$$\iint_S \mathbf{F}(\mathbf{r}) \cdot \mathrm{d}\mathbf{S} < 0, \tag{2.12}$$

where S is a small surface enclosing an equilibrium point. This condition is necessary for free levitation. We will continue to discuss this here in detail as the derivation also yields the sufficient condition for radial stability, which is directly relevant to the present work. By the divergence theorem, and (2.7), the potential energy must satisfy

$$\nabla^2 U(\mathbf{r}) > 0, \tag{2.13}$$

which can be written in a more intuitive form, in terms of the magnitude of the magnetic induction field, as

$$-\chi \nabla^2 B^2(\mathbf{r}) > 0. \tag{2.14}$$

The stability condition fails to hold for paramagnetic materials, $\chi > 0$, as we must satisfy

$$\nabla^2 B^2(\mathbf{r}) < 0, \tag{2.15}$$

which is not possible as we show below [6]. Expanding the left hand side of (2.15), we find

$$\begin{aligned}\nabla^2 B^2(\mathbf{r}) = 2\big\{ &|\boldsymbol{\nabla} B_{\mathbf{e}_x}|^2 + |\boldsymbol{\nabla} B_{\mathbf{e}_y}|^2 + |\boldsymbol{\nabla} B_{\mathbf{e}_z}|^2 \\ &+ B_{\mathbf{e}_x} \nabla^2 B_{\mathbf{e}_x} + B_{\mathbf{e}_y} \nabla^2 B_{\mathbf{e}_y} + B_{\mathbf{e}_z} \nabla^2 B_{\mathbf{e}_z} \big\}, \end{aligned} \tag{2.16}$$

where $B(\mathbf{r}) = |\mathbf{B}(\mathbf{r})|$, $B_{\mathbf{e}_x} = B_{\mathbf{e}_x}(\mathbf{r})$, $B_{\mathbf{e}_y} = B_{\mathbf{e}_y}(\mathbf{r})$ and $B_{\mathbf{e}_z} = B_{\mathbf{e}_z}(\mathbf{r})$. We may further simplify (2.16) by using the Ampère-Maxwell law

$$\boldsymbol{\nabla} \wedge \mathbf{B}(\mathbf{r}) = \mu_0 \mathbf{J}(\mathbf{r}), \tag{2.17}$$

where $\mathbf{J}(\mathbf{r})$ is the electric current density. However, inside the solenoid magnet, there are no free electric currents so there is zero current density, $\mathbf{J}(\mathbf{r}) = \mathbf{0}$. The magnetic induction field is, therefore, irrotational, where the time independent Ampère-Maxwell law becomes

$$\boldsymbol{\nabla} \wedge \mathbf{B}(\mathbf{r}) = \mathbf{0}. \tag{2.18}$$

Using Maxwell's divergence free equation, $\boldsymbol{\nabla} \cdot \mathbf{B} = 0$, the vector identity

$$\nabla^2 \mathbf{B}(\mathbf{r}) = \boldsymbol{\nabla}(\boldsymbol{\nabla} \cdot \mathbf{B}(\mathbf{r})) - \boldsymbol{\nabla} \wedge (\boldsymbol{\nabla} \wedge \mathbf{B}(\mathbf{r})) \tag{2.19}$$

shows that the components of the field $\mathbf{B}(\mathbf{r})$ satisfy

$$\nabla^2 B_{\mathbf{e}_x} = 0, \quad \nabla^2 B_{\mathbf{e}_y} = 0, \quad \nabla^2 B_{\mathbf{e}_z} = 0,$$

giving a simplified form of (2.16)

$$\nabla^2 B^2 = 2\left\{|\boldsymbol{\nabla} B_{\mathbf{e}_x}|^2 + |\boldsymbol{\nabla} B_{\mathbf{e}_y}|^2 + |\boldsymbol{\nabla} B_{\mathbf{e}_z}|^2\right\} \geq 0, \tag{2.20}$$

which is a contradiction to the necessary condition for paramagnetic objects, outlined by the inequality given by (2.15). In free space, therefore, stability of paramagnetic objects at the equilibrium points is not possible.

With diamagnetic objects, on the other hand, $\chi < 0$, so the stability condition is given by

$$\nabla^2 B^2(\mathbf{r}) > 0, \tag{2.21}$$

showing that diamagnetic objects are possible to be stably levitated as they satisfy the condition (2.20). Additionally, for stability, the energy of the object at the equilibrium point must be a minima in each direction. Therefore, by taking the

second derivative in each direction of (2.6) we must satisfy

$$\frac{\partial^2}{\partial z^2}B^2 > 0, \qquad \text{(vertical stability)}, \tag{2.22}$$

$$\frac{\partial^2}{\partial x^2}B^2 > 0, \quad \frac{\partial^2}{\partial y^2}B^2 > 0 \qquad \text{(radial/horizontal stability)}. \tag{2.23}$$

The vertical and radial stability conditions are sufficient to conclude that the equilibrium point is stable, if they are satisfied. Both stability conditions can be reformulated in terms of the axial magnetic field strength, $B(0,0,z)$.

Firstly, we introduce a magnetic potential function, $\phi = \phi(\mathbf{r})$, such that

$$\mathbf{B}(\mathbf{r}) = \boldsymbol{\nabla}\phi(\mathbf{r}). \tag{2.24}$$

Substituting (2.24) into Maxwell's divergence free equation, shows that $\phi(\mathbf{r})$ satisfies Laplace's equation

$$\nabla^2\phi(\mathbf{r}) = 0, \tag{2.25}$$

giving,

$$\frac{\partial^2\phi}{\partial x^2} + \frac{\partial^2\phi}{\partial y^2} + \frac{\partial^2\phi}{\partial z^2} = 0. \tag{2.26}$$

As the magnetic field is rotationally symmetric about the vertical axis, it follows that the horizontal derivatives of the components of $\mathbf{B}(\mathbf{r})$ are equal along z, with

$$\frac{\partial}{\partial x}B_{\mathbf{e}_x}\bigg|_{\substack{x=0\\y=0}} = \frac{\partial}{\partial y}B_{\mathbf{e}_y}\bigg|_{\substack{x=0\\y=0}}, \tag{2.27}$$

giving,

$$\frac{\partial^2\phi}{\partial x^2}\bigg|_{\substack{x=0\\y=0}} = \frac{\partial^2\phi}{\partial y^2}\bigg|_{\substack{x=0\\y=0}}. \tag{2.28}$$

Therefore, using (2.24) we have Laplace's equation on the axis as

$$2\,\frac{\partial^2\phi}{\partial x^2}\bigg|_{\substack{x=0\\y=0}} + \frac{\partial^2\phi}{\partial z^2}\bigg|_{\substack{x=0\\y=0}} = 0, \tag{2.29}$$

where we may deduce that [6]

$$\left.\frac{\partial^2\phi}{\partial x^2}\right|_{\substack{x=0\\y=0}} = \left.\frac{\partial^2\phi}{\partial y^2}\right|_{\substack{x=0\\y=0}} = -\frac{1}{2}\left.\frac{\partial^2\phi}{\partial z^2}\right|_{\substack{x=0\\y=0}}. \tag{2.30}$$

Expanding the scalar potential about the axis, by Taylor expansion, $\phi(\mathbf{r})$ is expressed as

$$\phi(\mathbf{r}) = \phi(0,0,z) + x\left.\frac{\partial\phi}{\partial x}\right|_{\substack{x=0\\y=0}} + y\left.\frac{\partial\phi}{\partial y}\right|_{\substack{x=0\\y=0}} + \frac{1}{2}\left(x^2\left.\frac{\partial^2\phi}{\partial x^2}\right|_{\substack{x=0\\y=0}} + y^2\left.\frac{\partial^2\phi}{\partial y^2}\right|_{\substack{x=0\\y=0}}\right) + ... \tag{2.31}$$

However, on the axis, the horizontal components of the field are zero as the magnetic field is directed vertically, giving

$$\phi(\mathbf{r}) = \phi(0,0,z) + \frac{1}{2}\left(x^2\left.\frac{\partial^2\phi}{\partial x^2}\right|_{\substack{x=0\\y=0}} + y^2\left.\frac{\partial^2\phi}{\partial y^2}\right|_{\substack{x=0\\y=0}}\right) + ..., \tag{2.32}$$

which is the equation (14) in Berry and Geim [6]. This is reduced by using (2.30) to give

$$\phi(\mathbf{r}) = \phi(0,0,z) - \frac{1}{4}\left(x^2+y^2\right)\left.\frac{\partial^2\phi}{\partial z^2}\right|_{\substack{x=0\\y=0}} + ..., \tag{2.33}$$

From (2.24) we may express the horizontal components as

$$B_{\mathbf{e}_x}(\mathbf{r}) = x\left.\frac{\partial^2\phi}{\partial x^2}\right|_{\substack{x=0\\y=0}} + ..., \quad B_{\mathbf{e}_y}(\mathbf{r}) = y\left.\frac{\partial^2\phi}{\partial y^2}\right|_{\substack{x=0\\y=0}} + ..., \tag{2.34}$$

which may be expressed in terms of the vertical field terms by using (2.29) giving

$$B_{\mathbf{e}_x}(\mathbf{r}) = -\frac{x}{2}\left.\frac{\partial^2\phi}{\partial z^2}\right|_{\substack{x=0\\y=0}} + ..., \quad B_{\mathbf{e}_y}(\mathbf{r}) = -\frac{y}{2}\left.\frac{\partial^2\phi}{\partial z^2}\right|_{\substack{x=0\\y=0}} + ..., \tag{2.35}$$

The same process is carried out for the vertical component of (2.24) with

$$B_{\mathbf{e}_z}(\mathbf{r}) = \left.\frac{\partial\phi}{\partial z}\right|_{\substack{x=0\\y=0}} - \frac{1}{4}(x^2+y^2)\left.\frac{\partial^3\phi}{\partial z^3}\right|_{\substack{x=0\\y=0}} + ..., \tag{2.36}$$

The magnetic field close to the axis is then

$$B^2(\mathbf{r}) \approx \left(\left.\frac{\partial \phi}{\partial z}\right|_{\substack{x=0\\y=0}} \right)^2 + \frac{(x^2+y^2)}{4} \left[\left(\left.\frac{\partial^2 \phi}{\partial z^2}\right|_{\substack{x=0\\y=0}} \right)^2 - 2 \left.\frac{\partial \phi}{\partial z}\right|_{\substack{x=0\\y=0}} \left.\frac{\partial^3 \phi}{\partial z^3}\right|_{\substack{x=0\\y=0}} \right] + ..., \tag{2.37}$$

which can be expressed in terms of the vertical field on the axis, $B_{\mathbf{e}_z}(0,0,z) = B_{\mathbf{e}_z}(z)$ as

$$B^2(\mathbf{r}) \approx B^2_{\mathbf{e}_z}(z) + \frac{(x^2+y^2)}{4} \left\{ \left(\frac{\partial B_{\mathbf{e}_z}}{\partial z} \right)^2 - 2B_{\mathbf{e}_z}(z) \frac{\partial^2 B_{\mathbf{e}_z}}{\partial z^2} \right\}. \tag{2.38}$$

We are now in a position to find the stability criteria in the vertical and horizontal directions, at $x = y = 0$, which are to be expressed in terms of the axial field strength only. Returning to the stability conditions, given by (2.22) and (2.23), we find

$$\mathcal{D}_1(z) = \left.\frac{\partial}{\partial z} B_{\mathbf{e}_z}\right|_{\substack{x=0\\y=0}} + B_{\mathbf{e}_z}(z) \left.\frac{\partial^2}{\partial z^2} B_{\mathbf{e}_z}\right|_{\substack{x=0\\y=0}} > 0, \qquad \text{(vertical stability)} \tag{2.39}$$

$$\mathcal{D}_2(z) = \left.\frac{\partial}{\partial z} B_{\mathbf{e}_z}\right|_{\substack{x=0\\y=0}} - 2B_{\mathbf{e}_z}(z) \left.\frac{\partial^2}{\partial z^2} B_{\mathbf{e}_z}\right|_{\substack{x=0\\y=0}} > 0, \quad \text{(horizontal stability)} \tag{2.40}$$

as given by Berry *et al.* [6]. These stability conditions are notably independent of object properties; depending only on the component of magnetic induction in the axial direction and its derivatives. For diamagnetic levitation, the above conditions must both be satisfied simultaneously. Examining a water-air system as an example, the two vertical equilibrium positions, where the derivatives of the potential energy are zero along z, are seen to have different stability characteristics, as shown in figure 2.6. Both equilibrium positions are stable in the radial/horizontal direction, satisfying the condition for horizontal stability. For the equilibrium position at $z = 11.3$ cm, both (2.39) and (2.40) are satisfied showing that diamagnetic levitation is possible. Whereas, at $z = 6.3$ cm, (2.39) is not satisfied showing that free levitation is not possible at this point; here, the equilibrium is unstable to displacements in the vertical direction.

In the present work, we are primarily interested in the radial stability condition, as vertical stability is enforced by confining the fluids in a narrow gap between two horizontally aligned flat plates. In the experimental set up, to be discussed in chapter 3, the magnetic field does not allow for free levitation within the magnet bore with the fluid-fluid system used, but the system has other desirable properties which will be explored later.

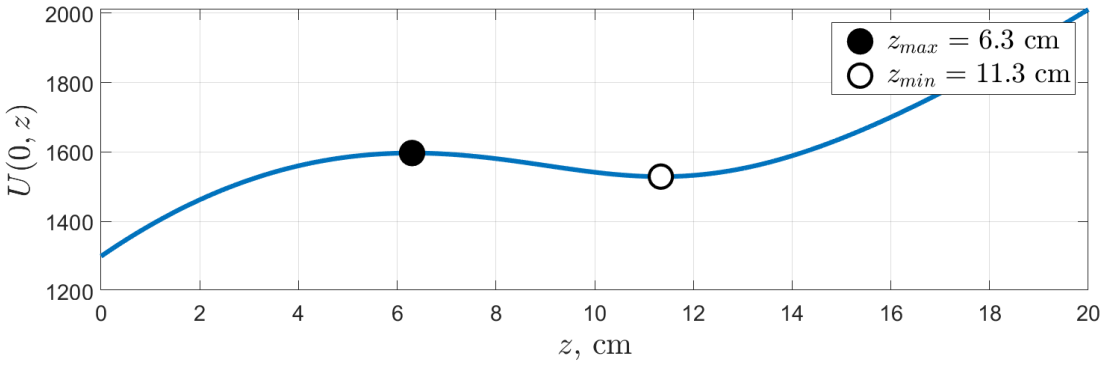

(a) Potential energy along the vertical direction

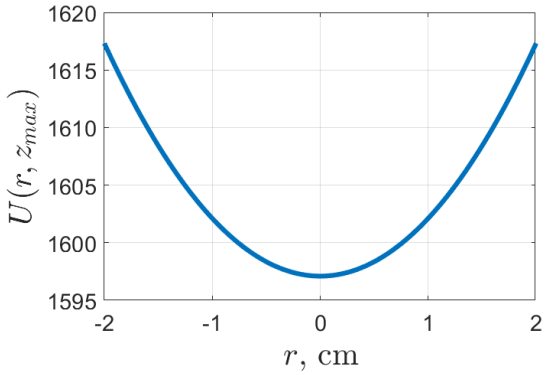

(b) Potential energy at $z = z_{min}$

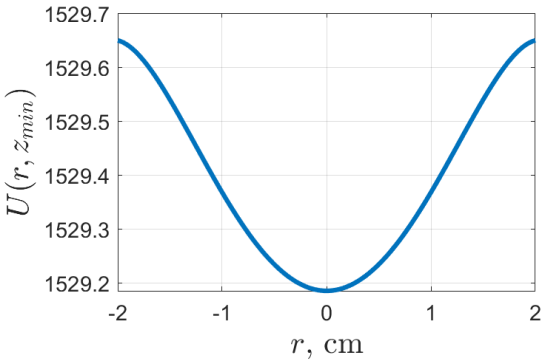

(c) Potential energy at $z = z_{max}$

Figure 2.6: Potential energy for a water droplet surrounded by air in a magnetic field of strength $B(0,0,0) = 18.5$ T, where $r = \sqrt{x^2 + y^2}$. (a) Potential energy along the centre axis with the minima and maxima points, as shown in figure 2.5 and indicated by the unfilled and filled dots, respectively. (b) and (c) Potential energy across the diameter of the magnet bore at the minima and maxima respectively.

For simplicity, the preceding section discussed the equilibrium levitation points and stability criteria of a volume of water suspended in a vacuum. In most experiments however, the object is surrounded by air at atmospheric pressure and temperature, not vacuum. Nevertheless, air has a magnetic susceptibility of $|\chi_{air}| \sim 10^{-7}$, which is small in comparison to that of water, and has a density of

order 10^{-3} times that of water. Hence, the effects of buoyancy and magnetic force from the surrounding air on the levitation of water in air are relatively small. For other fluid-fluid systems where magnetic susceptibilities are of similar order, the equilibrium criteria derived must be modified to account for the magnetic forces on the surrounding fluid. We must also take into account the effect of buoyancy from the surrounding fluid. An analogous principle that we may adapt for use in a magnetic field is the Archimedes principle and is discussed in the next section. Examination and application of this principle with respect to a static magnetic field will provide us with the tools necessary to create radial stability of typically unstable fluid-fluid systems.

2.3 The Magneto-Archimedes principle

Our attention is now drawn to volumes of fluid submersed within a second immiscible fluid. The magneto-Archimedes principle is similar to the Archimedes principle in that it relates to the buoyancy of objects in a magnetised fluid. By the Archimedes principle, submersed objects become *apparently* lighter in water than in air due to the buoyancy force that results from the pressure gradient in the vertical direction. The buoyant force is equal to the weight of fluid displaced by the object. Under the influence of a spatially-varying magnetic field, the magnetic force acting on the surrounding fluid modifies the pressure gradient, and so alters the buoyancy force acting on the object. With the addition of the magnetically-modified buoyancy force, the net force acting on an object surrounded by a diamagnetic or paramagnetic fluid is given by [24]

$$\delta\mathbf{F} = -\rho_f g\delta V\mathbf{e}_z + \frac{\chi_f}{2\mu_0}\delta V\boldsymbol{\nabla}B^2(r,z) + \rho_s g\delta V\mathbf{e}_z - \frac{\chi_s}{2\mu_0}\delta V\boldsymbol{\nabla}B^2(r,z), \qquad (2.41)$$

where we now use cylindrical polar coordinates r, θ, z. Here, we denote the density and volume magnetic susceptibility of the surrounding fluid by ρ_s and χ_s respectively; ρ_f and χ_f are the density and volume magnetic susceptibility of an

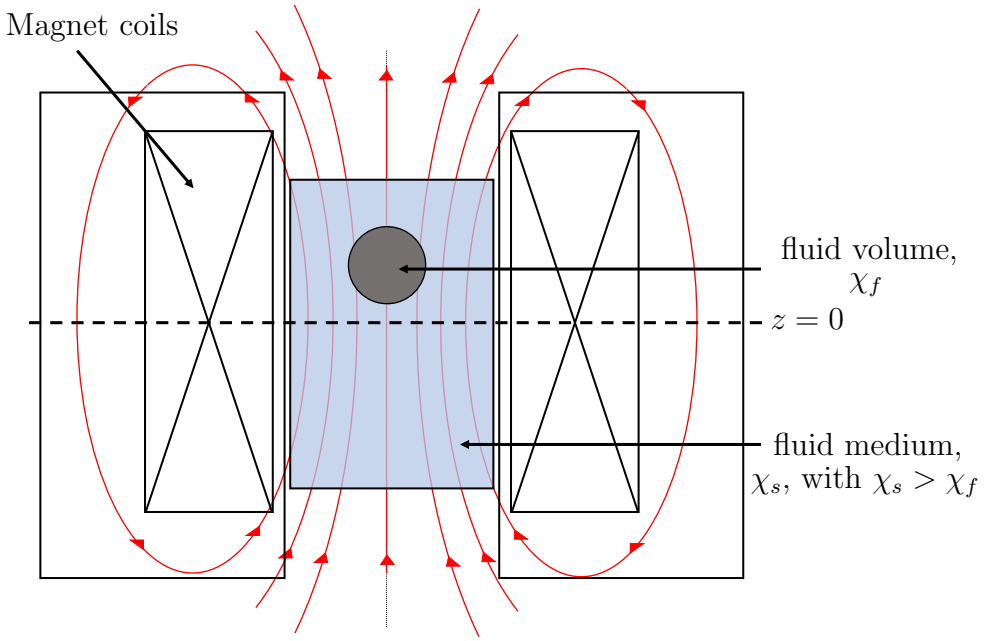

Figure 2.7: Schematic illustrating the magneto-Archimedes effect in a magnetic field generated by a superconducting solenoid magnet. Here, a 'blob' of diamagnetic fluid (grey) is shown submerged in a paramagnetic fluid (blue). The two fluids are assumed to be immiscible. The diamagnetic fluid is repelled upwards, away from the region of strong magnetic field at the centre of the coil. It is also repelled radially, away from the regions of relatively high magnetic field close to the coils, towards the solenoid axis. At the same time the paramagnetic fluid is drawn *toward* these same regions of high magnetic field enhancing the vertical upward force on the diamagnetic blob, and also the radial magnetic force that pushes the blob toward the axis.

object submerged in the fluid. In the present work, we need to consider the force acting on a magnetised fluid, or a small volume element of fluid, surrounded by a second magnetised fluid. Hence it is useful to read (2.41) as the net force on a small element of fluid, of volume δV.

Figure 2.7 shows, schematically, a magneto-Archimedes experiment in which a diamagnetic object (in this case, a 'blob' of diamagnetic fluid) is suspended within a paramagnetic fluid. In a typical levitation experiment that makes use of the magneto-Archimedes effect, the buoyancy force is enhanced by the magnetisation of the surrounding fluid. An example is the 'levitation' of metals such as gold and lead in magnetised liquid oxygen, see Catherall *et al.* [12]. In addition to

the vertical magnetic force in these experiments there is also, in general, a radial magnetic force. If the diamagnetic object/fluid blob is located within the bore, this radial force repels the object away from the relatively high field regions close to the coils, toward the axis of the solenoid. At the same time, the surrounding paramagnetic fluid is attracted toward these same regions, enhancing the net radial force pushing the object toward the axis. As discussed in section 2.2.1, we consider the forces at $r = 0$ to find the equilibrium points on the axis, adapting to (2.11) to consider two fluids, giving

$$B(0,z)\,\frac{\partial}{\partial z}B(r,z)\bigg|_{r=0} = \frac{\rho_f - \rho_s}{\chi_f - \chi_s} g\mu_0. \tag{2.42}$$

This equation involves the magnetic force on both the fluid element and its surroundings. If we define the apparent density as $\rho_a = \rho_f - \rho_s$ and apparent magnetic susceptibility of the system as $\chi_a = \chi_f - \chi_s$, we can see that the condition (2.42) is identical to (2.11) where

$$B(0,z)\,\frac{\partial}{\partial z}B(r,z)\bigg|_{r=0} = \frac{\rho_a}{\chi_a} g\mu_0. \tag{2.43}$$

The discussion of the equilibrium point then follows as in section 2.2.1. The magneto-Archimedes principle is highly relevant to the experiments described later. However, whereas a typical levitation experiment focuses on the vertical component of the net force given by equation (2.41), in this work we exploit the *radial* component of this force, where the radial body forces acting on the fluid can be considered, in some sense, as an effective radial gravitational force. In chapter 3 we shall discuss the experimental set-up and describe the fluids used in our experiments, in which we exploit the magneto-Archimedes principle to produce a stable initial configuration of two immiscible fluids.

Much has been discussed on the properties of diamagnetism and paramagnetism. For many materials with small magnetic susceptibility, a large magnetic

field strength is required to balance, or even dominate, the force of gravity. In this work, a superconducting solenoid magnet is used to create the large field strengths necessary for stability.

2.4 The superconducting cryogenic magnet

Superconducting magnets have become increasingly popular amongst research for use in applications where conventional electromagnets are no longer feasible due to the constant, large electric current needed to maintain high field strengths. One famous example of the use of superconducting magnets is Magnetic Resonance Imaging (MRI). This particular application uses strong, uniform magnetic fields to obtain a picture of a patient's body [36]. Here, a brief overview of the superconducting magnet used in our experiments is provided, and a brief discussion of the properties of a superconductor is given.

Available to us is a superconducting solenoid magnet which produces a magnetic field of up to 18.5 T at the centre of the solenoid $B(0,0)$, manufactured by Cryogenic Ltd. The field is generated by three superconducting coils wound around an open, room temperature bore of diameter 5.85 cm. The inner and middle coils are made from Niobium-Tin (Nb_3Sn) type II superconductor with the outer coil made from Niobium-Titanium (NbTi) type II superconductor [32]. The three coils are connected in series so that each coil carries the same electric current. Due to the geometry of the magnetic coils, the magnetic field lines take the shape as shown in figure 2.3. This superconducting magnet is cryogen free meaning that the low temperatures required for operation do not require liquid helium in direct contact with the coils. There are two methods used to thermally insulate the superconducting coils. First, the chamber which houses the superconducting coils is vacuum pumped. This reduces the conduction of heat from outside the chamber. Secondly a high-purity aluminium radiation shield reduces the heating through radiation.

A superconductor is a material which can conduct electricity without electrical resistance. With ordinary conductors, in general, the electrical resistivity falls gradually as its temperature decreases. Whereas, for superconducting materials, there is a critical temperature T_c below which the resistivity abruptly becomes zero; an electric current will circulate within a superconducting material indefinitely, provided the material is kept in its superconducting state. The change in the resistance with temperature for a superconducting and non-superconducting material is shown in figure 2.8 to illustrate the abrupt change in resistivity at T_c.

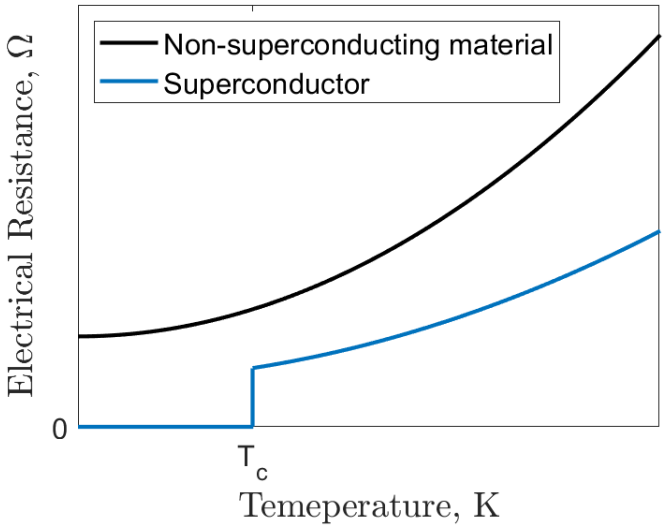

Figure 2.8: Simplified temperature (Kelvin, K) vs resistance (Ohm, Ω) graph for two sample materials with a zero applied magnetic field.

When an external magnetic field is applied to a superconductor the magnetic field is expelled from the superconductor when cooled to $T < T_c$, i.e. during the transition to its superconducting state. For type I superconductors, the magnetic field is excluded completely; exhibiting the complete Meissner effect [17]. However, when the applied magnetic field is greater than a critical field value H_C, the material becomes non-superconducting, returning to its normal state. This process is reversible if the magnetic field is lowered to be less than H_C. In comparison, Type II superconductors enter a "mixed state" when the magnetic field is greater than a critical field strength H_{C_1}. The "mixed state" exhibits an

incomplete Meissner effect and is characterised by the development of magnetic vorticies which allow partial admission of magnetic field lines through the superconductor. At a higher critical field strength H_{C_2}, the superconductor returns to its normal state as with type I superconductors. The value of H_{C_2} is typically higher than for the critical field strength H_C for type I superconductors, making them suitable for use in high field magnets [35].

Our experiments are primarily concerned with radial forces acting on an interface between two fluids. The fluids will also be subjected to a gravitational force. If a the heavier fluid lies above the lighter fluid, there will be a gravitational instability. Previous work completed by Scase *et al.* [45] have performed experiments which utilise an "effective gravity" in the vertical direction. This was done by effectively reversing gravitational force upon a density stratified regime using a superconducting magnet. Here, we proceed with the same idea in the radial direction. We are able to negate vertical gravitational forces by restricting the vertical domain and by utilising the equilibrium points found in section 2.2.2.

Chapter 3

Experimental procedure

The present experimental investigation makes use of a superconducting magnet provided by the School of Physics and Astronomy at the University of Nottingham. The magnet presented particular challenges in designing and building the apparatus, as well as conducting the experiments. The primary difficulties are those presented by working in a strong, static magnetic field, and within the confined space of the magnet bore.

In this chapter, we outline the experimental procedure developed to perform the interfacial instability experiments. The chapter will detail the equipment used to perform and record the experiments, and the 'Hele-Shaw' type cell used to hold the fluid-fluid system. We will also describe the fluids chosen to perform the experiments, and their properties.

3.1 Experimental set-up

The experimental set-up involves two principle phases. The first is preparing the chosen fluids, and the second is the preparation and filling of the cell. Following this, the volume magnetic susceptibilities of each fluid are then measured experimentally as described later.

3.1.1 Description and preparation of fluids

Careful choice of fluids is imperative. The two fluids were selected according to the following requirements:

1. We require a system of two immiscible fluids with differing density.

2. The lower density fluid should be attracted to the higher magnetic field region at the edges of the cell when the cell is placed in the bore of the superconducting magnet; i.e. we require the liquid to be relatively *paramagnetic*.

3. The higher density fluid should be repelled from the higher field region toward the centre of the cell; i.e. we require the liquid to be relatively *diamagnetic*.

4. We require the interfacial tension to be as low as possible. This is to limit the critical angular velocity required to induce instability in the interface to one that is experimentally achievable using the apparatus installed in the magnet bore. Interfacial tension is known to suppress radial instability, as will be seen theoretically in chapter 5.

These four requirements are tight restrictions on the possible combinations of fluids. After reviewing the small number of possible combinations, we selected the propylene carbonate (PC) as the higher density fluid and a solution of pure water with paramagnetic salt manganese chloride ($MnCl_2$) as the lower density fluid, abbreviated by MC. This combination of fluids has the required properties at room temperature and pressure, is relatively inexpensive, straightforward to prepare, chemically stable and is not hazardous to health, with trivial precautions. In addition it has one of the smallest interfacial tensions we were able to find in the literature.

The densities of both fluids were measured by weighing a glass vessel with volume 49.65 ml and mass 31.86 gms. As a check on our experimental method,

the density of water was measured to be 999.32 ± 0.05 kg m^{-3} at 22.0°C and compared to a literature value, giving an error of 0.15% relative to the empirical calculation given by Novotny *et al.* [40]. By the same method, the density of PC was measured to be 1200.47 ± 0.51 kg m^{-3} at 22.0°C. In Moumouzias *et al.* [38], the density of PC was measured at 1203.4 kg m^{-3} and 1197.8 kg m^{-3} at 20.0°C and 25.0°C, respectively, showing that our measured value is consistent within the range of temperatures quoted. The density of MC depends upon the concentration of $MnCl_2$. In our experimental study the concentration remained consistent at 0.100 ± 0.005 mol L^{-1} with a density measurement of 1009.70 ± 0.08 kg m^{-3} at 22.0°C. Novotny *et al.* [40] derived a formula to determine the density of binary aqueous solutions such as MC, which gives a density value of 1008.30 ± 0.52 kg m^{-3}. Comparison with our experimental value gives a maximum relative percentage error of no greater than 1%. Blue dye was added to the MC solution to provide contrast between the two fluid phases during analysis. This increased the density to 1010.22 ± 0.03 kg m^{-3} at 22.0°C.

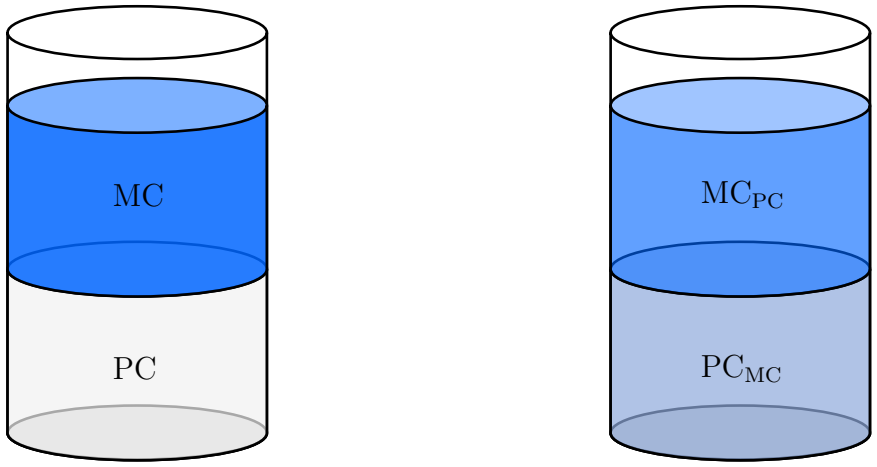

(a) Before diffusion (b) After diffusion

Figure 3.1: Fluids before and after diffusion in a preparatory beaker. (a) Before diffusion takes place, MC 'sits' above PC due to the density difference. (b) As PC is partially soluble in water, some gets dissolved in MC until the reaction reaches an equilibrium. The MC_{PC} consists primarily of MC with dissolved PC. While MC_{PC} consists primarily of PC with dissolved MC. The blue tint is a result from the addition of blue dye.

Fluid	Density, ρ kg m^{-3}	Uncertainty, kg m^{-3}
PC	1200.50	0.50
MC	1009.73	0.08
MC + blue dye	1010.22	0.03
PC_{MC}	1181.00	3.10
MC_{PC}	1048.30	0.50

Table 3.1: Summary of density for PC and MC. The last two rows are the result of mixing equal volumes of PC and MC together.

As propylene carbonate is soluble with water up to 25 wt% [50], the PC-MC combination was allowed to reach chemical equilibrium before use. We followed Smirnov *et al.* [50] by using saturated solutions of PC in MC and MC in PC, which are created by mixing equal volumes of PC and MC together, as seen in figure 3.1. The resultant solution was allowed to sit and reach equilibrium. The density of both PC and MC altered as a result of this mixing, and the measured values of each, at equilibrium, are summarised in table 3.1. The solution of PC with dissolved MC and blue dye is denoted by PC_{MC}, while the solution of MC mixed with blue dye and PC is denoted by MC_{PC}.

To obtain an experimental measurement of the interfacial tension between PC_{MC} and MC_{PC}, the "pendant drop method" was used [21]. A small, flat headed, needle with 0.57 ± 0.06 mm outer diameter, was used to form PC_{MC} drops, which hang from the needle under gravity, surrounded by the MC_{PC} solution. A series of images of pendant drops were recorded and processed to calculate an interfacial surface tension of 2.8 ± 0.3 mN m^{-1}. Smirnov *et al.* [50] measured the interfacial tension between water (H_2O) and PC to be approximately 2.95 mN m^{-1}. As MC_{PC} is an aqueous solution, we expect a similarity between Smirnov's interfacial tension value for a H_2O-PC interface and a MC_{PC}-PC_{MC} interface. Since the difference in our measurements is $\simeq 10\%$, a significant difference, care must be taken when using this value in predictive models.

3.1.2 Description and preparation of the cell

As described in chapter 1, a Hele-Shaw cell is characterised by the slow viscous flow between two flat plates, separated by a small gap relative to a length scale, giving a small aspect ratio. The experiments investigating radial stability and described by Carillo *et al.* [11], Alvarez-Lacelle *et al.* [1] and Bongrand *et al.* [8] were all performed using a circular Hele-Shaw cell. In this section the circular Hele-Shaw cell used for experiments, as well as the materials for its manufacture, are described.

During the process of experimentation various materials and designs were tested to create a cell that is capable of performing the required experiments. Figure 3.2 shows the final cell design. The configuration consists of two separate halves, which form the frame and are bound together with six equispaced screws. Each half is made from polytetrafluoroethylene (PTFE) which has a high chemical, thermal and electrical resistance [51]. There is also a 'lip' which accepts glass discs with a depth of 3 mm and radius 19.10 ± 0.03 mm, as shown in figure 3.3a. The glass is made from synthetic sapphire to produce a transparent material more durable than glass for scratch resistance, as well as being chemically resistant to most acids [16]. Placing the glass discs in the cell frame leaves a gap of thickness $b = 1.80 \pm 0.06$ mm between them and a volume of 2.10 mL for fluids to occupy, with a reported error in volume of 3.3%. There are two ports located along the diameter of the upper half, as seen from the 'side view' in figure 3.2, which allows the injection of fluids, represented by the red directional arrows shown in the 'cross section' of figure 3.2. The presence of the ports allow us to fill the cell while expelling trapped air bubbles.

The preparation of the cell started with cleaning the apparatus. This involved the thorough cleaning of the sapphire glass discs through a multistage process. The discs were first cleaned with a soapy solution followed by a rinse with purified, deionised water. Then, the glass discs were submerged in an ultrasonic bath of

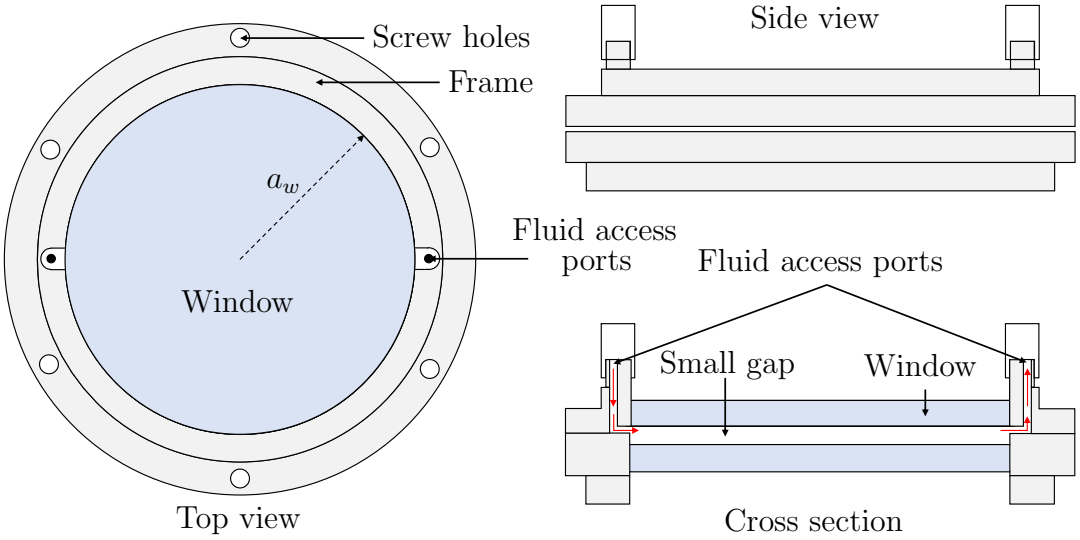

Figure 3.2: Schematic showing the multiple views of the finalised cell design used for the experiment. The red arrows in the cross section indicate the fluid flow when filling the cell. The radius of the window, where the experiments can be observed, is $a_w = 18.10 \pm 0.03$ mm. The radius of the gap between the glass discs is 19.10 ± 0.03 mm and the diameter of the fluid access ports is 0.50 ± 0.06 mm.

acetone followed by a secondary bath with isopropyl alcohol. Finally, the discs were rinsed with purified water again and dried using nitrogen gas. This process removed surface roughness caused by impurities such as dust and oily substances. A similar cleaning process was performed for the PTFE cell frame.

Once the cell was thoroughly cleansed, the glass discs were fixed into place, as shown in figure 3.2. A silicone rubber compound was used as a sealant around the edges to ensure a water tight, pressure resistant seal to prevent leaking, as shown in figure 3.3a. The cell was then assembled with six equispaced screws, and a layer of PTFE tape was tightly wound around the side of the cell to prevent possible leaking between the join.

Once assembled, the cell was pre-wetted with the MC_{PC} solution to reduce adhesion to the glass discs and emptied [11]. To remove air bubbles, the cell was placed vertically and MC_{PC} was injected from the bottom to allow air to escape through the upper port. The injection of fluid was performed slowly to prevent air entrainment inside the cell. Figure 3.3b shows a schematic of the filling

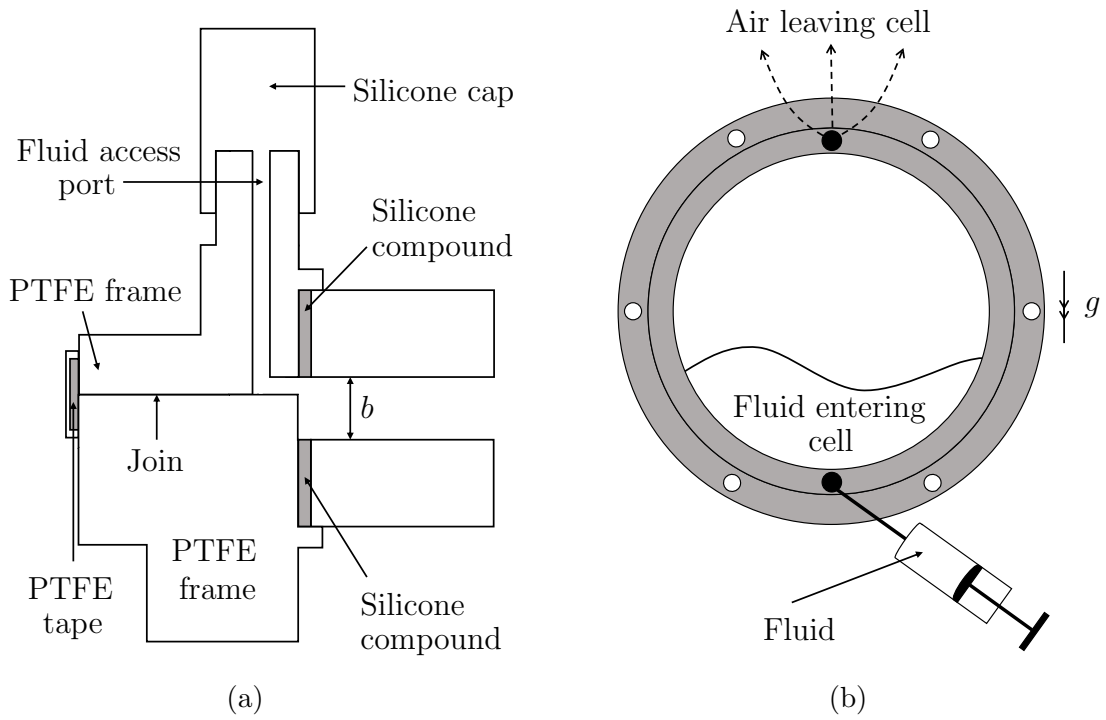

Figure 3.3: (a) Cross-sectional diagram showing half of the Hele-Shaw cell with gap thickness b, highlighting placement of preventative measures against leaking. (b) Illustrative figure to show method of filling the cell with fluid.

method. The remaining space between the plates was then filled with PC_{MC} using the same method, with the absence of air bubbles. To ensure equality in fluid volumes, PC_{MC} was injected up to a marker indicating when the fluids would be equal in volume. This method results in fluid layers that are equal in volume, and there being no observable air bubbles.

3.2 Cell positioning and volume magnetic susceptibility

Typically, volume magnetic susceptibilities are experimentally determined by using a Gouy balance as is the case in Baldwin *et al.* [2], where they measured a magnetic susceptibility for MC with a concentration of 0.06 mol L^{-1}. Here we used a different approach, utilising the vertical magnetic forces on the two fluids in the magnet bore.

With the cell assembled and filled with the two fluids, the cell was fixed inside a hollow plastic cylinder resting above a translucent disc to disperse light passing through from below. The cylinder was placed inside the magnet bore with the solenoid set to produce a field of strength $B(0,0) = 9.2$ T, with a light source placed at the bottom, as seen in figure 3.4. The translucent disc dispersed the light across the cell to provide uniform lighting conditions. Observing the shape of the interface allowed us to position the cell in the magnet bore *close to* one vertical equilibrium point, defined here as $z = z_0$ and discussed in section 2.2.2. This is when the vertical component of equation (2.41) is balanced such that

$$0 = (\rho_2 - \rho_1)g - \frac{(\chi_2 - \chi_1)}{2\mu_0} \frac{\partial}{\partial z} B^2 \bigg|_{\substack{r=0 \\ z=z_0}}, \tag{3.1}$$

where the subscripts $1, 2$ denote the inner and outer fluid layers respectively, as shown in figure 3.5. A rearrangement of (3.1) gives a relation for the difference in volume magnetic susceptibilities as

$$(\chi_2 - \chi_1) = 2\mu_0(\rho_2 - \rho_1) \left(\frac{\partial}{\partial z} B^2 \bigg|_{\substack{r=0 \\ z=z_0}} \right)^{-1}. \tag{3.2}$$

We were guided by the shape of the interface between the two fluid layers in order to adjust the position of the cell towards the equilibrium point. The interface made two circular contact lines with the top and bottom glass plates of the cell, as in figure 3.5. At the vertical equilibrium point, we expect these two circular contact lines to have the same diameter. Therefore we adjusted the vertical position of the cell until both contact lines, as viewed from a camera mounted above, align. The effect of perspective foreshortening was negligible since the distance between the cell and the camera was much larger than the gap thickness. Through this method, the position of the vertical equilibrium point was found to be $z_0 = 31.0 \pm 0.5$ mm above the $z = 0$ mm plane as shown in figures 2.3 and 3.4.

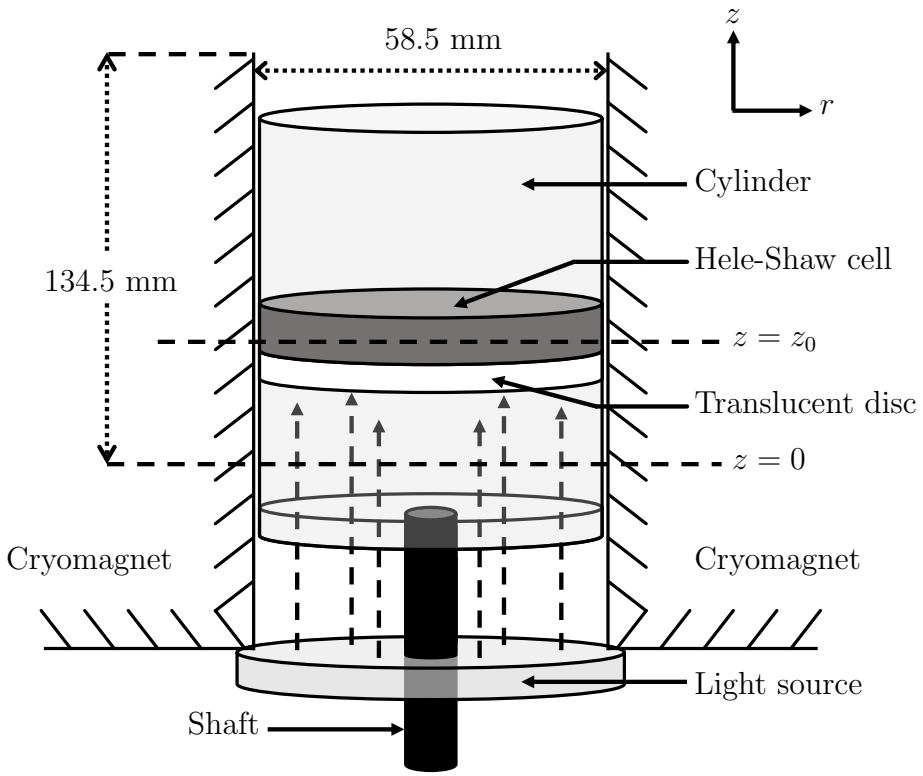

Figure 3.4: Diagram to show placement of the cell inside the magnet bore. The dashed arrows indicate light rays from the light source beneath the magnet bore.

In section 2.2.2, we described the two vertical equilibrium points for the case of water levitated in air. The same can be done for the PC_{MC}-MC_{PC} system. Figure 3.6 shows the potential energy along the vertical centre line of the magnet bore at $r = 0$ mm, with the solenoid producing a field of strength $B(0, 0) = 9.2$ T. Similar to figure 2.6, there are two vertical equilibrium points, one stable and one unstable. However, in contrast to figure 2.6, the radial stability differs between each vertical equilibria. When $z = z_0 = z_{max}$, radial forces act to centralise the inner fluid towards the centre axis of the magnet bore when disturbed. Whereas, at the upper equilibrium point, $z = z_{min}$, the radial forces will pull the inner fluid towards the magnet walls and repel the outer fluid towards the centre; the reason for this different behaviour is that the point $z = z_{min}$ lies outside the coils of the solenoid magnet. The initial condition in our experiments requires the more dense fluid to occupy the inner region of the cell which is achieved at $z = z_{max}$.

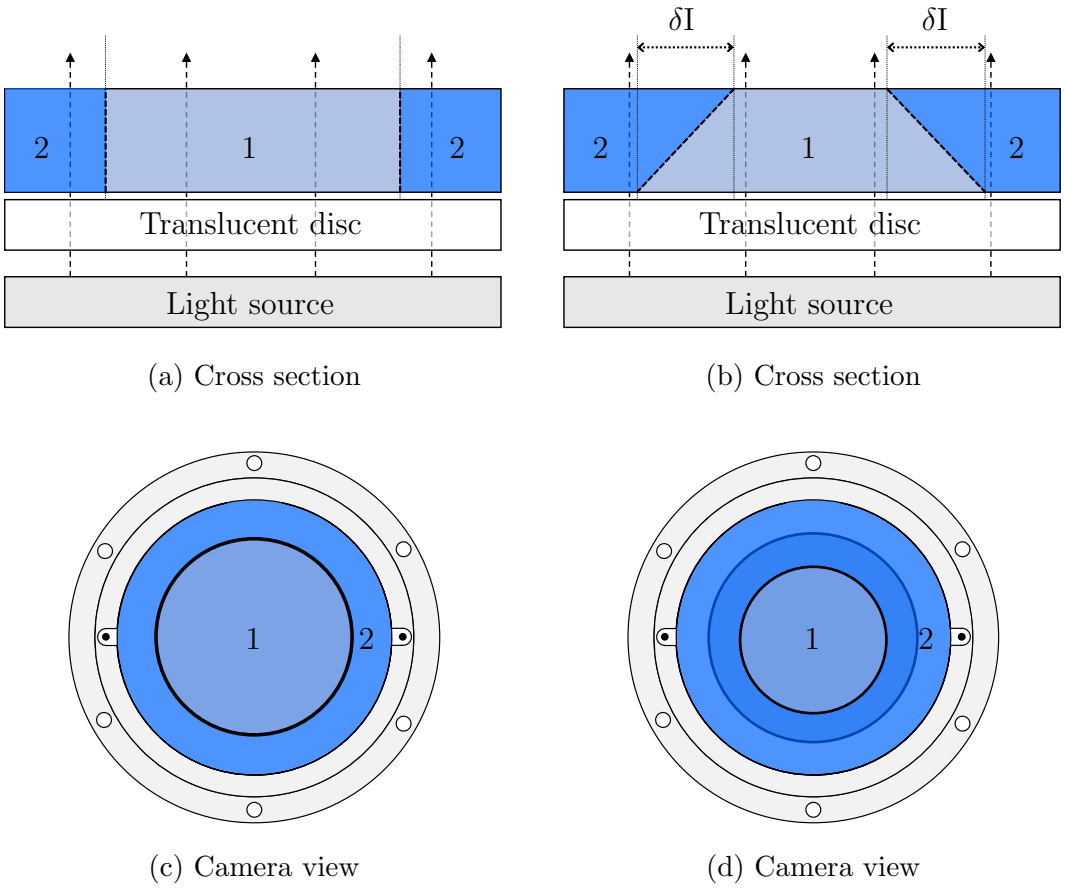

(a) Cross section (b) Cross section

(c) Camera view (d) Camera view

Figure 3.5: Light source highlighting the contact between the fluid and the glass plates at a vertical equilibrium point ((a),(c)) and non-equilibrium point ((b),(d)). The inner fluid region is denoted by 1 and the outer fluid region is denoted by 2. (a), (c) show the balance of vertical forces with radial forces acting. The contact lines in (c) appear to have the same diameter. (b), (d) show the effect of unbalanced vertical force on both fluid phases, and δI shows the difference in diameter of the upper and lower contact lines. In this case, the outer fluid 2 feels a buoyant force. The effect is non-equal diameter of the contact line on the top and bottom plate when observed through the perspective of the camera, shown in (d).

Evaluating the partial derivative of the field strength in (3.1) at $z_0 = 31.0 \pm 0.5$ mm, and inserting the experimental density measurements of the two fluids, we find the difference in magnetic susceptibility to be

$$(\chi_1 - \chi_2) \approx -1.45 \times 10^{-5}. \tag{3.3}$$

Though we only need the difference in volume magnetic susceptibilities throughout this work, we may produce an empirical measurement for the absolute sus-

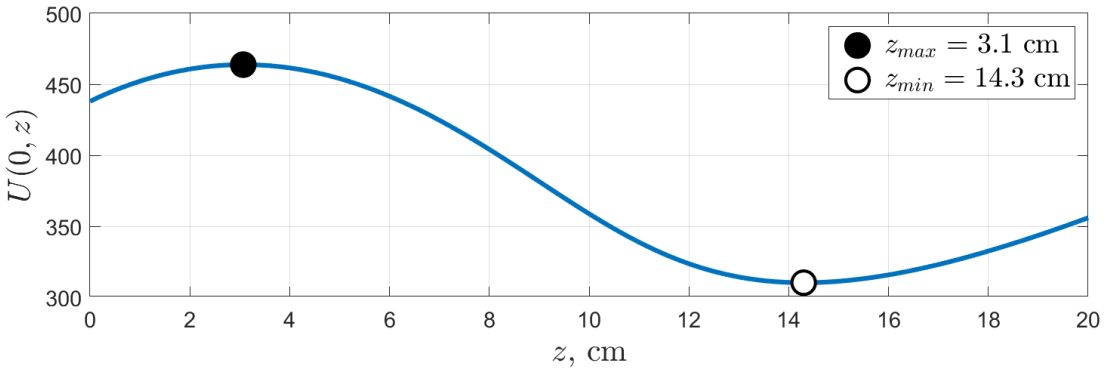

(a) Potential energy along the vertical direction

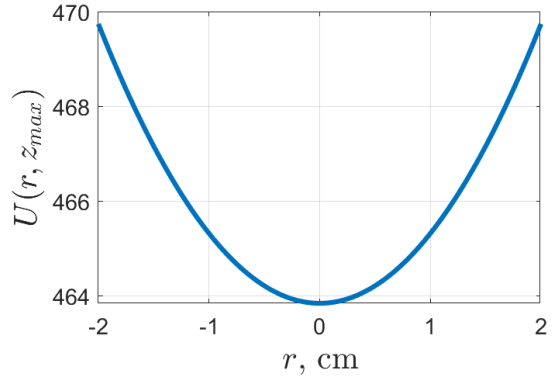

(b) Potential energy at $z = z_{max}$

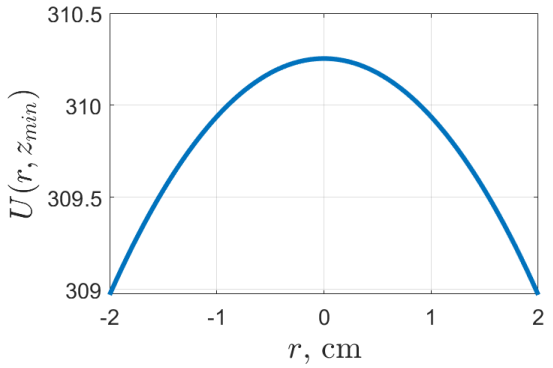

(c) Potential energy at $z = z_{min}$

Figure 3.6: Potential energy for a PC_{MC}-MC_{PC} system in a magnetic field of strength $B(0,0) = 9.2$ T. (a) Potential energy along the centre axis with the minima and maxima points. (b) and (c) Potential energy across the diameter of the magnet bore at the minima and maxima respectively.

ceptibility of PC_{MC}, and, consequently, for PC in place of a literature value. We may determine the volume magnetic susceptibility of MC by using Curie's law [27], and given as

$$\chi = \frac{C}{T}, \tag{3.4}$$

where T is temperature in Kelvin and C is known as the Curie constant; a property dependent on the material, see [27]. For a temperature of 22°C, the volume magnetic susceptibility of MC with 0.1 mol L^{-1} is $\chi_{MC} \approx 9.6 \times 10^{-6}$. Substituting for χ_2 in equation (3.3), we obtain an estimate for $\chi_1 = \chi_{PC_{MC}} \approx -4.9 \times 10^{-6}$ with an uncertainty of 3.5%. The concentration of MC in PC is assumed small so we conclude that, by our estimation, PC is a diamagnetic compound while MC is paramagnetic. This method of empirically determining the volume magnetic susceptibility of PC is derived on the assumption of small

concentration of MC in PC. Therefore, we only use the value of the difference in magnetic susceptibilities, (3.3).

3.3 Critical angular velocity

In order to fully carry out our analysis, we first describe the critical angular velocity, determined theoretically. The critical angular velocity is defined to be the angular velocity at which the radial forces at the interface, $r = r_0$, are balanced. Returning to the magneto-Archimedes (2.41) in section 2.3, with the subscript notation $j = 1, 2$ for the inner and outer fluids respectively, and applying centrifugal forces acting on each fluid layer, we obtain the 'buoyancy force' in the radial direction as

$$\mathrm{F}_r = \frac{(\chi_1 - \chi_2)}{2\mu_0} \frac{\partial}{\partial r} B^2 \bigg|_{\substack{r=r_0 \\ z=z_0}} + (\rho_1 - \rho_2) r_0 \Omega^2, \tag{3.5}$$

where the force acts on the inner fluid region (subscript 1) from the outer fluid region (subscript 2). The second term on the right hand side of (3.5) is analogous to the vertical buoyancy force by gravity, but is now due to the presence of angular velocity. When both fluid layers are equal in density, neither will exert pressure from this term, but both will continue to experience a radial centrifugal force.

The discussion in section 3.2 concluded that the interface is stable in the absence of rotation, at $z = 31.0$ mm, as the inner fluid is repelled from the higher field region at the edges of the cell, whilst the outer fluid is magnetically attracted towards it. Rotation about the vertical axis through the centre of the cell alters the radial force on both fluids. The centrifugal force exerts a radial force on both fluids, in the direction pointing toward the edge of the cell, for increasing r. For small angular velocities, Ω, the centrifugal force remains small compared with the magnetic forces on the system, maintaining a net radial force directed towards the axis of rotation. However, for larger velocities this is no longer the case; a

transition occurs at some critical angular velocity Ω_c

The critical angular velocity can be found directly from equation (3.5) by setting the net radial force to zero, at the interface. Rearranging for the critical angular velocity gives

$$\Omega_c^2 = \frac{(\chi_1 - \chi_2)}{2\mu_0 r_0(\rho_2 - \rho_1)} \frac{\partial}{\partial r} B^2 \Big|_{\substack{r=r_0 \\ z=z_0}}. \tag{3.6}$$

Figure 3.7 shows the effect on the radial energy potential at the interface against the influence of centrifugal forces. Below the critical angular velocity, the force acting on the inner fluid (PC) is restoring, directed towards $r = 0$, with the interface stable under perturbations. Above the critical angular velocity, the net radial force on an element of the dense inner fluid (PC) is directed outward, whereas the net radial force on an element of the lighter outer fluid (MC) is directed inward. Hence, for angular velocities above the critical angular velocity, the interface is unstable to perturbations, as in the classical Rayleigh-Taylor instability.

We obtain the interface location in figure 3.7 at $r_0 = 13.1$ mm, which is calculated from the image processing techniques discussed in the next chapter, and the radial gradient of the magnetic field at (r_0, z_0) is

$$\frac{\partial}{\partial r} B^2(r, z) \Big|_{\substack{r=0 \\ z=z_0}} \approx 74.7 \text{ T}^2\text{m}^{-1}.$$

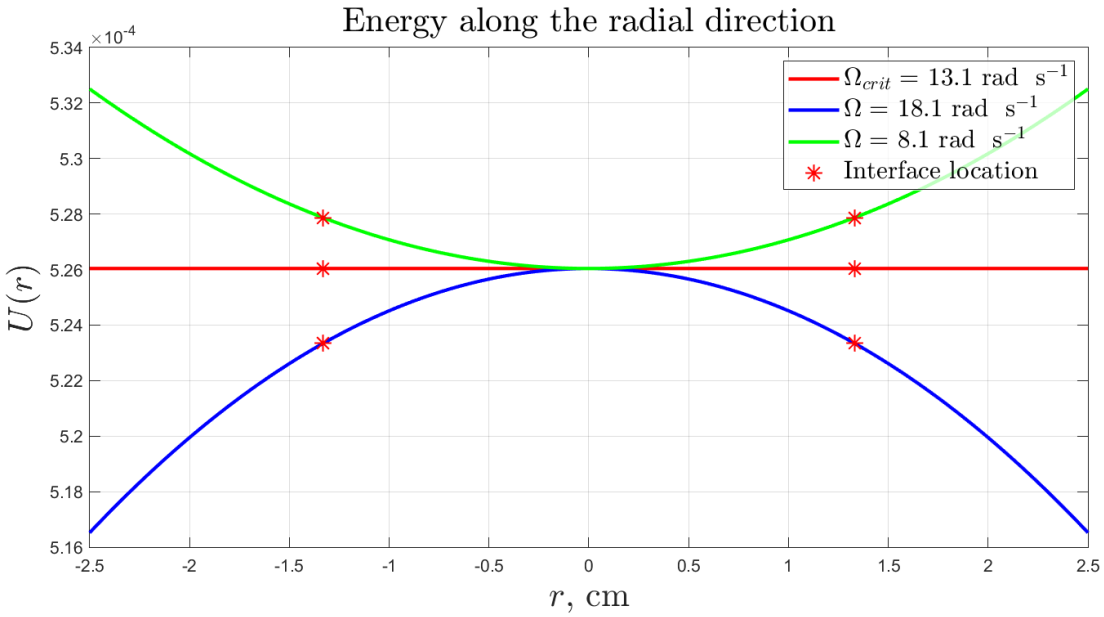

Figure 3.7: Potential energy of a unit volume element of inner fluid at the interface, measured along the radial direction in the magnet bore, at $z = 31.0$ mm. The initial position of the interface is indicated by the star symbols. For $\Omega < \Omega_c$, the net radial force on an element of the inner fluid at the interface is directed toward the rotation axis and the net radial force on an element of the outer fluid at the interface is directed away from the rotation axis. For $\Omega > \Omega_c$, the converse is true and the interface is thus unstable.

As can be seen by equation (3.6), real values of Ω_c are only permissible for a positive right hand side. In our current set up the density difference, $(\rho_1 - \rho_2) \approx -132.7$ kg m^{-3}, and the radial gradient of the magnetic field are both positive while $(\chi_1 - \chi_2) \approx -10^{-5}$ is negative. This follows from the property that the inner fluid layer, $\mathrm{PC_{MC}}$, is more dense and diamagnetic with respect to the outer fluid layer, $\mathrm{MC_{PC}}$, and the magnetic field gradient is positive for increasing r. Substituting all the necessary values into (3.6), the critical angular velocity is

$$\Omega_c = 13.1 \text{ rad s}^{-1}. \tag{3.7}$$

In summary, the magnetic and centrifugal forces are acting to oppose each other. If the right hand side of equation (3.6) changes sign, a real critical angular velocity no longer exists such that the system would be stable for all Ω. With this, we are able to perform our experiments with the following setup.

3.4 Experimental procedure

Once the cell was in the correct position located at $z = z_0 = 31.0$ mm, a mirror was placed above the magnet bore at 45° to the horizontal plane. A bright circular light source was placed at the bottom of the bore with a diffusive translucent disc underneath the cell to provide uniform lighting across the cell window. A high speed camera was placed at a distance of 2 metres outside the high magnetic field region, so as to not be affected by the magnetic field. To compensate for the distance between the camera and the cell, a system of two 40 cm focal length optical lenses, placed on a non-ferrous frame, was used to form an image of the cell at the focal point of the camera. The camera frame rate was varied between 200 and 400 frames per second, dependent upon the speed of rotation. The resolution remained constant at 512×512 pixels with each pixel corresponding to $9.1 \times 10^{-2} \pm 1.4 \times 10^{-5}$ mm. The experimental set up is shown schematically in figure 3.8. Once the images were captured, the data was post-processed using a MATLAB script in order to segment and extract the growth rate of perturbations of the interface. An additional MATLAB script was also implemented to determine the angular acceleration and angular velocity of the system. For this, a tracking shape in the form of a solid black circle was attached to the cell frame and illuminated by a light source placed above the magnet bore at an angle to reduce obstruction caused by reflections.

In order to induce rotation, a mechanical belt driven by a 24 V electrical motor was assembled underneath the cryomagnet, attached to a gear which held a shaft. The shaft was fixed to the cylinder holding the cell, applying rotation when the motor was on. The angular velocity of the system was controlled by a LabView program interacting with the motor power supply unit (PSU) through a National Instruments GPIB interface. The angular velocity will henceforth be denoted by Ω in figure 3.8, and should not be confused with electrical resistance in figure 2.8.

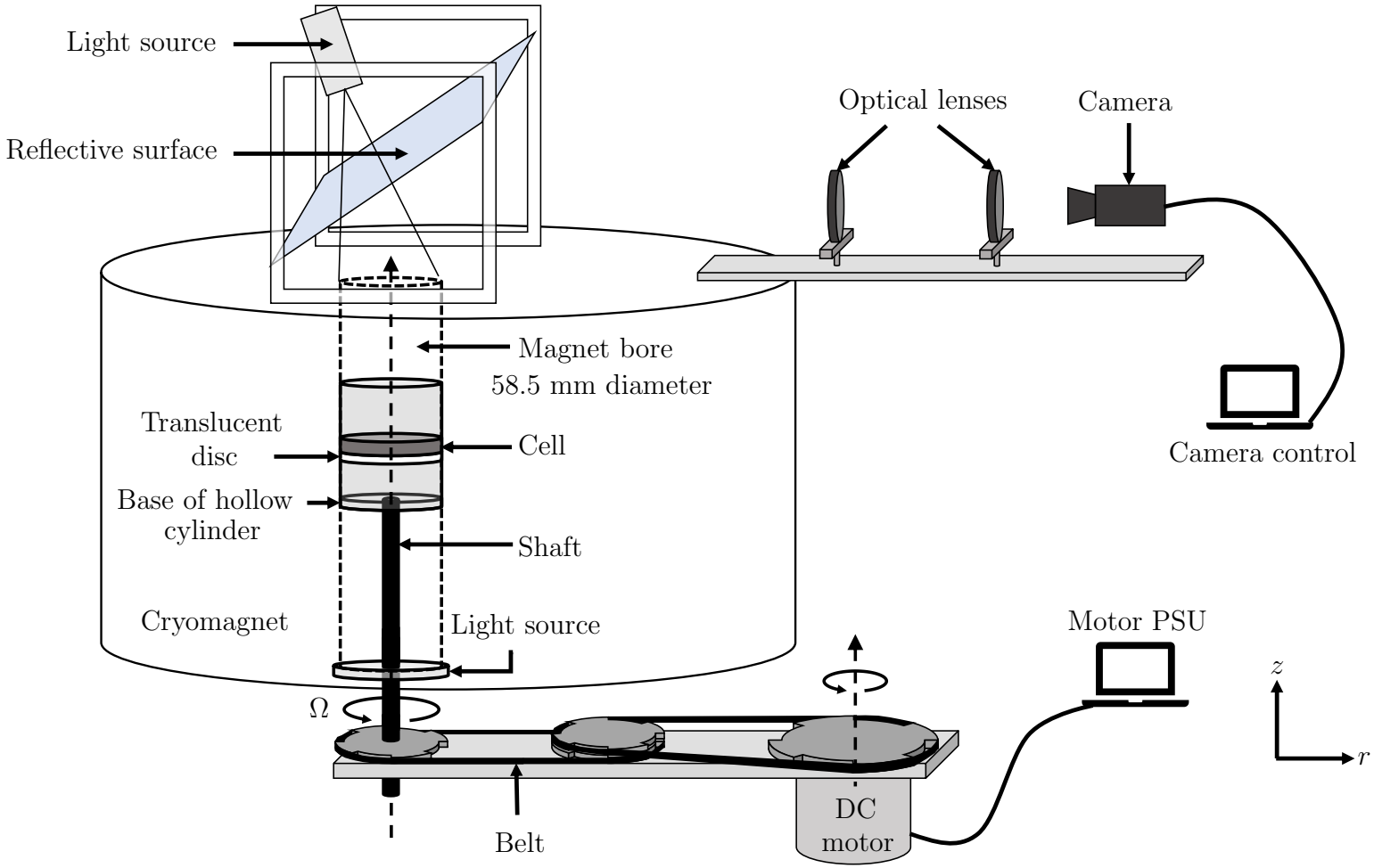

Figure 3.8: Schematic showing the experimental set up before performing the experiment.

Chapter 4

Data acquisition and analysis

4.1 Data acquisition and pre-processing

A high-speed Phantom camera was used to record each experiment using an "end trigger" which records for a designated amount of time in a looping buffer *before* the trigger is activated. The trigger was activated when the interface between the fluid phases can been seen to intersect the cell window boundary, as seen in figure 4.1, ensuring the instability event is captured.

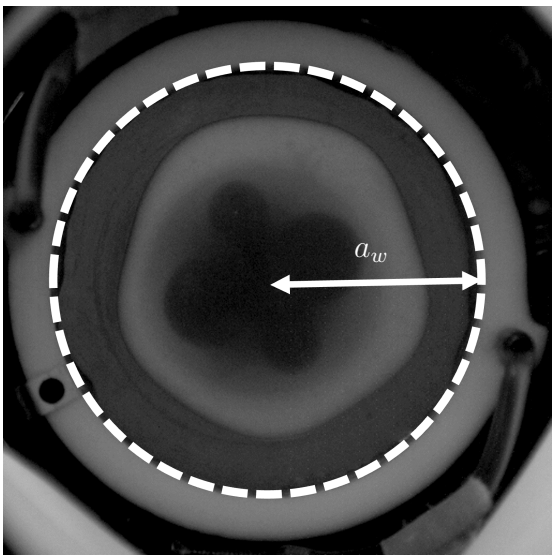

Figure 4.1: The window boundary is outlined by the white dashed line. The radius is $a_w = 18.10 \pm 0.03$ mm.

The open source software 'ffmpeg' was used to convert each video file into a

series of images, naming each graphic file consecutively and saved as '.png' graphic format, ready to be processed using a MATLAB scripts. Each image was cropped to eliminate the cell boundary which made edge detection simpler by 'removing' unwanted image data. Figure 4.2 shows the initial cropping process by setting the intensity values of the unwanted image pixels to zero, corresponding to black.

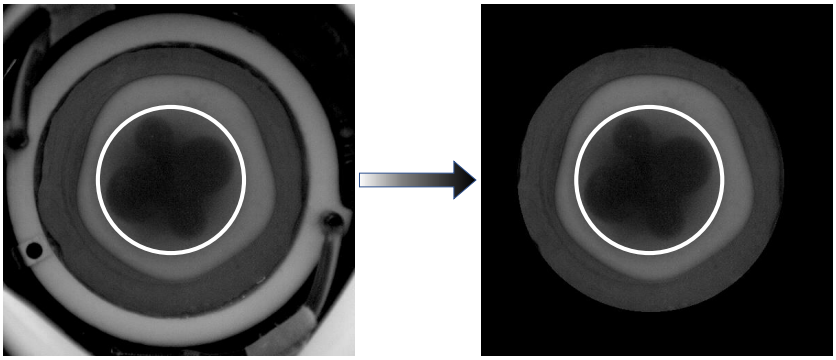

Figure 4.2: Setting the pixel intensity value to zero for all pixels beyond the cell window removes unwanted artefacts. The dark shape highlighted by the white circle is due to the shaft casting a shadow on the 'base of hollow cylinder' from figure 3.8; this does not influence the fluids. The inner, lightly contrasted fluid region is PC_{MC}, while the outer, darker contrasted fluid region is MC_{PC}.

To track the angular velocity of the cell over time, the images were similarly adjusted by leaving the pixels corresponding to the cell frame unchanged and setting all other pixel intensity values to zero, as shown in figure 4.3. This highlights a black dot attached to the cell frame which is used as a reference to measure angular velocity by tracking its path as it moves over time.

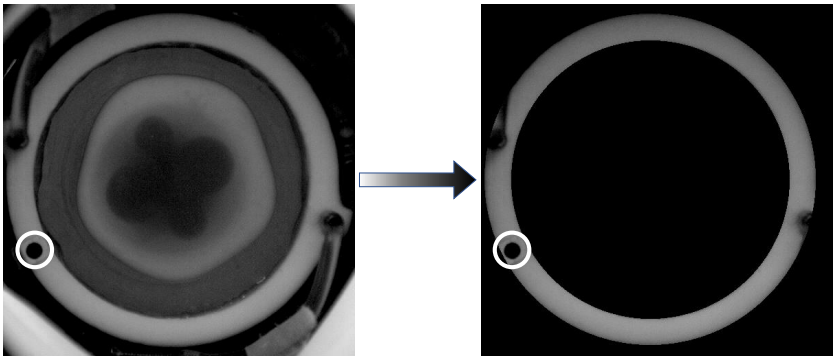

Figure 4.3: Setting the pixel intensity value to zero for all pixels which are not associated with the cell frame. The black dot highlighted by a white circle is the tracking reference used to find the angular velocity.

4.2 Image Processing - edge detection algorithm

The process of edge detection is an important step in the data analysis. The interface between the fluid layers forms an 'edge' in the images due to the contrast between the fluid layers in the camera images, as seen in figure 4.2 and 4.3. An 'edge' is defined as a position in an image where the local pixel intensity values change sharply, with a large gradient in a particular direction [9]. A widely-used edge detection algorithm is the Canny edge detector, and is considered to be one of the most rigorously tested algorithms, see Ding *et al.* [14] and references therein. The algorithm typically uses fixed parameters to find edges in an image. For a series of images, the algorithm becomes more complex if there are any fluctuations in ambient lighting.

Part of the experimental set up in chapter 3 involved placing a light source above the magnet bore at an angle to the vertical, in order to illuminate the top of the cell to track the motion of the black dot used to calculate angular speed (i.e. the magnitude of the angular velocity). This introduced some minor fluctuations in illumination of the interface due to reflection and also the non-uniformity of this light source, as the cell rotates. The implementation for the Canny edge detector became impractical to adjust for each image and so warranted an alternative method to detect the interface.

In our case, as a result of the pre-processing in the previous section, there are two contrasted regions from the two fluid phases. The edge detection problem simplifies to thresholding the images, i.e. converting the images to binary pixel intensity. All pixels above a threshold are assigned the value 255 (white), while all pixels below a threshold are assigned the value 0 (black) giving a binary image. The choice of threshold is important as it dictates the boundary of the inner fluid giving the interface. It must be noted that the threshold value is sensitive to variation in pixel intensity, and, as discussed, the pixel intensity

alters between each frame due to minor fluctuations. Additionally, each images contain high-frequency noise, obscuring the boundary between each fluid layer. This is typically seen by 'speckle noise' dispersed throughout each image. To reduce this noise before conversion to binary images, we used a spatial filter to average pixel intensity values with its neighbouring pixels.

A MATLAB script was written to extract the interface as a function of $r(\theta)$, where θ is the angle of rotation about the centre axis of the cell and $r(\theta)$ is the radial coordinate. The first step of this process is to apply a low-pass spatial filter to reduce the noise in each image [39]. This technique reduces the gradient of pixel intensity with its neighbours by passing low frequencies in the frequency domain using the two-dimensional Gaussian low-pass filter function

$$\mathrm{G}(x, y) = \mathrm{e}^{-\frac{x^2+y^2}{2\sigma^2}}, \tag{4.1}$$

where σ is the standard deviation distribution. The filter averages neighbouring pixels within an image giving greater weight to pixels towards the center of the filter window which varies in size according to the value of the variance, σ^2 [39]. The result, as shown in figure 4.4, is a reduction in image noise that would otherwise hinder edge detection techniques.

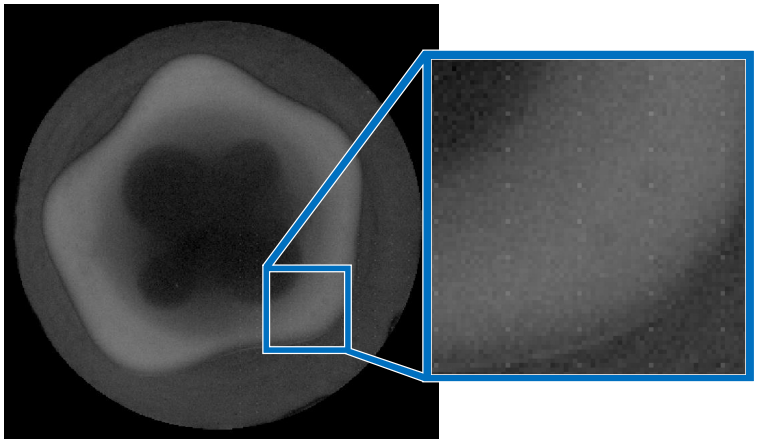

(a) Input image

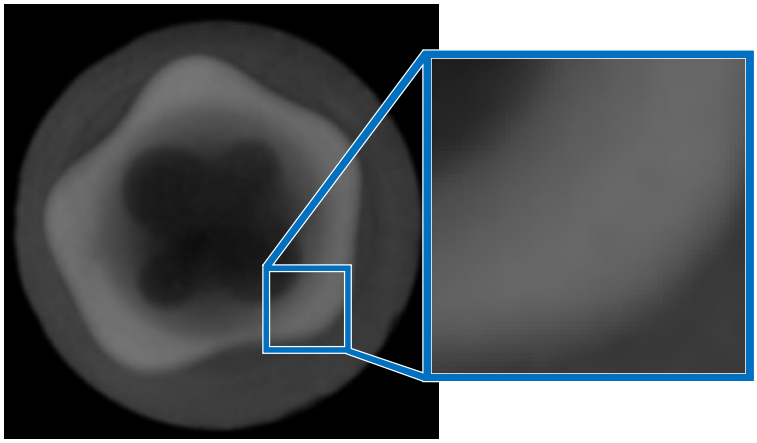

(b) Gaussian low-pass filter

Figure 4.4: Result of applying the Gaussian low-pass filter. In (a), there is noticeable noise in the form of white 'speckles' which could be the effect of the camera sensor. In (b), the speckle noise is averaged with neighbouring pixels, maintaining critical information such as contrast.

4.2.1 Determination of threshold values

The threshold value is important in the edge detection process. The light source above the magnet bore, in figure 3.8, creates fluctuations in pixel intensity as the cell rotates due to the applied current in the wires. Since we use a single threshold value for all frames in each experiment, it is important to choose the threshold value which best segments the fluid regions. To do this, we use the mass conservation of the fluids. As the fluids are restricted vertically, mass conservation results in an approximately constant area of each fluid phase in the images, under the assumption that the fluid flow is radial. To test whether light fluctuations

affected the edge detection process, we rotated the cell at sub-critical angular velocity. Under these conditions, we expect the interface to remain stable with a circular shape.

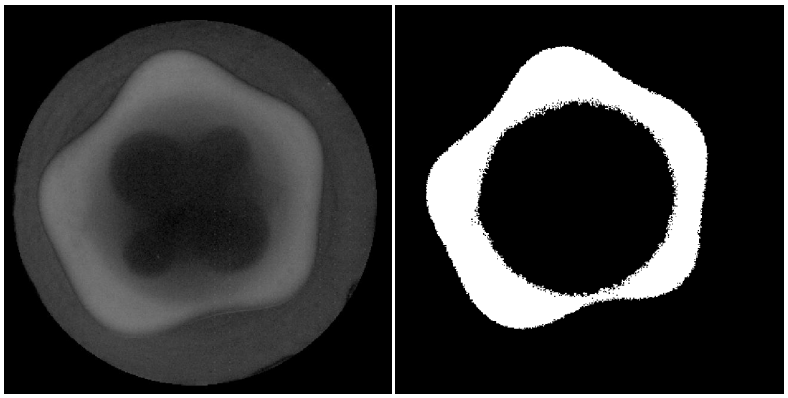

(a) Input image

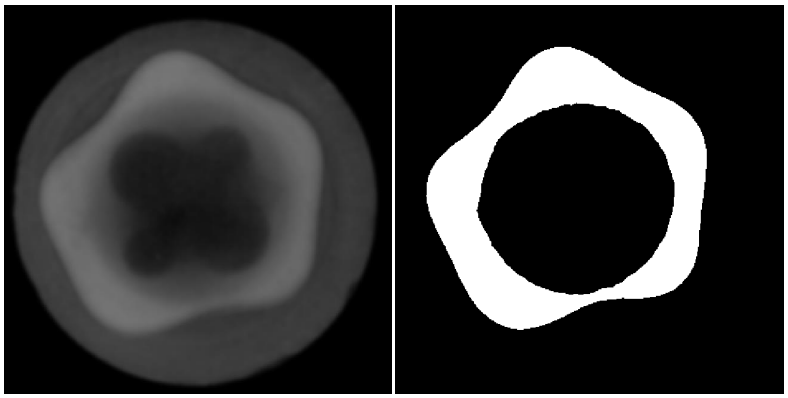

(b) Gaussian low-pass filter

Figure 4.5: Comparison of binarising an (a) input image and (b) filtered image. The boundary of (b) is noticeably less noisy than (a).

For each experimental video, a sample of image frames representing one full rotation of the cell was selected. For each image, a threshold value was manually chosen which could best binarise the image with the boundary as the interface. The average of the threshold values selected for each image was taken and applied to all frames of the video. The area of the white region of each frame was calculated as well as its arithmetic mean across all frames in the video. We found the standard deviation for each experiment to be no greater than 2% from the mean area, showing that the threshold values consistently segmented the fluid

regions without large deviations. Figure 4.5 shows the result of thresholding the final frame in one particular experiment. The method described above was used to find threshold values for each experiment with similar standard deviation in their values. The final stage of image processing was to extract the interface by first finding image contours.

4.2.2 Extracting image contours

A contour in image processing refers to a line joining all pixels with equal pixel intensity values. In binarising the images, the pixels associated with the inner fluid region (PC) are given a pixel intensity value of 255, corresponding to a white region as seen in figure 4.6a. The pixels in the binary image have intensity values which are either 0 or 255.

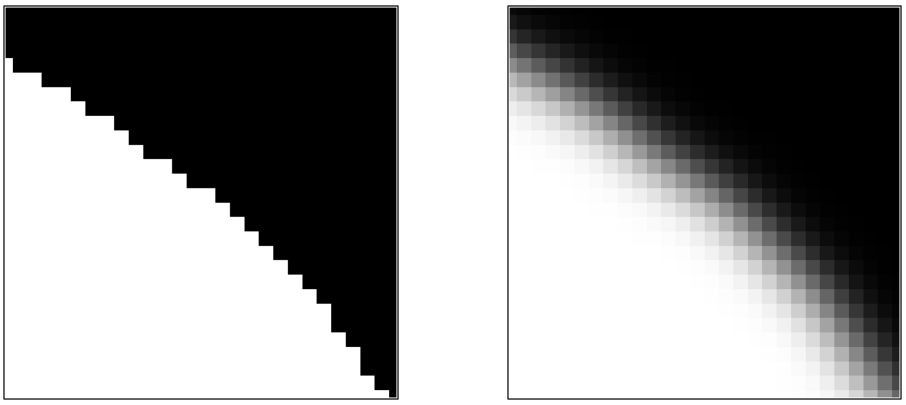

(a) Binarised image (b) Gaussian filter

Figure 4.6: (a) Binary image showing a boundary with pixel intensity either 0 or 255. (b) Gaussian filter is applied to average over neighbouring pixels at the boundary, giving pixel values between 0 and 255 inclusive, across the boundary.

As such, for a binary image without further filtering, there is ambiguity in choosing the correct contour as a result of the choice of threshold. This leads to a "rough" contour due to the pixelation of the boundary in the binary image. Finding a contour without an additional filter leads to the contour shown in figure 4.7a. The contour does not appear to align with the interface between the fluid layers in this case, leading to further processing of our images.

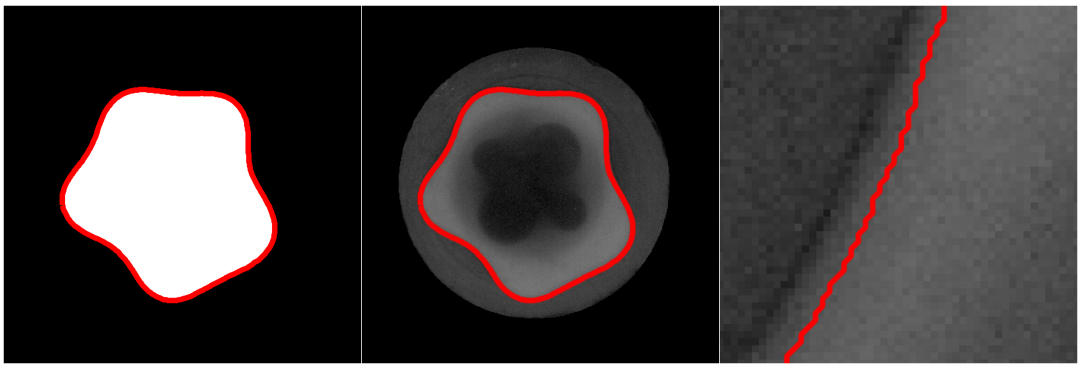

Binary input Contour overlay Inspection image

(a) Finding contour without filter applied to binary input

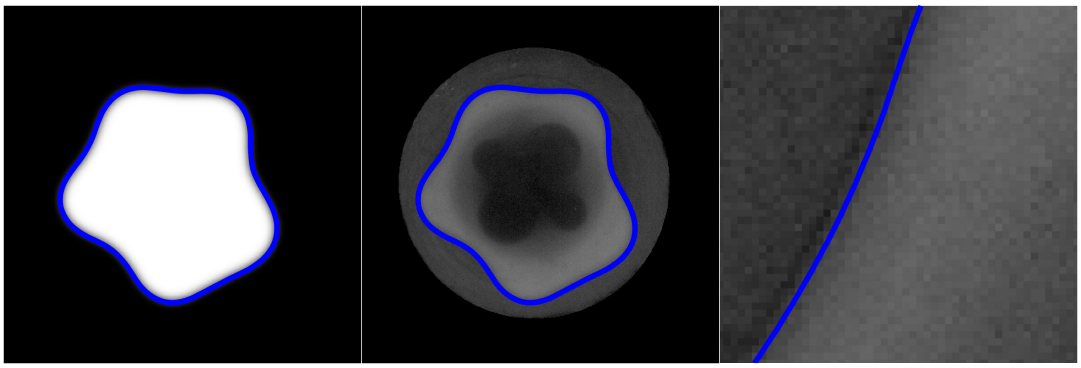

Binary input Contour overlay Inspection image

(b) Finding the contour with filter applied to binary input

Figure 4.7: Without, (a), and with, (b), a Gaussian filter to average neighbouring pixels at the boundary of the binary image.

Recalling that the Gaussian filter averages neighbouring pixel intensity values, applying the same filter to the binary images produce figure 4.6b. The pixels at the boundary are now averaged with their neighbouring pixels, using the uncertainty in threshold values to guide the intensity of the Gaussian filter applied. The pixel intensity within this region takes values between 255 and 0, providing a gradient from white to black respectively.

The contour level was chosen by finding a matching contour for a sample of images representing the full experiment. The selected contours for the present experiment deviated from their average by 4.8%. A possible source of this error is the effect of light fluctuations as the cell rotates. The sensitivity of varying the

Experiment	Mean contour level, pixel intensity	Percentage SD, %
1	74.3	3.8
2	75.6	1.3
3	58.4	4.8
4	49.1	5.3
5	60.0	3.5
6	77.2	3.8
7	81.4	1.2
8	79.9	3.3

Table 4.1: Standard deviation (SD) of mean contour level as a percentage. The mean contour level is similar in value for each experiment, but vary due to changes in brightness during experiments.

contour level within the error of 4.8% for a single image frame is shown in figure 4.8. On the left image, the contour error is indistinguishable in this case, but closer inspection highlights the associated error. Table 4.1 shows the associated

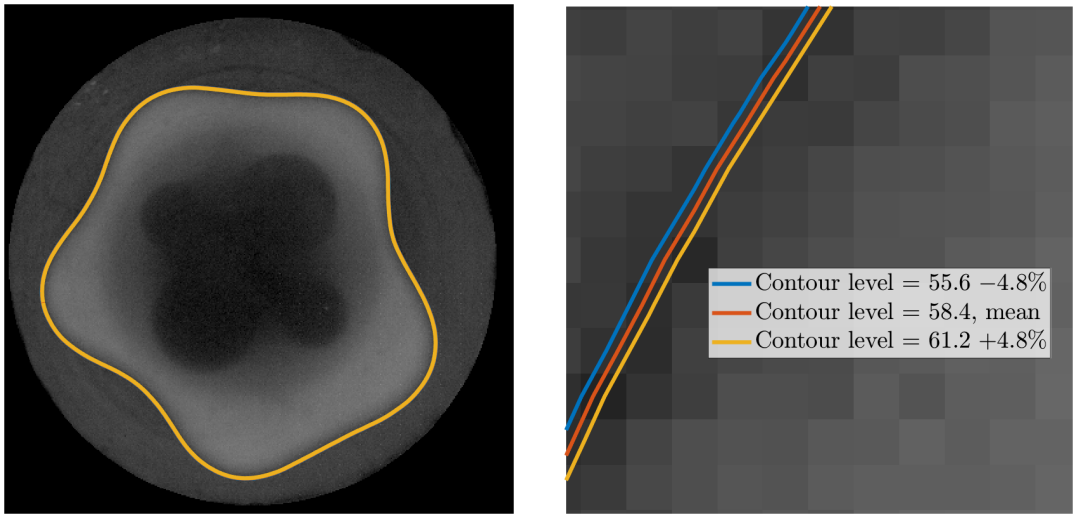

Figure 4.8: Change in contour level affects the extraction of the interface. The contours are superimposed onto the original images. By inspection, the image processing accurately isolates the interface between the inner and outer fluid regions.

percentage errors for various experiments performed.

The full results of the image processing techniques used here are shown in figure 4.9 for one particular experiment. We can see the progression in time of a sample experiment from the circular initial condition, to the onset of instability, and subsequent growth of the dominant wavenumber. The contour level remains

constant for each frame in the experimental video, and inspection of the original frame with the highlighted contour shows good agreement isolating the interface. The results are similar in other videos, meaning that we are in a position to extract the contour data and analyse the perturbations induced by rotation.

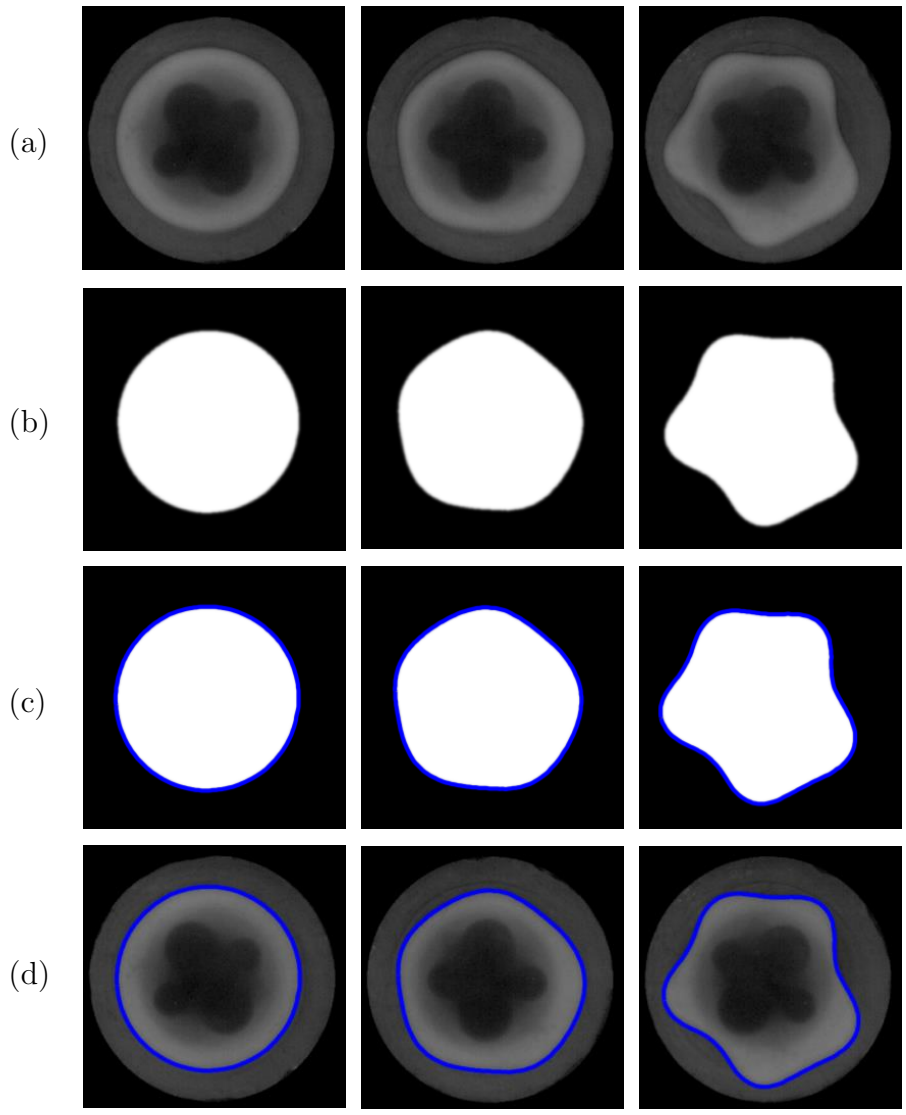

Figure 4.9: Progression of an experiment and the result of image processing. (a) Input image frames. (b) Gaussian blur of binarised image frames. (c) Contour extraction of interface. (d) Contour overlay on input image to show comparison.

4.2.3 Green's theorem: Converting extracted data into polar coordinates

The contours for each frame of an experimental video are now converted into a two-dimensional continuous function, in terms of the polar coordinates (r, θ). The area enclosed by the image contours are first found by using Green's theorem as

$$\iint_D \left(\frac{\partial Q}{\partial x} - \frac{\partial P}{\partial y} \right) \, \mathrm{dS} = \oint_{\partial D} P \, \mathrm{d}x + Q \, \mathrm{d}y, \tag{4.2}$$

for some closed contour ∂D with domain D, a two-dimensional Cartesian vector field $\mathbf{F}(x, y) = (P(x, y), Q(x, y))$ and surface element dS and where x, y are spatial coordinates. For a vector field of the form

$$\mathbf{F}(x, y) = \left(-\frac{y}{2}, \frac{x}{2} \right), \tag{4.3}$$

the left hand side of (4.2) reduces to the integral for the area of D, which can now be given by the line integral around the contour enclosing D, such that

$$A = \oint_{\partial D} P \, \mathrm{d}x + Q \, \mathrm{d}y = \frac{1}{2} \oint_{\partial D} x \, \mathrm{d}y - y \, \mathrm{d}x, \tag{4.4}$$

where A denotes the area of the domain enclosed by ∂D shown in figure 4.10.

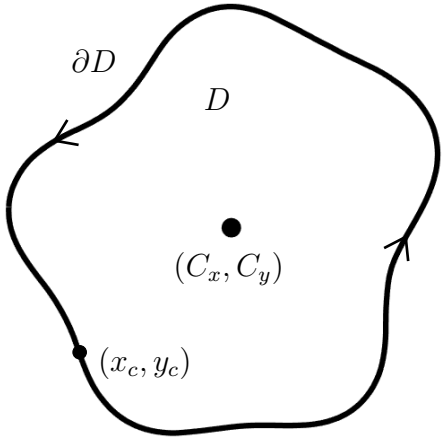

Figure 4.10: Closed contour from image processing. To find (C_x, C_y), Green's theorem is applied along the contour denoted by ∂D, where (x_c, y_c) denotes a point on the contour.

We are then able to calculate the centre of mass of the closed contour with the formulae

$$C_x = \frac{1}{A}\iint_D x \ \mathrm{dS}, \quad C_y = \frac{1}{A}\iint_D y \ \mathrm{dS}, \tag{4.5}$$

where $\mathrm{dS} = \mathrm{d}x\mathrm{d}y$ in Cartesian coordinates. Using Green's theorem once more, we can write the centroid coordinates in line integral form such as

$$C_x = \frac{1}{A}\int_D \frac{x}{2} \ \mathrm{d}x, \quad C_y = \frac{1}{A}\int_D -\frac{y}{2} \ \mathrm{d}y. \tag{4.6}$$

The centroid coordinates are used to find the radial distance between the centroid and the contour by

$$r = \sqrt{(C_x - x_c)^2 + (C_y - y_c)^2}, \tag{4.7}$$

where x_c and y_c are points on the contour. The associated angle, θ is found giving the polar form for each point on the contour using

$$\tan\theta = \frac{y_c - C_y}{x_c - C_x}.$$

The result is a sinusoid representing the extracted contour and, hence, the extracted interface. Figure 4.11 shows the progression of the interface in time in the form of the sinusoid. Originally, the extracted contours were found from the laboratory frame of reference. A rotation matrix was then applied to the contour data to transform the data to the rotating frame of reference. Hence, figure 4.11 shows the growth of each point of the fluid-fluid interface over time. Figure 4.12 is a complimentary figure to show the original images within the laboratory frame of reference. The coloured points show the start of the extracted contours seen in figure 4.11 and used to illustrate our data analysis methods.

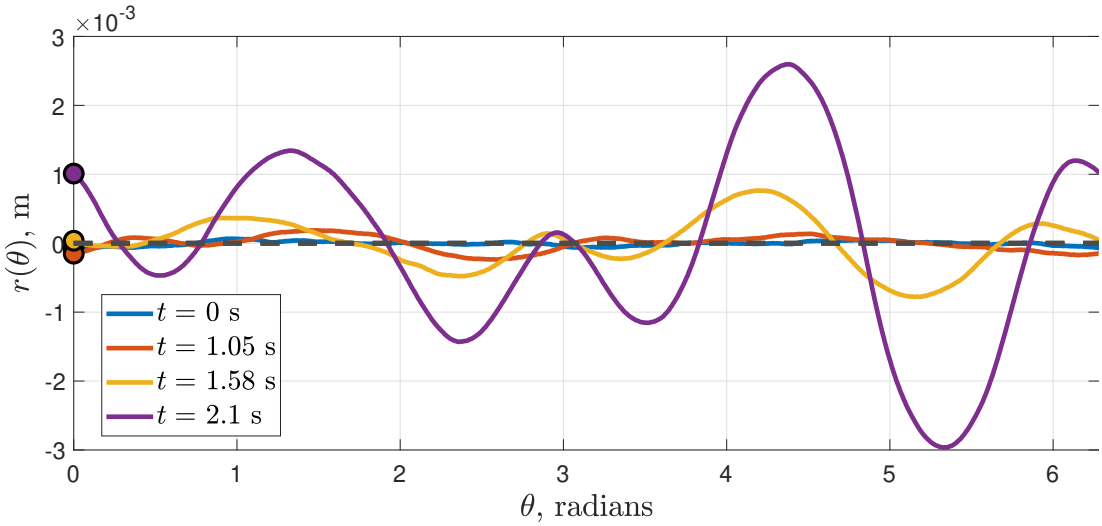

Figure 4.11: Evolution of the interface over time in the rotating frame of reference. The initial interface is represented by the $r = 0$ line at $t = 0$, and the coloured points show where the contour extraction starts and is complimentary to figure 4.12.

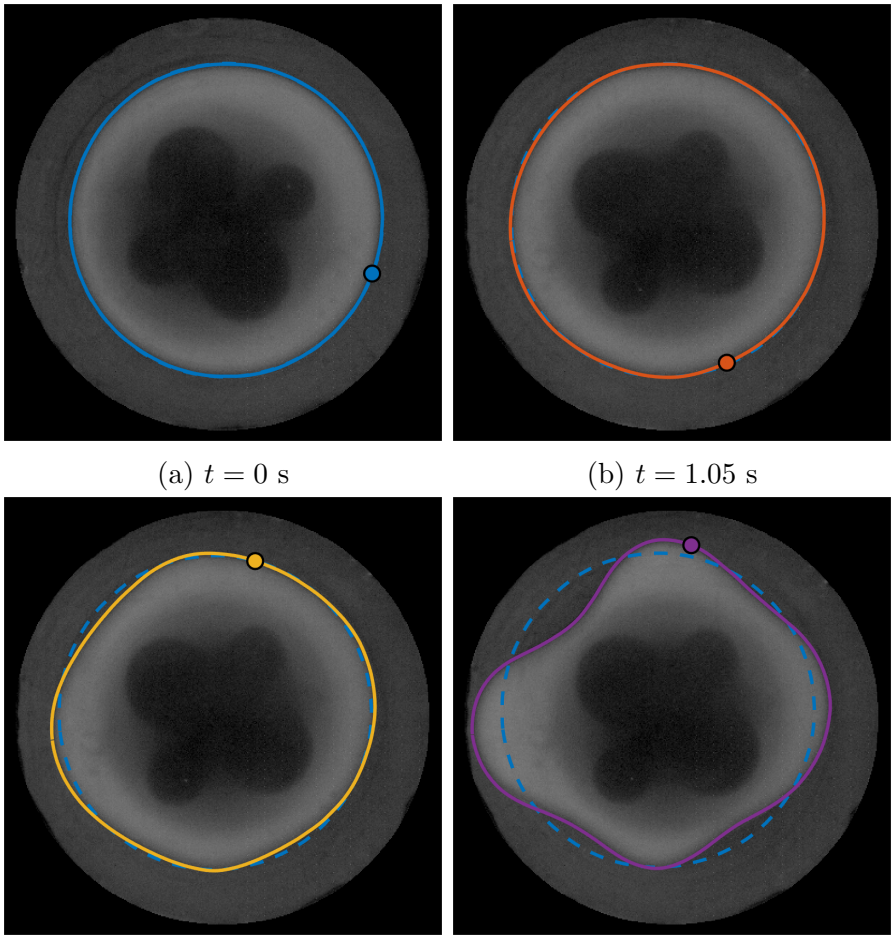

(a) $t = 0$ s (b) $t = 1.05$ s

(c) $t = 1.58$ s (d) $t = 2.10$ s

Figure 4.12: Original images with extracted interface as contours, and coloured accordingly with figure 4.11 in the laboratory frame of reference. The rotation is anticlockwise, as viewed from the camera. The dashed blue line is an overlay to compare each time with $t = 0$ s.

4.2.4 Measuring angular velocity

The cell was rotated using a 24 V DC motor attached at the base of the experimental set-up, as discussed in section 3.4. To measure the rotation rate, a marker was used as a tracker, which is indicated in figure 4.3. The centre of mass position of the marker was stored for each frame and the angular velocity was found by calculating the change in angular position per time step. Figure 4.13 shows the angular velocity-time graph for the example experiment discussed in this chapter. Other experiments follow the same procedure. Each experiment is slowly accelerated to $\Omega = 5$ rad s^{-1} and kept constant for a period of time to

initially set solid body rotation at sub-critical angular velocity. An acceleration is then applied to the system until a 'target' angular velocity is reached which is where the analysis of the instability takes place. The critical angular velocity for which the centrifugal force becomes greater in magnitude than the magnetic body force, calculated by (3.6), is marked on the graph. The highlighted region indicates a stage of acceleration in which the angular velocity is increased from $\Omega = 13.1$ rad s^{-1} to a target value of $\Omega > \Omega_c$.

The acceleration of the cell is discrete; a voltage was increased stepwise using a LabView program resulting in a step function for the angular velocity. Table 4.2 lists the range of angular velocities reached over the course of eight experiments. The percentage uncertainties are shown in table 4.2 were calculated from the variation over repeated experiments.

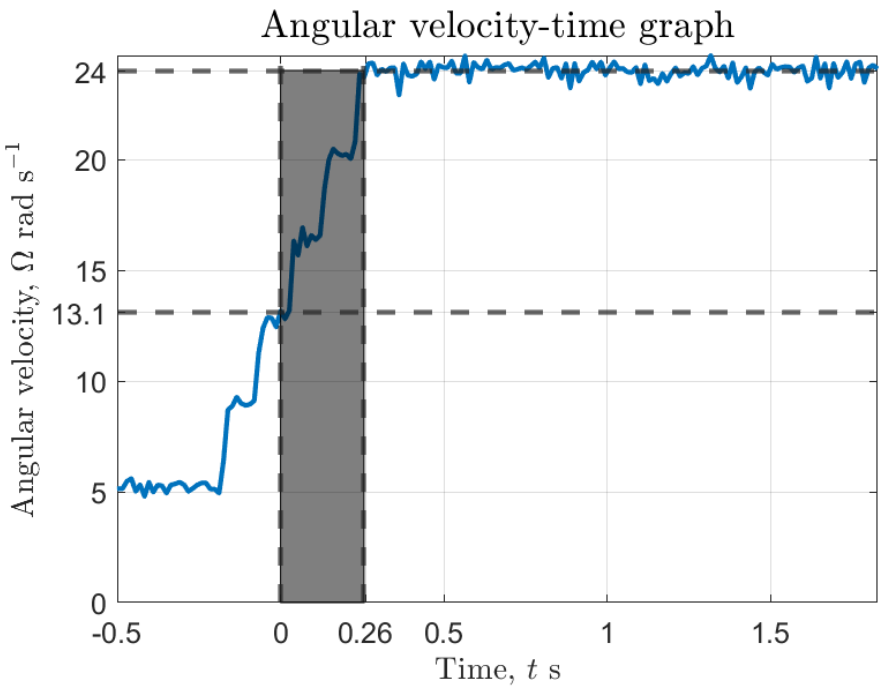

Figure 4.13: Angular velocity over time. The horizontal dashed lines show the critical angular velocity and target angular velocity, $\Omega_c = 13.1$ rad s^{-1} and $\Omega = 24.0$ rad s^{-1} respectively. The highlighted grey region represents the region of acceleration the experiment undergoes before reaching Ω_c

Experiment No.	Maximum angular velocity, Ω rad s^{-1}	% uncertainty
1	18.5	3.5
2	21.3	3.1
3	24.0	3.1
4	25.2	3.2
5	26.7	2.8
6	29.3	2.7
7	29.9	2.0
8	30.6	2.0

Table 4.2: List of experiments performed, with their associated maximum angular velocities and uncertainties.

4.3 Fourier decomposition

In the previous section, we showed how the fluid-fluid interface contours can be extracted from each image frame and converted into a continuous sinusoid. We now analyse the sinusoid using Fourier analysis.

With most[1] periodic, piecewise continuous functions, there exists a Fourier series form, a sum of trigonometric functions, and expressed mathematically as

$$R(\theta) = \frac{a_0}{2} + \sum_{m=1}^{\infty} \{a_m \cos(m\theta) + b_m \sin(m\theta)\}, \tag{4.8}$$

where $R(\theta)$ is a periodic function, $\theta \in [-\pi, \pi)$, and a_m, b_m are the Fourier coefficients associated with wavenumber m. The Fourier coefficients are determined

[1] A Fourier series representation of a function exists if the function satisfies the Dirichlet conditions [25]

by the integrals

$$a_m = \frac{1}{\pi}\int_{-\pi}^{\pi} R(\theta)\cos(m\theta)\ \mathrm{d}\theta,$$
$$b_m = \frac{1}{\pi}\int_{-\pi}^{\pi} R(\theta)\sin(m\theta)\ \mathrm{d}\theta.$$

To represent the contours extracted by the process outlined in section 4.2.3 as a Fourier series, we truncate the series by approximating with $2N+1$ terms

$$R(\theta) \approx \frac{a_0}{2} + \sum_{m=1}^{N}\{a_m\cos(m\theta) + b_m\sin(m\theta)\}, \tag{4.9}$$

The choice of N was automatically chosen for each frame to give a root mean squared error between the extracted interface and Fourier series representation less than an error tolerance of 10^{-2}, with $N \sim \mathcal{O}(10^2)$.

The growth rate of the amplitude of each wavenumber in the experiments can then be determined by finding the amplitude of each wavenumber at each time step, where the time step is defined by

$$t_s = \text{time step} = \frac{1}{\text{frames per second}}. \tag{4.10}$$

The amplitude for each wavenumber is given by

$$A_m = \sqrt{a_m^2 + b_m^2}, \qquad \text{for } m > 0, \tag{4.11}$$

We measure A_m as time progresses throughout each experiment. The growth rates are then found from the change in amplitude over time.

4.4 Interfacial growth

Figure 4.15 is a plot of the logarithm of the amplitude with wavenumbers m showing exponential growth, as might be anticipated for a small linear perturba-

tion. As such, curves of the form

$$f(t) = \alpha e^{\omega t}, \tag{4.12}$$

are fit to the experimental data, where α is the initial amplitude of disturbance and ω is the growth rate. The horizontal line shows the noise level defined by the oscillations observed in the data. The noise level is defined to be the maximum amplitude of oscillation before the onset of instability; during the acceleration phase when the angular velocity is sub-critical, for $t < 0$. We found that wavenumbers $2 \leq m \leq 6$ exhibited amplitudes exceeding the noise level.

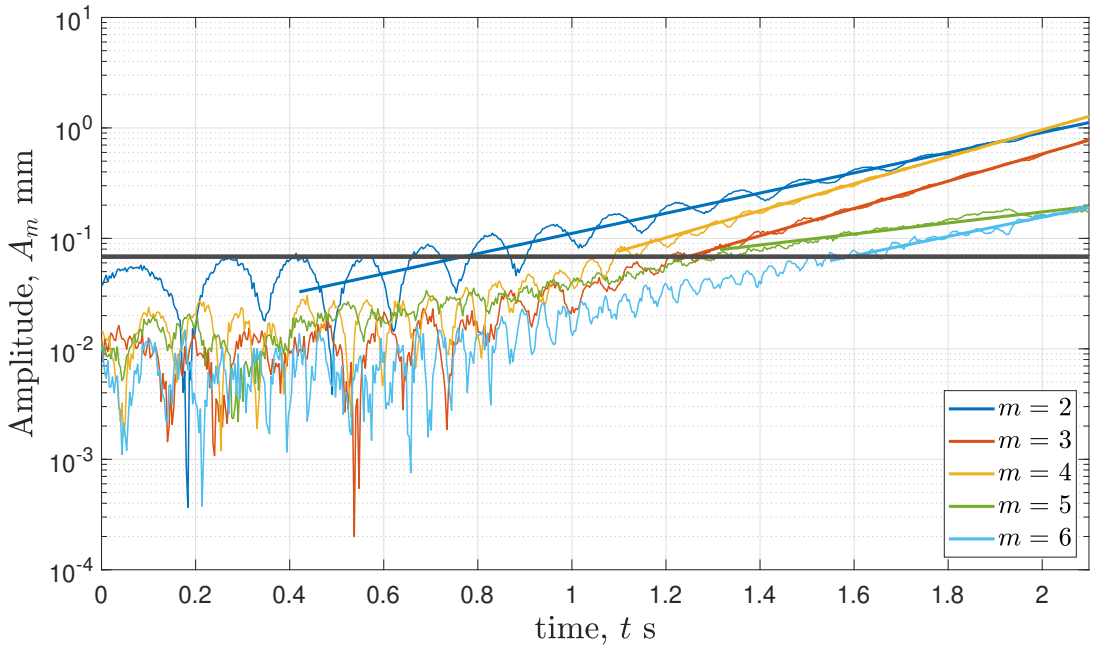

Figure 4.14: Amplitude vs. time, logarithmic plot.

Figure 4.15: Logarithmic plot of amplitude vs. time with target angular velocity $\Omega = 24.0$ rad s^{-1}. The noise level is again shown by the solid black line. Below noise level, the amplitude rapidly approaches 0 causing large oscillatory behaviour during the early time stage of growth.

Figure 4.15 is the associated logarithmic plot for the amplitude A_m. There are two areas of notable change in this graph. Below the noise level, indicated by the solid black line, the amplitudes appear to fluctuate rapidly. However, this phenomenon occurs when the wave amplitudes are less than a pixel in magnitude.

At this scale our measurements are limited by our camera resolution. We proceed by neglecting this phase when considering the growth of the wave. Above the noise floor the logarithm of the amplitude increases linearly with time.

The amplitudes extracted from the Fourier representations, at $\Omega = 24.0$ rad s^{-1}, are shown in the corresponding plot in figure 4.16 by dashed lines, and their fitted curves of the form (4.12) are shown in their respective solid lines. Our investigation is unable to conclusively prove a single source of the observed oscillations. However, as the cell rotates, the amplitude of each wavenumber of the interface oscillates periodically and proportionally to the angular velocity of the cell, indicating that lighting is one source for fluctuations causing the oscillations in our data. Further experiments will allow for further investigation into the source of the oscillations and implementations needed to reduce or eliminate them.

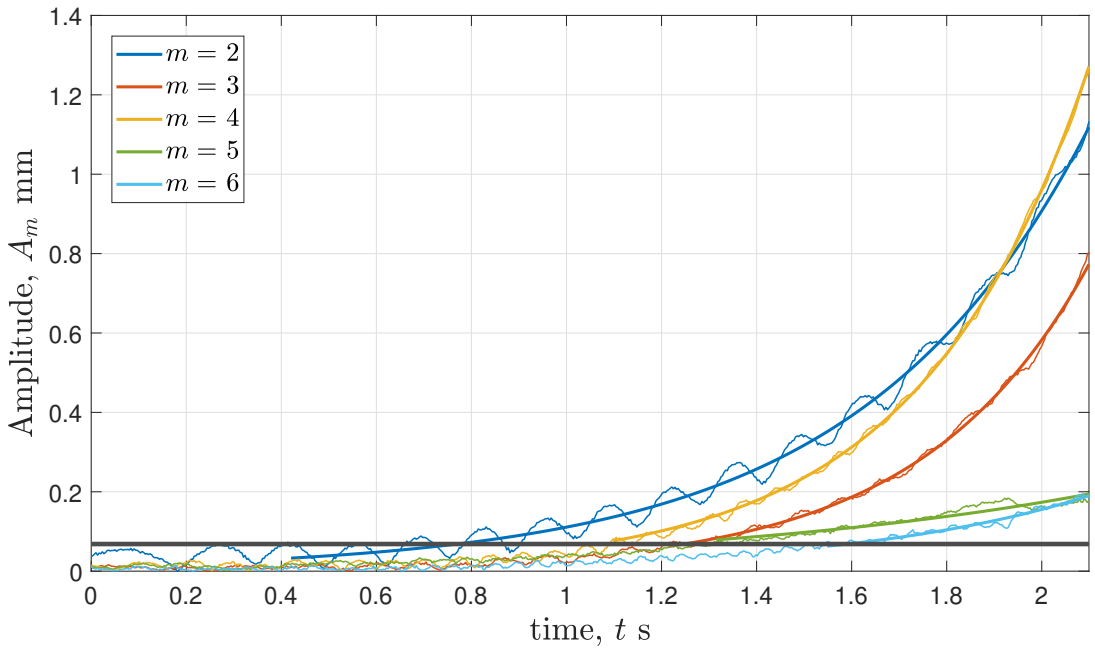

Figure 4.16: Complimentary exponential plot to figure 4.15. Amplitude, in millimeters, of wavenumbers $m = 2, ..., 6$ with an exponential fit. The fitted lines are shown in solid coloured lines, while the original data is shown as dashed lines.

Comparison of figure 4.15 with the final frame of the experiment shown in figure 4.12, shows that $m = 4$ is the most prominent wavenumber. This can be seen by an asymmetric 4-lobed shape in the image. However, measurement of lower order

wavenumbers, such as $m = 2, 3$ in this example, also show an expected significant contribution to the instability from these modes. The contributions are expected to come from the angular acceleration present when $\Omega > \Omega_c$, as discussed by Carillo *et al.* [11]. When the target angular velocity is reached, lower order wavenumbers are excited during acceleration and may be in a position to have a significant contribution to the instability in amplitude as they exhibit growing instability earlier in time than the most unstable wavenumber associated with the target angular velocity.

Ω, rad s^{-1}	$m = 2$		$m = 3$		$m = 4$		$m = 5$		$m = 6$	
	RMSE	R^2, %	RMSE	R^2, %	RMSE	R^2, %	RMSE	R^2, %	RMSE	R^2, %
18.5	0.29	70	0.15	30	0.18	26	-	-	-	-
21.3	0.28	93	0.056	99	0.075	91	0.0064	62	-	-
24.0	0.26	93	0.067	96	0.072	97	0.038	98	0.093	71
25.2	0.36	78	0.047	98	0.038	99	0.027	99	0.057	89
26.7	0.41	75	0.12	84	0.080	98	0.037	09	0.077	66
29.3	0.51	89	0.041	99	0.081	99	0.033	99	0.062	95
29.9	0.44	59	0.061	99	0.086	98	0.034	99	0.033	95
30.6	0.45	67	0.068	98	0.072	99	0.034	99	0.040	99

Table 4.3: Root-mean-squared-error (RMSE) and R^2 goodness-of-fit measure for linear fitting in the logarithmic scale of amplitude data for wavenumbers $m = 2, ..., 6$.

To quantify the reliability of the fitted curves, we first convert the data points to a logarithmic scale as shown in figure 4.15. By transforming (4.12) into a logarithmic scale we obtain

$$F(t) = \ln \alpha + \omega t, \tag{4.13}$$

which is the equation for a straight line with gradient ω. We now fit the transformed data with the linear regression model provided by (4.13) and use two goodness-of-fit measures, displayed in table 4.3, to evaluate the reliability of the chosen fit model.

The root-mean-squared-error statistic measures the concentration of data points about the predicted exponential model, and are calculated by

$$\mathrm{RMSE} = \sqrt{\sum_{i=1}^{N} \frac{\left(A_m(t_i) - f(t_i)\right)^2}{N}}, \tag{4.14}$$

where t_i is the i-th time for data point i, $A_m(t)$ is the function of amplitude for wavenumber m, N is the number of data points associated with $A_m(t)$, and $f(t)$ is the exponential curve of best fit. A model of best fit will have a RMSE value of 0, if it perfectly fits the observed data points. In table 4.3 we see that, for $\Omega \geq 21.3$ rad s^{-1} and $m \geq 3$, RMSE < 0.1 showing the concentration of data points is close to the linear regression lines of (4.13). For $m = 2$, as well as when $\omega = 18.5$ rad s^{-1} we see greater deviation from the line of best fit.

Another statistic we use is the R^2 which is calculated by

$$\mathrm{R}^2 = 1 - \frac{\sum_{i=1}^{N} \left(A_m(t_i) - f(t_i)\right)^2}{\sum_{i=1}^{N} \left(A_m(t_i) - \bar{A}_m\right)^2}, \tag{4.15}$$

where $\bar{A}_m$ is the mean of the observed amplitude data for wavenumber m. The R^2 is a percentage explaining the variation of the data around a linear model. Therefore, high R^2 values tell us that the chosen fit model explains a large proportion

of the variation in data. We can see that for $\Omega = 18.5$ rad s^{-1} and $m = 3, 4$, we report $R^2 \leq 30\%$. We must conclude that the chosen linear model is not the best choice to fit the associated data. It is inappropriate to suggest that the growth of modes $m = 3, 4$ can be modelled by an exponential function for the experiment with target angular velocity $\Omega = 18.5$ rad s^{-1}. However, for $\Omega \geq 21.3$ rad s^{-1} and $m \geq 3$, the R^2 is consistently above 95%. Therefore, in combination with RMSE, it is reasonable to suggest that the linear model in (4.13) is an appropriate choice overall.

4.5 Experimental results

With the method of data analysis detailed in the preceding sections, the results of the experiments are now presented. Table 4.4 gives a summary of the experimental parameters used throughout all of our experiments.

Experimental quantity	Value	Units
ρ_1	1181.0	kg m^{-3}
ρ_2	1048.3	kg m^{-3}
η_1	2.8×10^{-3}	Pa s
η_2	1.0×10^{-3}	Pa s
χ_1	9.6×10^{-6}	Dimensionless
χ_2	-4.9×10^{-6}	Dimensionless
r_0	13.1	mm
b	1.80	mm
a	19.1	mm
γ	2.8	mN m^{-1}
$\frac{\partial B^2}{\partial r}\Big\vert_{\substack{r=r_0 \\ z=z_0}}$	74.7	T^{2}m^{-1}

Table 4.4: Summary table of experimental parameters measured in chapter 3.

Figure 4.17 shows the growth rate of each wavenumber with contributions to the interface, whose amplitude surpasses the noise floor discussed in section 4.4.

We found that the amplitude for $m \geq 7$ did not surpass the noise floor and are removed from our discussion. For each mode, the shading of the markers indicate the value of the angular velocity. Each shaded group represents a repetition of the same experiment without changing experimental parameters. At lower angular velocity, $\Omega \lesssim 25.2$ rad s^{-1}, the growth rate for modes $m \geq 4$ do not exceed the noise floor. The radial forces exerted on the fluids by the magnet suppress the growth of these wavenumbers. Larger velocity is required to induce higher order wavenumber growth.

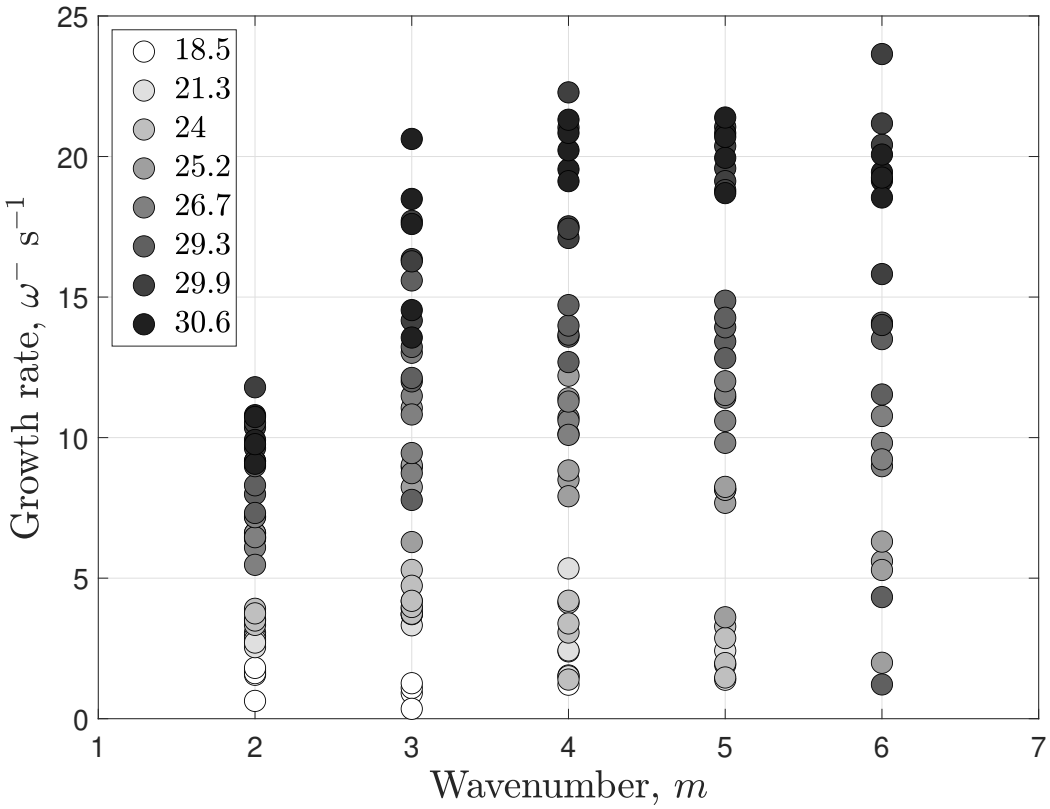

Figure 4.17: The growth rates for wavenumbers $m = 2, 3, 4, 5, 6$. The angular velocity is represented by the shading of the data points, increasing as the points get darker in colour.

The regression model used in figure 4.15 allows us to extract the growth rates from the amplitude data. The growth rates are found for each wavenumber by taking the gradient of the associated regression lines. Table 4.5 shows the growth rate of each mode for increasing angular velocity. The uncertainties are found by repeating each experiment with the same parameters.

	Angular Velocity (Ω)															
	18.5		21.3		24.0		25.2		26.7		29.2		29.9		30.6	
m	ω	$\delta\omega, \%$	ω	$\delta\omega, \%$	ω	$\delta\omega, \%$	ω	$\delta\omega, \%$	ω	$\delta\omega, \%$	ω	$\delta\omega, \%$	ω	$\delta\omega, \%$	ω	$\delta\omega, \%$
2	0.47	3.3	1.1	< 1	2.1	1.1	2.1	3.0	2.7	3.2	3.1	4.7	3.2	4.3	3.6	4.1
3	0.29	26.0	1.4	1.0	2.8	3.2	3.4	2.3	3.9	7.6	5.0	1.1	5.4	3.8	5.4	2.1
4	0.39	23.0	1.0	1.6	3.1	2.6	3.4	< 1	4.4	1.5	5.5	1.7	6.4	3.1	6.6	1.4
5	-	-	0.76	18.0	2.3	1.0	3.5	< 1	4.4	1.2	6.1	< 1	6.5	1.1	6.6	1.2
6	-	-	-	-	1.5	11.0	3.1	8.5	2.8	12.0	5.3	5.5	6.1	1.1	7.0	1.6

Table 4.5: The growth rates of each wavenumber, m, are given by ω with units rad s^{-1} and their associated percentage uncertainties denoted by $\delta\omega$. Large uncertainty is recorded for higher wavenumbers when the angular velocity is low.

In figure 4.18 the fastest growing wavenumber is extracted from all data collected from our experiments at various angular velocities, Ω. At each value of the angular velocity, there are multiple data points which indicate the repetitions performed for the associated Ω. We can see a steady increase in the fastest growing wavenumber for increasing Ω, as may be expected from introducing greater radial forces in the system. However, at higher Ω, the data 'levels out', suggesting a limit on the fastest observable wavenumber. There are two possible conclusions for this. The first is that there exists a limit on the fastest growing wavenumber for the experimental setup outlined in chapter 3, providing a valuable argument for the implementation of larger angular velocity in future experiments. A second conclusion is that the relationship between the fastest growing wavenumber and angular velocity is non-linear, leading to the need for further analytical study, as is the topic of the next chapter.

Figure 4.19 shows images from eight experiments performed over a range of Ω. Comparison with figure 4.18 shows consistent recording of the expected fastest growing mode as seen in figure 4.19. The asymmetric growth of the interface is due to the growth of multiple wavenumbers as a consequence of lower wavenumber excitation during the acceleration phase, see figure 4.13. An important piece of information we can collect from our data is the most dominating wavenumber, i.e. the mode with the fastest growth rate at each target Ω.

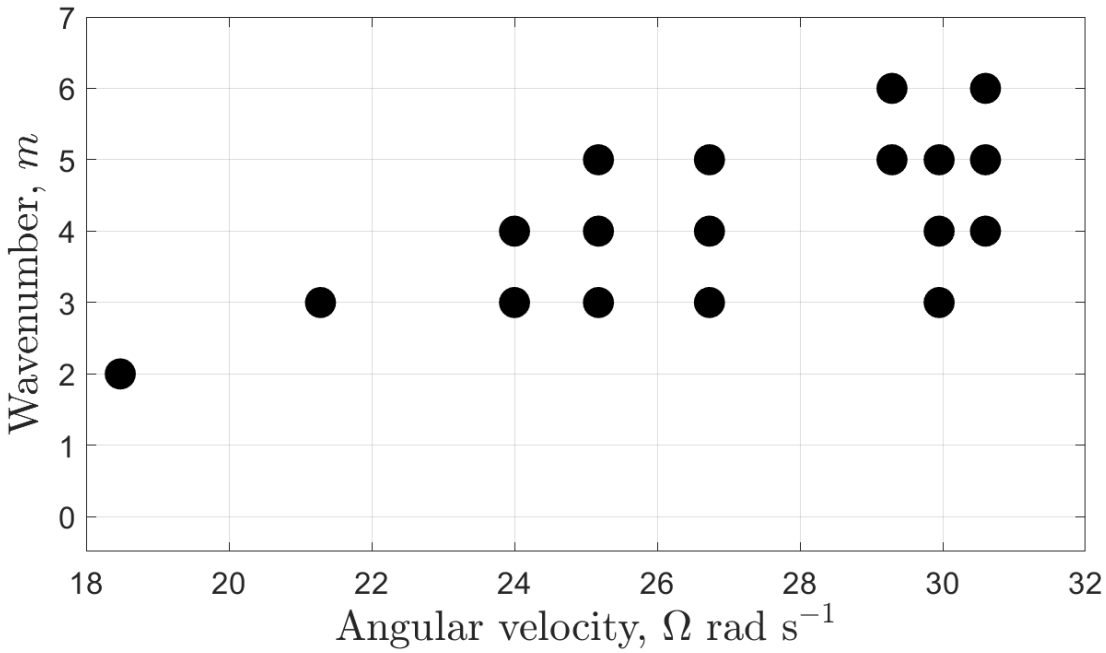

Figure 4.18: Graph showing the fastest growing wavenumber at eight different angular velocities. There are five data points within a 'group' of points at each Ω, representing five experimental repetitions for every Ω investigated.

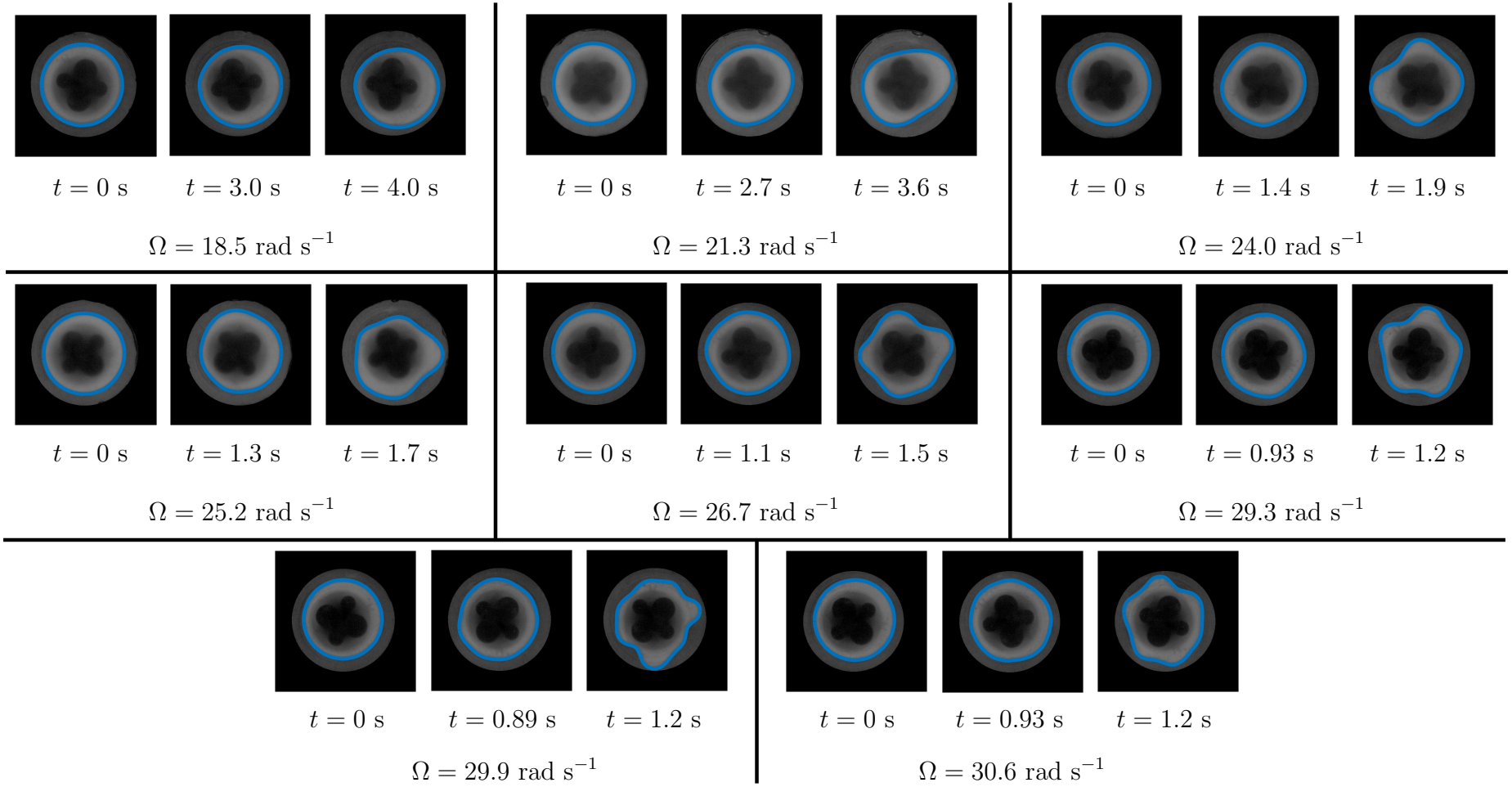

Figure 4.19: Image results of experiments at three time stamps to show progression of each experiment. The second time stamp at each Ω is 75% past $t = 0$ to show onset of instability.

4.6 Summary

Throughout this chapter we have detailed the procedure from data collection to data analysis of our experimental results. We applied dye to the outer fluid in order to create a strong contrast between the fluid layers, as well as removing unnecessary image data during the pre-processing stage set out in section 4.1. We then applied closed contour techniques to extract the interface data and represent them by an approximated Fourier representation.

By plotting the logarithm of the amplitude for each wave mode as a function of time (figure 4.15), we were able to observe linear growth when the amplitude of each mode surpassed the noise floor. We applied linear regression analysis to extract the growth rate as given by the gradient of the associated line-of-best-fit. The growth rates for each mode are then presented in table 4.5. The increasing angular velocity gives greater growth rates for wave modes, as might be anticipated on the grounds of greater centrifugal force directed radially towards the magnet coils. The most unstable wavenumber for each angular velocity can then be determined looking for the mode with the fastest growth rate, as shown in figure 4.18. With this data, we are able to proceed to look at the predictive models used and to ascertain verification of a linear perturbation model.

Chapter 5

Two-dimensional analysis in rotational geometry

To begin our theoretical analysis, we look at interfacial perturbations within a circular domain, bound by an impermeable boundary. Much of what is discussed in this chapter will be a review of the derivation of the governing model necessary for analysing the behaviour of two-dimensional interfacial instabilities in circular domains. The model shall be restricted to the discussion of two incompressible fluids and their shared interface.

In this chapter, we derive a general two-dimensional model with instantaneous constant angular velocity. We then linearly perturb the hydrostatic background solution by method of normal modes to find conditions for stability for inviscid flow. By investigating inviscid flow, we are able to introduce the main modelling techniques used to analyse the fluid flow, as well as investigating the key concepts of radial stability through the analysis of the contributing physical forces at work, without cause for concern with regards to viscosity. Later, in chapter 6, the similarities between the inviscid and viscous solution will be discussed,

5.1 The governing equations

We first consider the underpinning assumptions that build the foundations of the model. One critical assumption is that the flow is assumed to be incompressible. Physically, we mean that for a parcel of fluid in the flow, the density of the fluid parcel remains constant for all time. Mathematically, this is the mass conservation equation

$$\frac{\mathrm{D}\rho}{\mathrm{D}t} + \rho\boldsymbol{\nabla}\cdot\mathbf{u} = 0, \tag{5.1}$$

which is reduced to the well-known incompressibility condition

$$\boldsymbol{\nabla}\cdot\mathbf{u} = 0, \tag{5.2}$$

where ρ is the constant fluid density, $\mathbf{u} = (u(\mathbf{r},t), v(\mathbf{r},t), w(\mathbf{r},t))$ is a fluid velocity field, with $\mathbf{r}$, t the spatial vector and time dependence, respectively.

$$\frac{\mathrm{D}}{\mathrm{D}t}f(\mathbf{r},t) = \frac{\partial}{\partial t}f(\mathbf{r},t) + (\mathbf{u}\cdot\boldsymbol{\nabla})f(\mathbf{r},t)$$

is the material derivative which, when applied to some scalar quantity $f(\mathbf{r},t)$, describes the rate of change of $f(\mathbf{r},t)$ within a given fluid parcel as it moves with the fluid. Equation (5.2) is a consequence of mass conservation for incompressible fluids and forms one of the conditions which must be satisfied for a velocity vector field $\mathbf{u} = \mathbf{u}(\mathbf{r},t)$. Initially, we assume the fluid flow is two-dimensional with $\mathbf{u} = (u(\mathbf{r},t), v(\mathbf{r},t), 0)$ and is also isothermal.

The Navier-Stokes momentum equation for an incompressible non-inert fluid within a rotating reference frame is expressed as

$$\frac{\mathrm{D}\mathbf{u}}{\mathrm{D}t} = -\frac{1}{\rho}\boldsymbol{\nabla}p - \boldsymbol{\Omega}\wedge(\boldsymbol{\Omega}\wedge\mathbf{r}) - 2\boldsymbol{\Omega}\wedge\mathbf{u} + \frac{\eta}{\rho}\nabla^2\mathbf{u} + \mathbf{F}, \tag{5.3}$$

where $p = p(\mathbf{r},t)$ is the pressure field and $\boldsymbol{\Omega} = (0,0,\Omega)$, $\mathbf{F} = \mathbf{F}(\mathbf{r},t)$ are vector fields which represent the constant angular velocity of the fluid domain centred

about the origin at $\mathbf{r} = (0, 0, 0)$, and any additional external body forces, respectively. Typically, the body force due to gravitational effects are included in the vector field $\mathbf{F}$. Though, as shown in chapter 2, gravitational effects have been neglected by exploiting vertical points of equilibrium in solenoid magnet, meaning that $\mathbf{F}$ will only include the radial component of the magnetic body force, which has been derived in chapter 2. The momentum equation can then be written as

$$\frac{\mathrm{D}\mathbf{u}}{\mathrm{D}t} = -\frac{1}{\rho}\boldsymbol{\nabla} p - \boldsymbol{\Omega} \wedge (\boldsymbol{\Omega} \wedge \mathbf{r}) - 2\boldsymbol{\Omega} \wedge \mathbf{u} + \frac{\eta}{\rho}\nabla^2 \mathbf{u} + \frac{\chi}{2\mu_0}\frac{1}{\rho}\frac{\partial}{\partial r} B(r, z)^2 \mathbf{e}_r. \tag{5.4}$$

(5.1), (5.2) and (5.4) are the full governing equations describing the rotational fluid flow under the influence of an externally applied magnetic field. The terms of greatest importance, and those of most interest in our analysis, are the rotational and magnetic terms. The effect of these terms will be reviewed as well as the criteria needed to induce or stabilise perturbations. Additionally, the governing equations of motion are applied to each fluid layer, such that the subscript $j = 1, 2$ will be introduced to designate the inner and outer fluid layers, respectively. A schematic of the problem is shown in figure 5.1. For convenience, the full governing model is written as

$$\frac{\mathrm{D}\rho_j}{\mathrm{D}t} + \rho_j \boldsymbol{\nabla} \cdot \mathbf{u}_j = 0, \tag{5.5}$$

$$\frac{\mathrm{D}\mathbf{u}_j}{\mathrm{D}t} = -\frac{1}{\rho_j}\boldsymbol{\nabla} p_j - \boldsymbol{\Omega} \wedge (\boldsymbol{\Omega} \wedge \mathbf{r}) - 2\boldsymbol{\Omega} \wedge \mathbf{u}_j + \frac{\eta_j}{\rho_j}\nabla^2 \mathbf{u}_j + \frac{\chi_j}{2\mu_0 \rho_j}\frac{\partial}{\partial r} B(r, z)^2 \mathbf{e}_r, \tag{5.6}$$

$$\boldsymbol{\nabla} \cdot \mathbf{u}_j = 0. \tag{5.7}$$

5.1.1 Dimensionless formulation with uniform angular velocity

We now reformulate the model into its dimensionless counterpart. In the present analysis, we take a constant axisymmetric rotation of a circular cell. This implies the angular velocity is a constant, unidirectional vector. The angu-

lar velocity is assumed, without loss of generality, to act along the vertical axis in three-dimensional space such that

$$\mathbf{\Omega} = \Omega \mathbf{e}_z,$$

where the unit vectors $\mathbf{e}_r, \mathbf{e}_\theta, \mathbf{e}_z$ form an orthonormal basis in three dimensions for a cylindrical coordinate system. The dimensional scales for time, length and velocity, denoted by $[T]$, $[L]$ and $[U]$ respectively, can be readily determined by the properties of the system under consideration where

$$t = [T]t', \quad \mathbf{r} = [L]\mathbf{r}', \quad \mathbf{u} = [U]\mathbf{u}', \tag{5.8}$$

such that t', $\mathbf{r}'$, $\mathbf{u}'$ indicate new dimensionless variables and are assumed to be $\mathcal{O}(1)$, where we have used the 'dash' notation to label dimensionless quantities. For the time scale, as angular velocity is assumed constant, the natural scale to choose is

$$[T] = \frac{1}{\Omega}, \quad \text{such that,} \quad t = \frac{1}{\Omega}t', \tag{5.9}$$

where $\Omega = |\mathbf{\Omega}|$ is the magnitude of the constant angular velocity, measured in radians per second.

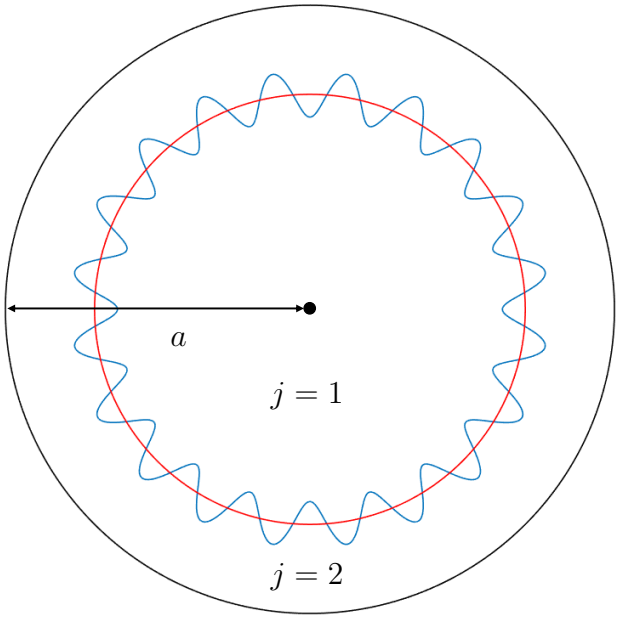

Figure 5.1: The domain of the cell. The outer boundary, with radius a, is a solid wall, the blue sinusoid represents an unstable interface with wavenumber $m = 20$ and the red circle shows the initial radius of the interface at $r = r_0$. The inner fluid region is marked by $j = 1$, while the outer fluid region is marked by $j = 2$.

An appropriate length scale comes from the fluid being constrained within a walled domain, as shown in figure 5.1, so a natural length scale is the domain radius, defined to be a where

$$[L] = a, \quad \text{such that,} \quad \mathbf{r} = a\mathbf{r}'.$$

The velocity scale can be determined by the combination of both time and length by $[U] = [L]/[T]$. Therefore, the velocity scale is

$$[U] = a\Omega, \quad \text{such that,} \quad \mathbf{u} = a\Omega\mathbf{u}'.$$

Once the dimensional scales are determined, they are substituted into (5.4) along with the undetermined scales,

$$\frac{[U]}{[T]}\frac{\mathrm{D}\mathbf{u}_j'}{\mathrm{D}t'} = -\frac{[P]}{[L]\rho_0}\frac{1}{\rho_j'}\boldsymbol{\nabla}'p_j' - [L]\Omega^2\mathbf{e}_z \wedge (\mathbf{e}_z \wedge \mathbf{r}') - 2[U]\Omega\mathbf{e}_z \wedge \mathbf{u}_j' + \frac{[U]\eta_0}{[L]^2\rho_0}\frac{\eta_j'}{\rho_j'}\nabla'^2\mathbf{u}_j' + \frac{\chi_j B_0^2}{2\mu_0\rho_0[L]}\frac{1}{\rho_j'}\frac{\partial}{\partial r'}B(r',z')^2\mathbf{e}_r,$$

where the quantities $[P], B_0, \rho_0, \eta_0$ are given by

$$p = [P]p', \quad B(r,z) = B_0 B(r',z'), \quad \rho_j = \rho_0\rho_j', \quad \eta_j = \eta_0\eta_j'. \tag{5.10}$$

As stated previously, there are two fluids of interest in this system with non-equal densities and viscosity. Rather than choose one fluid property as a global scale, we introduce a characteristic density and viscosity which give the average between both fluid layers. Let the following be defined such that

$$\rho_0 = \frac{\rho_1 + \rho_2}{2}, \quad \eta_0 = \frac{\eta_1 + \eta_2}{2},$$

are the characteristic density and viscosity scales, respectively. We proceed by first scaling the pressure term with the inertial term, giving the inertial pressure scale of the system as

$$[P] = \frac{\rho_0[L]^2}{[T]^2} = \rho_0\Omega^2 a^2,$$

such that the momentum equation becomes

$$a\Omega^2\frac{\mathrm{D}\mathbf{u}_j'}{\mathrm{D}t'} = -a\Omega^2\frac{1}{\rho_j'}\boldsymbol{\nabla}'p_j' - a\Omega^2\mathbf{e}_z \wedge (\mathbf{e}_z \wedge \mathbf{r}') - 2a\Omega^2\mathbf{e}_z \wedge \mathbf{u}_j' + \frac{\Omega\eta_0}{a\rho_0}\frac{\eta_j'}{\rho_j'}\nabla'^2\mathbf{u}_j' + \frac{\chi_j B_0^2}{2\mu_0\rho_0 a}\frac{1}{\rho_j'}\frac{\partial}{\partial r'}B(r',z')^2\mathbf{e}_r. \tag{5.11}$$

Upon simplifying, we have

$$\frac{\mathrm{D}\mathbf{u}'_j}{\mathrm{D}t'} = -\frac{1}{\rho'_j}\boldsymbol{\nabla}' p'_j + r'\mathbf{e}_r - 2\mathbf{e}_z \wedge \mathbf{u}'_j + \frac{1}{\mathrm{Re}}\frac{\eta'_j}{\rho'_j}\boldsymbol{\nabla}'^2\mathbf{u}'_j + \frac{\chi_j B_0^2}{2\mu_0\rho_0\Omega^2 a^2}\frac{1}{\rho'_j}\frac{\partial}{\partial r'}B(r',z')^2\mathbf{e}_r, \tag{5.12}$$

where we introduce the system Reynolds number as

$$\mathrm{Re} = \frac{\rho_0 a^2 \Omega}{\eta_0}.$$

As we are working on a problem in two-dimensions under the influence of a three dimensional magnetic field, we take a slice through the vertical plane at the equilibrium position described in chapter 2. We will therefore proceed to evaluate the magnetic field strength $B(r,z)$, as well as the radial gradient field $\frac{\partial}{\partial r}B(r,z)^2$ on the plane $z = z_0$.

A new dimensionless number is now introduced, relating the relative importance of magnetic pressure acting on a fluid layer with magnetic susceptibility χ_j to inertial pressure, and is defined as

$$\mathrm{Mp}_j = \frac{\chi_j B_0^2}{2\mu_0\rho_0\Omega^2 a^2}. \tag{5.13}$$

Finally, a modified pressure, $\mathrm{P}_{\mathrm{M}j}(r,t)$, is introduced which includes the centrifugal and magnetic force as they are both conserved vector quantities, giving

$$\mathrm{P}_{\mathrm{M}j}(\mathbf{r}',t') = p_j(\mathbf{r}',t') - \frac{\rho'_j}{2}r'^2 - \mathrm{Mp}_j B(r',z'_0)^2. \tag{5.14}$$

By substituting into the momentum equation, it follows that the conservation of mass and incompressibility condition remain unchanged. The dimensionless

governing equations are then

$$\frac{\mathrm{D}\rho_j}{\mathrm{D}t} + \rho_j \boldsymbol{\nabla} \cdot \mathbf{u}_j = 0, \tag{5.15}$$

$$\frac{\mathrm{D}\mathbf{u}_j}{\mathrm{D}t} = -\frac{1}{\rho_j}\boldsymbol{\nabla}\mathrm{P}_{\mathrm{M}j}(\mathbf{r},t) - 2\mathbf{e}_z \wedge \mathbf{u}_j + \frac{1}{\mathrm{Re}}\frac{\eta_j}{\rho_j}\nabla^2\mathbf{u}_j, \tag{5.16}$$

$$\boldsymbol{\nabla} \cdot \mathbf{u}_j = 0, \tag{5.17}$$

where the prime notation has been dropped on the understanding that quantities will be dimensionless unless otherwise stated.

5.1.2 Linear stability analysis - method of normal wavenumbers

Linearising a perturbation solution to the governing equations is a common method used as a foundation when solving for leading order hydrodynamic instability [15]. It gives a strong insight into the behaviour of instabilities during the early time stages when perturbed from their initial hydrostatic state.

If the fluids are in hydrostatic equilibrium, then it is implied that there is zero fluid velocity, $\mathbf{u}_j(\mathbf{r},t) = \mathbf{0}$, with respect to the frame of reference. In a rotating frame of reference, hydrostatic equilibrium occurs when both fluid layers are in solid body rotation. We first determine the hydrostatic solutions with $\mathbf{u}_j(\mathbf{r},t) = \mathbf{0}$; (5.16) is reduced to

$$\mathbf{0} = -\frac{1}{\rho_j}\boldsymbol{\nabla}\mathrm{P}_{\mathrm{M}j}(\mathbf{r},t),$$

which gives the hydrostatic pressure as

$$p_j^*(\mathbf{r},t) = \frac{\rho_j}{2}r^2 + \mathrm{Mp}_j B(r,z)^2 + A_j(t), \quad \text{with} \quad \mathbf{u}_j^*(\mathbf{r},t) = \mathbf{0}, \tag{5.18}$$

where $A_j(t)$ may differ within each fluid layer and the additional superscript '$*$' denotes a hydrostatic quantity, as in [46].

Suppose we let a perturbation to the hydrostatic interface at $r = r_0$ be described by the function disturbance $\xi(\mathbf{r}, t)$, then the full description of the interface is

$$\mathcal{I} := r - (r_0 + \xi(\mathbf{r}, t)) = 0. \tag{5.19}$$

As the form of early time disturbances are presumed to be a sum of sinusoids, we define the initial perturbation as such, with

$$\xi(r, \theta, t) = \alpha \mathrm{e}^{i(m\theta + \omega t)},$$

where, α is the amplitude of the disturbance, m is an eigenvalue denoting the azimuthal wavenumber and ω denotes the angular frequency, such that $c = \omega/m$ is the phase velocity of a wave with eigenvalue m. Upon nondimensionalising with the length scale, we get

$$\mathcal{I} := r - (1 + \epsilon \mathrm{e}^{i(m\theta + \omega t)}) = 0, \tag{5.20}$$

where ϵ is introduced as a parameter describing a ratio between the initial disturbance amplitude and radius of the fluid domain. It is assumed that ϵ is small with

$$\epsilon = \frac{\text{Amplitude of the perturbation}}{\text{Chosen length scale of the system}} = \frac{\alpha}{a} \ll 1. \tag{5.21}$$

The method of solution will be to write linear perturbations to the hydrostatic solution in terms of normal wavenumbers. The method of normal wavenumbers is a standard method for investigating hydrodynamic stability [15].

With the perturbation parameter ϵ, defined by (5.21), the physical quantities of velocity and pressure are written with increasing order in ϵ

$$\mathbf{u}(\mathbf{r}, t)_j = \mathbf{u}^*(\mathbf{r}, t)_j + \epsilon \mathbf{U}_j(\mathbf{r}, t) + \mathcal{O}(\epsilon^2), \tag{5.22}$$

the validity which becomes questionable for $\epsilon \sim 1$, when the amplitude of the disturbance is comparable to the domain size. The function $\mathbf{U}_j$ is introduced as first order perturbation function for the velocity field. Using the hydrostatic velocity, $\mathbf{u}_j^* = \mathbf{0}$, the fluid velocity can be written in terms of $\mathbf{U}_j$ only, with

$$\mathbf{u}(\mathbf{r},t)_j = \epsilon \mathbf{U}_j(\mathbf{r},t) + \mathcal{O}(\epsilon^2), \tag{5.23}$$

As the flow is assumed to be two-dimensional, we may introduce a streamfunction definition of $\mathbf{U}_j$, in terms of a function $\psi_j = \psi_j(\mathbf{r},t)$, such that ψ_j satisfies $\boldsymbol{\nabla} \wedge \boldsymbol{\nabla}\psi_j = \mathbf{u}_j$ [4], giving

$$\mathbf{U}_j = \left(\frac{1}{r}\frac{\partial \psi_j}{\partial \theta}, -\frac{\partial \psi_j}{\partial r}, 0 \right).$$

Using the method of normal wavenumbers, the solution is assumed to have azimuthal and temporal dependence of the form $\mathrm{e}^{i(m\theta+\omega t)}$, so we write the streamfunction as

$$\psi_j(\mathbf{r},t) = \phi_j(r)\mathrm{e}^{i(m\theta+\omega t)}, \tag{5.24}$$

where m is an eigenvalue denoting the wavenumber, ω is the associated angular frequency of the wave and t is the time dependence. We see that the definition for ψ_j is consistent with the incompressibility condition, reducing the full problem to that of a potential flow with

$$\nabla^2 \psi_j = 0. \tag{5.25}$$

We also expect the perturbed pressure to have a similar form as the velocity field, so we redefine the pressure as

$$p_j = p_j^*(\mathbf{r},t) + \epsilon \mathcal{P}_j(r)\mathrm{e}^{i(m\theta+\omega t)} + \mathcal{O}(\epsilon^2), \tag{5.26}$$

where $\mathcal{P}_j(r)$ is the first order perturbation function for the pressure field. The velocity field, $\mathbf{u}_j(\mathbf{r},t)$, may then be expressed as

$$\mathbf{u}_j(\mathbf{r},t) = \left(\frac{im}{r}\phi_j(r), -\frac{\mathrm{d}}{\mathrm{d}r}\phi_j(r)\right)\mathrm{e}^{i(m\theta+\omega t)}. \tag{5.27}$$

It is possible to get a complex number for ω, which provides two important pieces of information about the disturbance of the interface. Writing $\omega = \omega_R + i\omega_I$, where $\{\omega_R, \omega_I\} \in \mathbb{R}$ represent the real and imaginary parts, respectively, the interface becomes

$$r - (r_0 + \epsilon \mathrm{e}^{i(m\theta+\omega_R t)}\mathrm{e}^{-\omega_I t}) = 0. \tag{5.28}$$

Hence, the rate of precession of a disturbance with wavenumber m is given by ω_R, whereas the stability information of the same disturbance is given by the behaviour of ω_I; $\omega_I < 0$ indicates instability.

By taking terms of order $\mathcal{O}(\epsilon)$, the equation of motion, (5.3), can be linearised and expressed in component form. The radial part gives,

$$\begin{aligned} -\frac{m\omega\phi_j}{r} = &-\frac{1}{\rho_j}\frac{\mathrm{d}\mathcal{P}_j}{\mathrm{d}r} - 2\frac{\mathrm{d}\phi_j}{\mathrm{d}r} \\ &+ \frac{im\eta_j}{\rho_j \mathrm{Re}}\left\{\frac{1}{r}\frac{\mathrm{d}}{\mathrm{d}r}\left(r\frac{\mathrm{d}}{\mathrm{d}r}\left(\frac{\phi_j}{r}\right)\right) - \frac{(1+m^2)\phi_j}{r^3} + \frac{2}{r^2}\frac{\mathrm{d}\phi_j}{\mathrm{d}r}\right\} \end{aligned} \tag{5.29}$$

with the azimuthal equation as,

$$\begin{aligned} -i\omega\frac{\mathrm{d}\phi_j}{\mathrm{d}r} = &-\frac{im\mathcal{P}_j}{\rho_j r} - 2\frac{im\phi_j}{r} \\ &+ \frac{\eta_j}{\rho_j \mathrm{Re}}\left\{-\frac{1}{r}\frac{\mathrm{d}}{\mathrm{d}r}\left(r\frac{\mathrm{d}^2\phi_j}{\mathrm{d}r^2}\right) + \frac{(1+m^2)}{r^2}\frac{\mathrm{d}\phi_j}{\mathrm{d}r} - \frac{2m^2\phi_j}{r^3}\right\}, \end{aligned} \tag{5.30}$$

where $\phi_j = \phi_j(r)$. Both $\mathcal{O}(\epsilon)$ equations are identical to those provided by Scase *et al.* [46]. We differ here as we assume that the fluid properties, ρ and η, are constant in each layer. Rearranging the azimuthal part, (5.30), for $\mathcal{P}_j$ and

substituting into the radial part, (5.29), gives

$$i\omega\left(\phi_j'' + \frac{\phi_j'}{r} - \frac{m^2\phi_j}{r^2}\right) = \frac{1}{\mathrm{Re}}\frac{\eta_j}{\rho_j}\left\{\phi_j'''' + \frac{2\phi_j'''}{r} - (1+2m^2)\left(\frac{\phi_j''}{r^2} - \frac{\phi_j'}{r^3}\right) + \frac{m^2(m^2-4)\phi_j}{r^4}\right\}. \quad (5.31)$$

Equation (5.31) is of an Orr-Sommerfeld type which describes perturbations to a two-dimensional flow that can be used to determine the hydrostatic stability of an interface [15]. The prime notation here is used to denote the derivative with respect to the argument, r.

5.1.3 Boundary conditions

We apply the standard dynamic and kinematic boundary conditions along with velocity regularity which is a special condition, based on physical grounds, that applies to this problem as a result of its geometry. The no-penetration condition is applied on the boundary at $r = 1$.

Velocity regularity is a condition that requires the fluid velocity to be finite at the origin $r = 0$. In addition to the solid boundary no-penetration condition, we have

$$|\mathbf{u}_1(r=0)| < \infty, \quad \text{and} \quad \mathbf{u}_2(r=1)\cdot\mathbf{e}_r = 0. \quad (5.32)$$

There also exists a no-slip condition at the solid boundary in the case of a viscous outer layer, $\eta_2 \neq 0$, which tells us that the tangential velocity on the boundary is equal to the velocity of the boundary. This means that

$$\mathbf{u}_2(r=1)\cdot\mathbf{e}_\theta = 0. \quad (5.33)$$

However, in this chapter, we are restrict ourselves to the inviscid case so that the no-slip condition is not needed, but will be used at a later stage. The kinematic boundary condition requires that fluid parcels on the interface remain on the

interface and so move with the velocity of the interface. This can be expressed as the material derivative of the interfacial equation being zero. That is,

$$\frac{\mathrm{D}\mathcal{I}}{\mathrm{D}t} = \frac{\partial \mathcal{I}}{\partial t} + (\mathbf{u}\cdot\nabla)\mathcal{I} = 0. \tag{5.34}$$

By using the perturbed velocity definition, as in (5.23), the kinematic boundary condition, (5.34), becomes

$$-i\epsilon\omega \mathrm{e}^{i(m\theta+\omega t)} + \frac{i\epsilon m\phi_j}{r}\mathrm{e}^{i(m\theta+\omega t)} - \frac{i\epsilon^2 m}{r}\mathrm{e}^{i(m\theta+\omega t)}\phi_j' = 0. \tag{5.35}$$

Hence, at the initial interface, $r = r_0$, the leading order kinematic boundary condition becomes

$$\phi_j(r_0) = \frac{\omega r_0}{m}, \qquad \text{for } j = 1, 2. \tag{5.36}$$

The dynamic boundary condition is given in terms of the stress continuity condition across the interface which is explained in detail within the next section.

5.1.4 Stress continuity condition

The stress condition is derived across the interface $\mathcal{I}$. The continuity of stress is given by, in dimensionless form,

$$\left[\underline{\underline{\sigma}}\cdot\hat{\mathbf{n}}\right]_-^+ = \frac{1}{\mathrm{We}}(\nabla\cdot\hat{\mathbf{n}})\hat{\mathbf{n}}, \tag{5.37}$$

where the plus-minus, on the left hand side, indicates a jump from the outer fluid to the inner fluid. The Weber number, We, relates the importance of inertial forces to surface stress, defined as $\mathrm{We} = \rho_0\Omega^2 a^3/\gamma$ where γ is the surface tension between the fluid layer, and with $\underline{\underline{\sigma}}$ denoting the stress tensor given by

$$\underline{\underline{\sigma}}_j = -p_j\underline{\underline{\mathrm{I}}} + \frac{2\eta_j}{\mathrm{Re}}\underline{\underline{\mathrm{e}}}_j$$

so that,

$$\left[\underline{\underline{\sigma}} \cdot \hat{\mathbf{n}}\right]_{-}^{+} = \left[-p_j \hat{\mathbf{n}}\right]_{-}^{+} + \frac{2}{\mathrm{Re}} \left[\eta_j \underline{\underline{\mathrm{e}}}_j \cdot \hat{\mathbf{n}}\right]_{-}^{+}, \tag{5.38}$$

where $\underline{\underline{\mathrm{I}}}$ is the identity second rank tensor and $\underline{\underline{\mathrm{e}}}_j$ is the rate of strain tensor defined as

$$\underline{\underline{\mathrm{e}}}_j = \frac{1}{2}\left(\boldsymbol{\nabla}\mathbf{u}_j + (\boldsymbol{\nabla}\mathbf{u}_j)^{\mathrm{T}}\right). \tag{5.39}$$

The unit normal to the interface is defined by

$$\begin{aligned}\hat{\mathbf{n}} = \frac{\nabla\mathcal{I}}{|\nabla\mathcal{I}|} &= \frac{\hat{\mathbf{r}} + \left(-\frac{im}{r}\epsilon \mathrm{e}^{i(m\theta+\omega t)}\right)\hat{\theta}}{1 + \epsilon^2 \frac{m^2}{r}\mathrm{e}^{2i(m\theta+\omega t)}} \\ &= (1+\mathcal{O}(\epsilon^2))\hat{\mathbf{r}} + \left(-\frac{im}{r}\epsilon \mathrm{e}^{i(m\theta+\omega t)} + \mathcal{O}(\epsilon^2)\right)\hat{\theta}.\end{aligned} \tag{5.40}$$

Then, on the interface $r = r_0 + \epsilon \mathrm{e}^{i(m\theta+\omega t)}$, the unit normal becomes

$$\hat{\mathbf{n}} = (1+\mathcal{O}(\epsilon^2))\hat{\mathbf{r}} + \left(-\frac{im}{r_0}\epsilon \mathrm{e}^{i(m\theta+\omega t)} + \mathcal{O}(\epsilon^2)\right)\hat{\theta}. \tag{5.41}$$

where Taylor's expansion has been used to obtain a linear approximation in ϵ. The right hand side of (5.37) is calculated using (5.41) and is given by

$$\nabla \cdot \hat{\mathbf{n}} = \frac{1}{r_0} + \epsilon \frac{(m^2-1)}{r_0^2}\mathrm{e}^{i(m\theta+\omega t)} + \mathcal{O}(\epsilon^2).$$

We now consider the first term on the right hand side of (5.38). Since the perturbation is applied to the initial radius of the interface, we find the Taylor expansion of the pressure about $r = r_0$ to get

$$\left[-p_j \hat{\mathbf{n}}\right]_{-}^{+} = -\left[p^*(r_0) + \epsilon\left(\left.\frac{\mathrm{d}p^*}{\mathrm{d}r}\right|_{r=r_0} + \mathcal{P}(r_0)\right) + \mathcal{O}(\epsilon^2)\right]_{-}^{+} \tag{5.42}$$

$$[-p\hat{\mathbf{n}}]_-^+ = -\left\{\left[p^*(r_0) + \epsilon\left(\left.\frac{\mathrm{d}p^*}{\mathrm{d}r}\right|_{r=r_0} + \mathcal{P}(r_0)\right)\right]_-^+ + \mathcal{O}(\epsilon^2)\right\}\hat{\mathbf{r}} + \left\{\frac{im\epsilon}{r_0}\mathrm{e}^{i(m\theta+\omega t)}\left[p^*(r_0)\right]_-^+ + \mathcal{O}(\epsilon^2)\right\}\hat{\theta} \quad (5.43)$$

where $p^*(r,t)$ is as defined in (5.18). The second term on the right hand side of (5.38) uses the rate of strain tensor, as in (5.39), giving

$$\left[\eta\underline{\underline{e}}\cdot\hat{\mathbf{n}}\right]_-^+ = \left\{\frac{im\epsilon}{r_0^2}\left[\eta^*(r_0\phi'' - \phi)\right]_-^+\mathrm{e}^{i(m\theta+\omega t)} + \mathcal{O}(\epsilon^2)\right\}\hat{\mathbf{r}} + \left\{\frac{\epsilon}{2r_0}\left[\eta^*(-r_0^2\phi'' + r_0\phi' - m^2\phi)\right]_-^+\mathrm{e}^{i(m\theta+\omega t)} + \mathcal{O}(\epsilon^2)\right\}\hat{\theta}$$

Then the stress continuity condition, (5.37), finally becomes,

$$-\left[\left\{p^*(r_0) + \epsilon\left(\rho r_0 + 2\mathrm{Mp}B(r_0)\left.\frac{\partial B}{\partial r}\right|_{\substack{r=0\\z=z_0}} + \mathcal{P}(r_0)\right) + \frac{2\epsilon im}{r_0^2\mathrm{Re}}\eta(r_0\phi' - \phi)\mathrm{e}^{i(m\theta+\omega t)} + \mathcal{O}(\epsilon^2)\right\}\hat{\mathbf{r}} + \left\{\frac{im\epsilon}{r_0}\mathrm{e}^{i(m\theta+\omega t)}p^*(r_0) + \frac{\epsilon}{r_0^2\mathrm{Re}}\eta(-r_0^2\phi' + r_0\phi' - m^2\phi)\mathrm{e}^{i(m\theta+\omega t)} + \mathcal{O}(\epsilon^2)\right\}\hat{\boldsymbol{\theta}}\right]_-^+ = \frac{1}{\mathrm{We}}\left\{\left(\frac{1}{r_0} + \epsilon\frac{(m^2-1)}{r_0^2}\mathrm{e}^{i(m\theta+\omega t)}\right) + \mathcal{O}(\epsilon^2)\right\}\hat{\mathbf{r}} + \left\{-\frac{im}{r_0^2}\epsilon\mathrm{e}^{i(m\theta+\omega t)} + \mathcal{O}(\epsilon^2)\right\}\hat{\boldsymbol{\theta}}. \quad (5.44)$$

To maintain simplicity, we proceed to write $B(r) = B(r, z_0)$ as we will only be interested in the magnetic field contributions at $z = z_0$, discussed in chapter 2. We can isolate terms by taking $\mathcal{O}(1)$ and $\mathcal{O}(\epsilon)$ in the radial direction and $\mathcal{O}(\epsilon)$ in the azimuthal direction, respectively

$$[p^*]_-^+ = -\frac{1}{\mathrm{We}}\frac{1}{r_0} \quad (5.45)$$

$$\left[\rho r_0 + 2\mathrm{Mp}B(r_0)\left.\frac{\partial B}{\partial r}\right|_{\substack{r=0\\z=z_0}} + \mathcal{P}(r_0) - \frac{2im\eta}{r_0^2\mathrm{Re}}(r_0\phi' - \phi)\right]_-^+ = -\frac{1}{\mathrm{We}}\frac{m^2-1}{r_0^2} \quad (5.46)$$

$$\left[\eta(-r_0^2\phi'' + r_0\phi' - m^2\phi)\right]_-^+ = 0 \quad (5.47)$$

We first consider stability criteria for an inviscid fluid; when fluid inertia dominates fluid shear stress forces such that $\mathrm{Re} \to \infty$ with $|\eta_j| \to 0$.

5.2 Two-dimensional inviscid flow with surface tension

We now consider a two-dimensional inviscid model to investigate radial fluid instabilities under rotation, and the effect on stability of an externally applied magnetic field. Immediately, from the assumption of an inviscid model, we can see that the stress continuity equations, (5.45)-(5.47), can be reduced to

$$[p^*]_-^+ = -\frac{1}{\mathrm{We}}\frac{1}{r_0} \tag{5.48}$$

$$\left[\rho r_0 + 2\mathrm{Mp}B(r_0)\left.\frac{\partial B}{\partial r}\right|_{\substack{r=0\\z=z_0}} + \mathcal{P}(r_0)\right]_-^+ = -\frac{1}{\mathrm{We}}\frac{m^2-1}{r_0^2}, \tag{5.49}$$

where the azimuthal $\mathcal{O}(\epsilon)$ stress continuity condition, (5.47), is automatically satisfied due to the absence of dynamic viscosity. The perturbed quantity $\mathcal{P}_j(r)$ can be determined by rearranging (5.30) and taking the inviscid approximation, giving

$$\mathcal{P}_j(r) = -\rho_j\left(2\phi_j - \frac{\omega r}{m}\phi_j'\right). \tag{5.50}$$

Additionally, the Orr-Sommerfeld equation for stability, (5.31), can be simplified to the second order Rayleigh differential equation

$$\phi_j + \frac{\phi_j'}{r} - \frac{m^2\phi_j''}{r^2} = 0, \tag{5.51}$$

whose solutions are found with Frobenius' series method to give power law solutions as

$$\phi_1(r) = \frac{\omega r_0}{m}\left(\frac{r}{r_0}\right)^m, \quad \phi_2(r) = \frac{\omega r_0}{m}\left(\frac{r}{r_0}\right)^m\left(\frac{1-r^{-2m}}{1-r_0^{-2m}}\right). \tag{5.52}$$

We now have all the tools necessary to provide us with the dispersion relation; a relation between the wave frequency with its wavenumber or wavelength, λ, such that $\lambda = 2\pi/m$.

5.2.1 Inviscid dispersion relation

Immediately we can substitute the eigenfunctions from (5.52) into the azimuthal stress continuity equation, (5.49), evaluating at $r = r_0$ to give

$$\rho_2 r_0 + 2\mathrm{Mp}_2 B(r_0)\left.\frac{\partial B}{\partial r}\right|_{\substack{r=0\\z=z_0}} - \rho_2\left\{2\frac{\omega r_0}{m} - \frac{\omega r_0}{m}\left(\omega + \frac{2r_0^{-2m}\omega}{1-r_0^{-2m}}\right)\right\} - \rho_1 r_0 - 2\mathrm{Mp}_1 B(r_0)\left.\frac{\partial B}{\partial r}\right|_{\substack{r=0\\z=z_0}} + \rho_1\left\{2\frac{\omega r_0}{m} - \frac{\omega r_0}{m}\omega\right\} = -\frac{1}{\mathrm{We}}\frac{m^2-1}{r_0^2}. \quad (5.53)$$

By introducing the dimensionless Atwood number as

$$\mathcal{A} = \frac{\rho_2 - \rho_1}{\rho_1 + \rho_2},$$

and noting that the dimensionless sum of the density in both fluid layers is equal to 2, we may multiply (5.53) by $m/(r_0(\rho_1+\rho_2))$, to make further simplifications giving

$$\mathcal{A}(\omega^2 - 2\omega + m) = \frac{(1+\mathcal{A})\omega^2}{1-r_0^{2m}} - \frac{m(\chi_2-\chi_1)B_0^2}{r_0(\rho_1+\rho_2)\mu_0\rho_0\Omega^2 a^2}B(r_0)\left.\frac{\partial B}{\partial r}\right|_{\substack{r=0\\z=z_0}} - \frac{m(m^2-1)}{\mathrm{We}(\rho_1+\rho_2)r_0^3}, \quad (5.54)$$

The Atwood number gives an indication of the initial set-up of the system under consideration. By our definitions, if $\mathcal{A} < 0$ then the inner fluid layer is more dense than the outer ($\rho_2 < \rho_1$). We will see that, in the absence of surface tension and magnetic forces, a negative Atwood number will indicate an initially unstable configuration. In this case, we will say that the system is naturally unstable under rotation.

We now write a quadratic equation for ω which gives the inviscid dispersion relation as

$$\omega^2 + \mathcal{A}^*(2\omega - m) = \mathcal{A}^*\left(\mathcal{S} - \mathcal{B}\right), \tag{5.55}$$

where $\mathcal{A}^*$ is introduced as a modified Atwood number, as defined in [46] and given as

$$\mathcal{A}^* = \mathcal{A}\left(\frac{1 - r_0^{2m}}{1 + \mathcal{A}r_0^{2m}}\right).$$

We have also introduced two functions of importance. The surface tension adjustment factor, $\mathcal{S}$, which accounts for surface tension effects, and the magnetic force factor, $\mathcal{B}$, parameterising effects derived from the externally applied magnetic field. The factors are expressed as

$$\mathcal{S}(\mathrm{We}; \mathcal{A}, m, r_0) = \frac{m(m^2 - 1)}{2r_0^3 \mathrm{We}\mathcal{A}}, \tag{5.56}$$

$$\mathcal{B}(B(r_0), m, r_0, \chi_j) = \frac{m(\chi_1 - \chi_2)B_0^2}{2r_0\mu_0\rho_0\Omega^2 a^2 \mathcal{A}} B(r_0) \left.\frac{\partial B}{\partial r}\right|_{\substack{r=0 \\ z=z_0}}. \tag{5.57}$$

The behaviour of the interfacial perturbation is given by the two solutions of (5.55), giving

$$\omega(m) = -\mathcal{A}^* \pm \left[\mathcal{A}^*(\mathcal{A}^* + m + \mathcal{S} - \mathcal{B})\right]^{\frac{1}{2}}, \tag{5.58}$$

which differs from the solution (3.11) by Scase & Hill in [46] by the inclusion of the magnetic term $\mathcal{B}(B(r_0), m, r_0, \chi_j)$.

If $\omega(m)$ is real and nonzero, then the interface is stable and will precess about the axis of rotation, giving travelling waves solutions. The discriminant of $\omega(m)$ will provide two travelling waves that will travel both clockwise and anticlockwise. If $\omega_I \neq 0$ then the positive, ω_I^+, and negative, ω_I^-, solutions contribute to the instability. However, ω_I^+ can be seen to decay over time, whereas ω_I^- is seen to grow in time when substituted into (5.20). Hence, the negative solution is the solution of interest in the following discussions.

5.2.2 Density stratification, magnetic influence and surface tension effects

From the dispersion relation in equation (5.58) and our discussion, we can determine the critical wavenumber, m_c, for which all wavenumbers with $m < m_c$ are unstable. The critical wavenumber is found by setting the discriminant of (5.58) to be zero. Let us define a function $\mathcal{D}(m)$ such that

$$\mathcal{D} := \mathcal{A}^* \left(\mathcal{A}^* + m + \mathcal{S} - \mathcal{B} \right). \tag{5.59}$$

Using the definitions of $\mathcal{A}^*$, $\mathcal{S}$ and $\mathcal{B}$, the critical wavenumber is found by the implicit relationship $\mathcal{D}(m_c) = 0$ with

$$\mathcal{A}\left(\frac{1 - r_0^{2m_c}}{1 + \mathcal{A} r_0^{2m_c}}\right) + m_c + \frac{m_c(m_c^2 - 1)}{2 r_0^3 \mathrm{We} \mathcal{A}} - \frac{m_c(\chi_1 - \chi_2) B_0^2}{2 r_0 \mu_0 \rho_0 \Omega^2 a^2 \mathcal{A}} B(r_0) \left.\frac{\partial B}{\partial r}\right|_{\substack{r=0 \\ z=z_0}} = 0. \tag{5.60}$$

We have assumed that the fluid-fluid system has a non-equal density stratification across both layers such that $\mathcal{A} \neq 0$. With the combination of fluids used for experiments in Chapter 3, we know that the difference in magnetic susceptibility is negative such that $\chi_1 - \chi_2 < 0$. Additionally, the gradient product in the radial direction at the initial interface is positive with a dimensional value of 74.7 $\mathrm{T^2 m^{-1}}$, so that the magnetic term provides an additional restorative force to the interface, further suppressing the growth of wavenumber m. This value is from equation (3.3) and is dependent upon fluid properties, such as density.

For each wavenumber, instability occurs if $\mathcal{D}(m) < 0$, while $\mathcal{D}(m) > 0$ implies stability. Figure 5.2 shows the suppressing nature of the magnetic field contributions in addition to surface tension effects in varying combinations, with $\mathrm{We} \approx 1.7 \times 10^2$ and $\mathcal{A} = -0.079$, with respect to the measured values for ρ_1, ρ_2, and γ in chapter 3. For the case where both magnetism and surface tension play a role, we see that the critical wavenumber is $m_c = 9$. On the other hand, for the case of zero magnetic field contribution, the critical wavenumber is $m_c = 10$.

Hence, the inclusion of the magnetic field can stabilise higher order wavenumbers under suitable conditions.

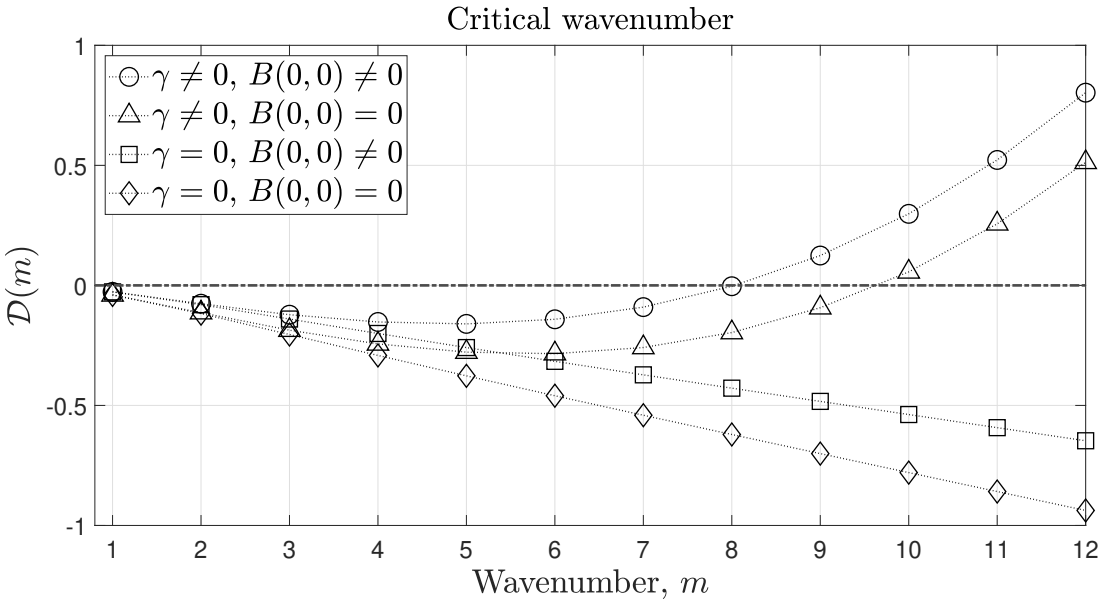

Figure 5.2: Effect of the magnetic factor $\mathcal{B}$ and surface tension factor $\mathcal{S}$ on $\mathcal{D}$, for $\gamma = 0.0028$ N m^{-1}, $B(0,0) = 9.2$ T, $\Omega = 25$ rad s^{-1} and $\mathcal{A} = -0.079$

There is a special case at $m = 1$ when $B(0,0) \neq 0$. For the parameters used in figure 5.2, we see that $m = 1$ is unstable in all cases. The stability of $m = 1$ is independent of surface tension contributions as we have $\mathcal{S} = 0$, so we return to the criteria in (5.59) to find a range on the Atwood number for which instability of $m = 1$ occurs. Solving (5.59) for $\mathcal{A}$, we get two solutions as

$$\mathcal{A} = \frac{\left\{-m + \mathcal{B}_2 \pm [(m - \mathcal{B}_2) - 4(1 - r_0^{2m} + m r_0^{2m})]^{\frac{1}{2}}\right\}}{2(1 - r_0^{2m} + m r_0^{2m})} \tag{5.61}$$

where we have defined

$$\mathcal{B}_2 := \frac{m r_0^{2m-1}(\chi_1 - \chi_2)}{4} \left.\frac{\partial B^2}{\partial r}\right|_{\substack{r=0 \\ z=z_0}}, \tag{5.62}$$

for simplicity. Looking at the behaviour of $m = 1$ for $\mathcal{A} \in [-1, 0)$ in figure 5.3 shows that $m = 1$ is unstable for all configurations with $\mathcal{A} < 0$ and $\mathcal{B}_2 = 0$. When $\mathcal{B}_2 \neq 0$, there is a region for which instability occurs. These points are marked by

black dots on figure 5.3 and can vary with differing angular velocity, and strength of the magnetic field at $B(0,0)$. The magnetic force is acting to restore the centre of mass of the inner fluid layer to its equilibrium position, described in chapter 2. The Atwood region of instability in figure 5.3 is $-0.99 < \mathcal{A} < -0.025$. Outside of this range, the magnetic body forces are able to overcome centrifugal motion for $m = 1$. When $\mathcal{A} > -0.025$, the density stratification for rotation is too small, weakening the centrifugal force compared to the density-independent constant magnetic force, stabilising the centre of mass of the inner fluid region.

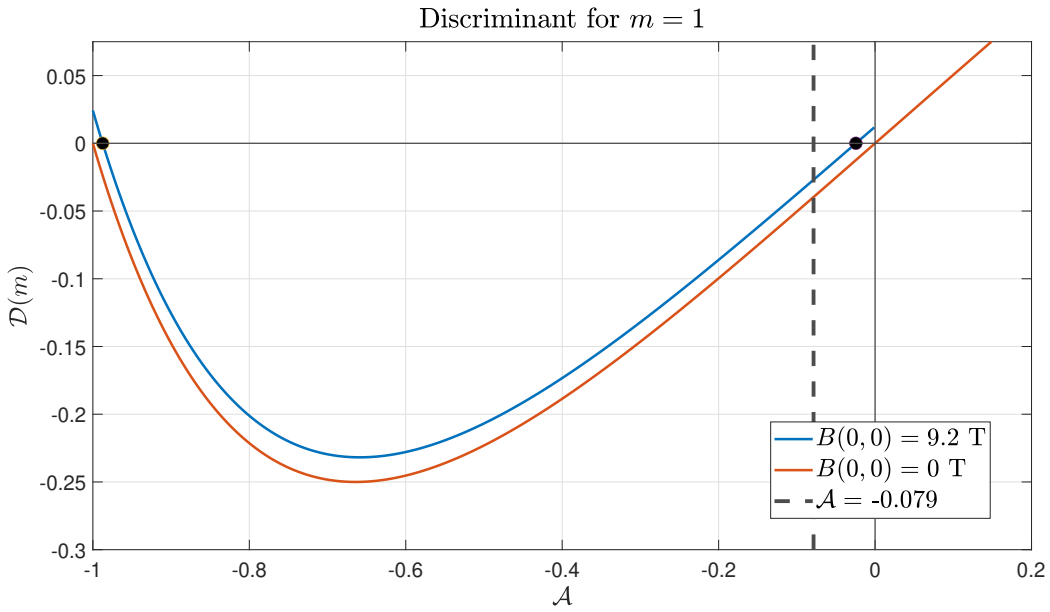

Figure 5.3: Stability of $m = 1$ in the presence of a magnetic field with We $\approx 1.7 \times 10^2$ and $\Omega = 25$ rad s^{-1}. The dark dots indicate the lower and upper bounds on $\mathcal{A}$. When $\mathcal{D} > 0$, $m = 1$ grows in time. When $\mathcal{D} < 0$, $m = 1$ is stabilised.

The existence of a stability region is unique to $m = 1$ due to the lack of contribution from surface tension. For $m > 1$, a critical Atwood number is observed, as shown in figure 5.4, which differ for each wavenumber. Additionally, we can decide upon a m_c, thus finding the necessary density stratification needed to achieve stability above the chosen m_c, while keeping all other parameters constant, with $\Omega = 25$ rad s^{-1}. Shown in table 5.1 are values for the critical density stratification for the associated critical wavenumber with $B(0,0) = 0$ T and We $\approx 1.7 \times 10^2$. Comparison with figure 5.2 shows, for $\mathcal{A} = -0.079$, the

critical wavenumber as $m = 6$.

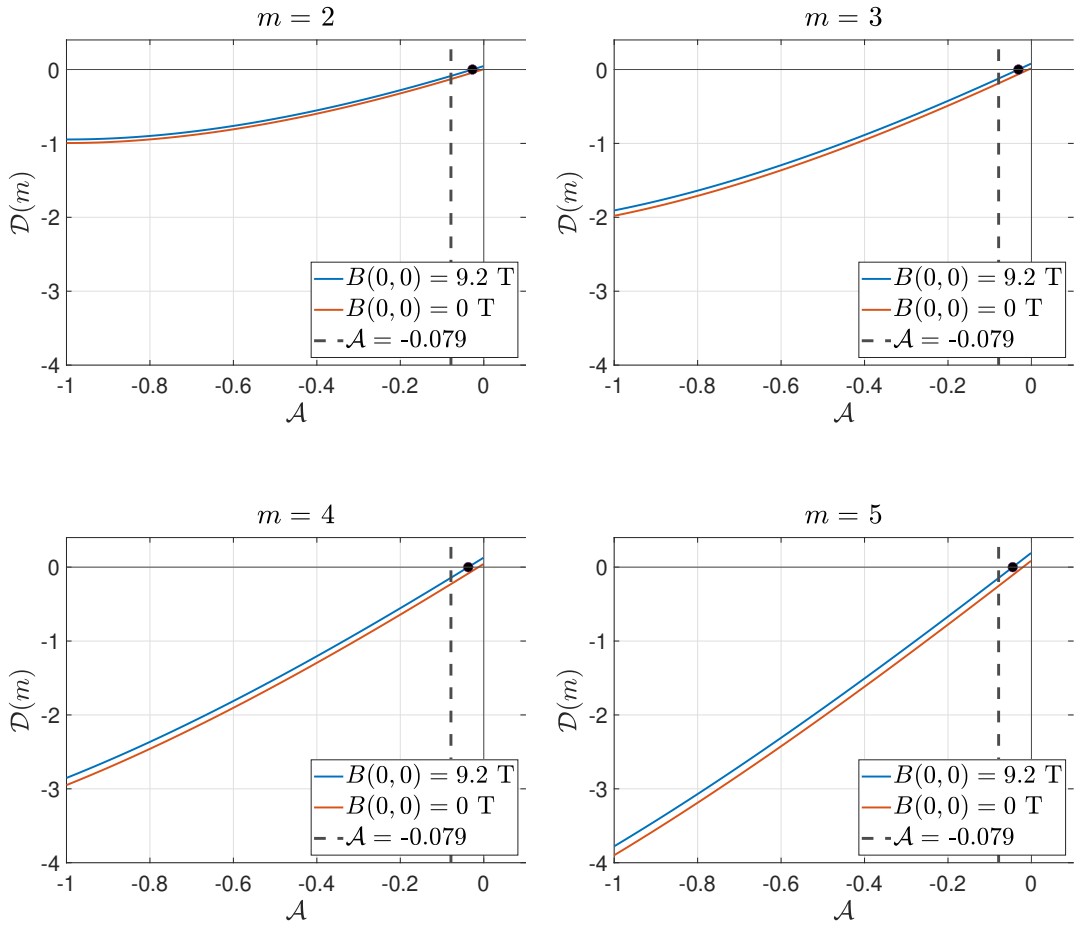

Figure 5.4: Stability of $m = 2, 3, 4, 5$ in the presence of a magnetic field with We $\approx 1.7 \times 10^2$ and $\Omega = 25$ rad s^{-1}. The dark dot indicates the critical Atwood number.

The effects of the magnetic field can be seen at higher order wavenumbers in figure 5.4. The magnetic field effect is linearly proportional to m, reducing the critical Atwood number needed for stability as m increases.

5.2.3 Critical angular velocity

To find the critical angular velocity, we first transform (5.58) into dimensional variables. Reversing the process set out in section 5.1.1, using the dimensional scale defined, the Weber number definition and noting that ω denotes angular

m_c	Critical Atwood number
1	$\mathcal{A} \approx -0.99$ or $\mathcal{A} \approx -0.025$
2	$\mathcal{A} \approx -0.027$
3	$\mathcal{A} \approx -0.031$
4	$\mathcal{A} \approx -0.037$
5	$\mathcal{A} \approx -0.045$
6	$\mathcal{A} \approx -0.054$
7	$\mathcal{A} \approx -0.065$
8	$\mathcal{A} \approx -0.078$

Table 5.1: Unstable density stratification which allow for the associated critical wavenumber, m_c. Values are given to two significant figures. Density stratification greater than the critical Atwood number stabilises m_c, while less than the critical Atwood number increases unstable growth rate.

frequency with the time scale as defined in (5.9), we have

$$\omega = \mathcal{A}^*\Omega \pm \left(\mathcal{A}^* \left(\mathcal{A}^*\Omega^2 + m\Omega^2 + \frac{m(m^2-1)\gamma}{2r_0^3\rho_0\mathcal{A}} - \frac{m(\chi_1-\chi_2)}{4r_0\rho_0\mu_0\mathcal{A}} \frac{\partial B^2}{\partial r}\bigg|_{\substack{r=0 \\ z=z_0}} \right) \right)^{\frac{1}{2}}.$$

with the same assumptions set out in section 5.2.2, the discriminant of the angular frequency must satisfy

$$\Omega^2(\mathcal{A}^* + m) + \frac{m(m^2-1)\gamma}{2r_0^3\rho_0\mathcal{A}} - \frac{m(\chi_1-\chi_2)}{4r_0\rho_0\mu_0\mathcal{A}} \frac{\partial B^2}{\partial r}\bigg|_{\substack{r=0 \\ z=z_0}} > 0. \tag{5.63}$$

When the system acts under rotation only, such that $B(0,0) = 0$, $\gamma = 0$, the interface is unstable for all $m \in \mathbb{N}$. The presence of surface tension, $\gamma > 0$, is seen to stabilise the interface for each wavenumber $m > 1$. The contributions from a magnetic field further stabilise each wavenumber with constraints on the Atwood number and magnetic susceptibility as described in section 5.2.2. If the system has $\chi_1 - \chi_2 > 0$, then the magnetic field would contribute to unstable growth.

The critical angular velocity to induce instability in the inviscid scheme, under the influence of an externally applied magnetic field in the presence of surface

tension is given by

$$\Omega_c^2 = \frac{1}{\mathcal{A}(\mathcal{A}^* + m)} \left(\frac{m(\chi_1 - \chi_2)}{2r_0\rho_0\mu_0} \left. \frac{\partial B^2}{\partial r} \right|_{\substack{r=0 \\ z=z_0}} - \frac{m(m^2-1)\gamma}{2r_0^3\rho_0} \right). \tag{5.64}$$

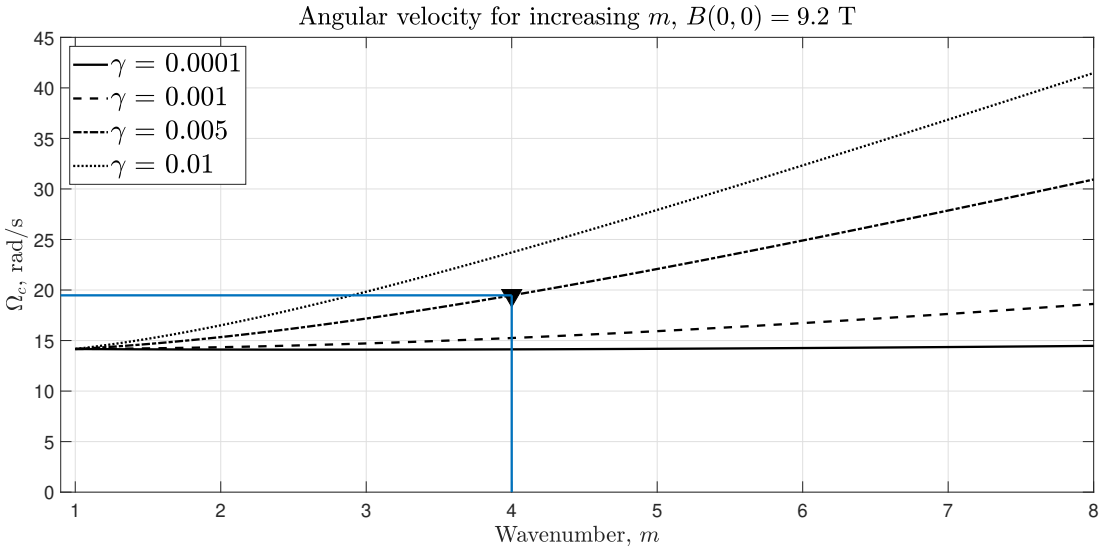

Figure 5.5: Critical angular velocity when under the influence of an externally applied magnetic field, for various surface tension values given by γ. The triangle shows that $\Omega_c = 19.5$ rad s^{-1} and $\gamma = 0.005$ N m^{-1} at $m = 4$.

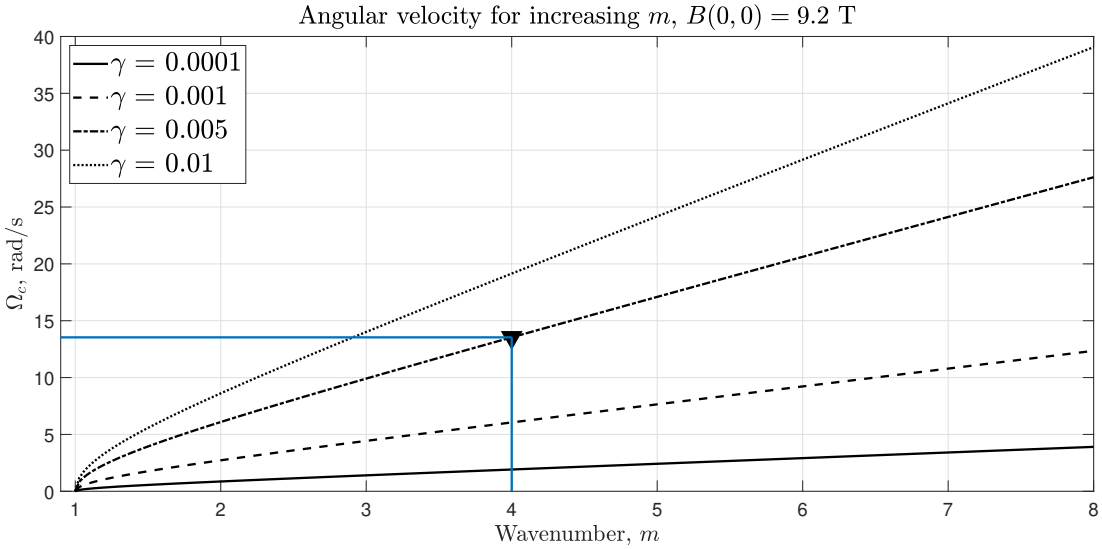

Figure 5.6: Critical angular velocity in the absence of an externally applied magnetic field. The triangle shows that $\Omega_c = 13.5$ rad s^{-1} and $\gamma = 0.005$ N m^{-1} at $m = 4$.

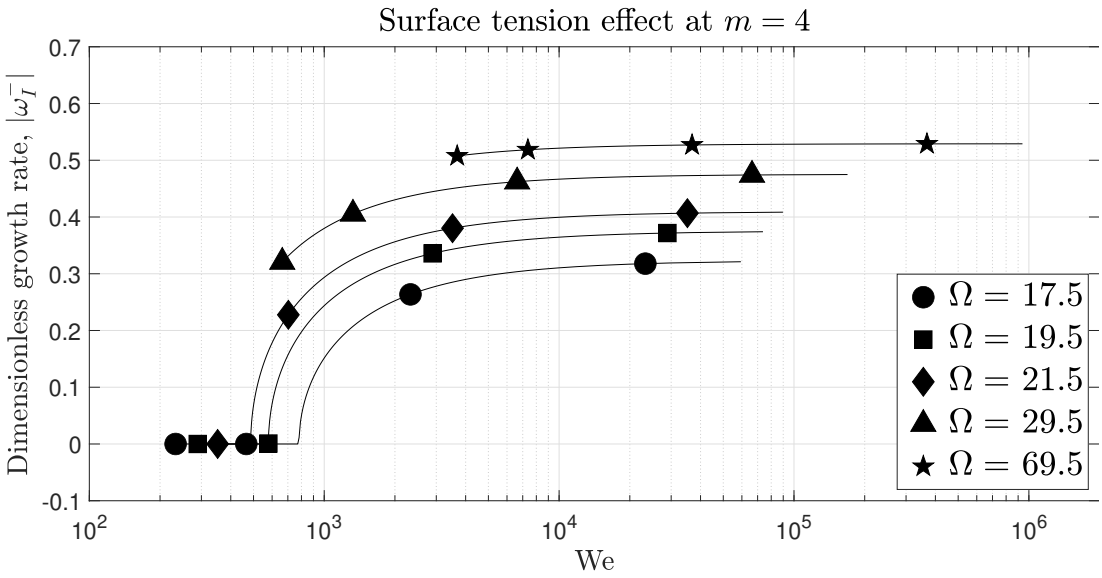

Figure 5.7: Stabilising effect of surface tension for wavenumber $m = 4$. The markers along each curve designate points of surface tension values where $\gamma = 0.01$, 0.005, 0.001 and 0.0001 N m^{-1} respectively.

In our experiments we set the field strength to be $B(0,0) = 9.2$ T giving the radial gradient product as

$$\left.\frac{\partial B^2}{\partial r}\right|_{\substack{r=r_0\\z=z_0}} = 74.7 \text{ T}^2\text{m}^{-1}, \tag{5.65}$$

which is calculated from a model of the solenoid magneti using the Biot-Savart law, [42], and is independent of the properties of the fluid. By using the measured quantities of the fluid properties as described in chapter 3, we can find Ω_c for various values of γ. Hence, we may also determine the critical velocity required to induce unstable growth of any desired wavenumber. Figure 5.5 shows the change in Ω_c for increasing wavenumber over increasing values of surface tension while under the influence of an externally applied magnetic field, using the experimental parameters for ρ_1, ρ_2, χ_1, χ_2, and r_0. By looking at the special case $m = 1$, the surface tension term in (5.63) becomes zero leaving only magnetic forces. The critical angular velocity is thus

$$\Omega_c = 13.4 \text{ rad s}^{-1}. \tag{5.66}$$

Notice that this value is different to the critical angular velocity given by (3.7). This is due to us accounting for surface tension. The suppressing nature of surface tension increases the critical angular velocity necessary instability. For $m \geq 2$ and $\gamma \neq 0$, surface tension starts to take effect on the interface. The surface tension term is proportional to m^2 and becomes a dominating effect as m increases. The angular velocity required to induce instability for wave mode m also increases as a consequence.

In the absence of the magnetic field, (5.63) depends only upon surface tension. In the special case $m = 1$, the effect of surface tension disappears and the critical velocity is $\Omega_c = 0$ rad s^{-1}. Increasing m rapidly increases surface tension effects showing the stabilising effect of surface tension when $\mathcal{A} < 0$. Figure 5.6 shows how Ω_c is affected when $B(0,0) = 0$ T. In figure 5.7 we see more clearly the stabilising nature of surface tension for various values of Ω. The range of surface tension covered is the same as figures 5.5 and 5.6, where the triangle indicates the necessary critical velocity for $m = 4$. When $\Omega \leq 24.3$ rad s^{-1} we see that the points at $\gamma = 0.005$ N m^{-1} and $\gamma = 0.01$ N m^{-1} are along the line $\omega_I^- = 0$ showing that $m = 4$ is stable; consistent with the discussion of figure 5.5. In the limit as We $\to \infty$, the surface tension force becomes negligible. In this limit, the asymptotes give the maximum possible growth rate for any given wavenumber, on the assumption that the fluid properties have not changed.

5.3 Summary

Throughout the preceding discussions, we have derived the inviscid theoretical predictions as given by Scase *et al.* [46], with the inclusion of magnetic field effects. The predictions tell us the contributing nature of the three main effects on a body of fluid: centrifugal motion, surface tension, and the presence of an external magnetic field. By investigating the effects mentioned, we were able to determine stability criteria for each wavenumber m. In particular, we were

able to determine a critical wavenumber for which all wavenumbers below exhibit instability. Other criteria were also determined for the Atwood number and angular velocity. This gives us a variety of properties that may be adjusted to induce or suppress instability.

The inviscid study provides a good background into the two-phase fluid instability problem under the influence of a magnetic field. The inviscid assumption is one that gives a reasonable initial guess to start an investigation into the growing instabilities of the associated experiments. However, this is not an applicable in our experiments due to the large shear stresses present within the flow field. It is therefore instructive to adjust the theoretical model to include such effects and consider new modelling assumptions in light of the geometry used during experiments.

Chapter 6

Hele-Shaw analysis in rotational geometry

With the inviscid theoretical predictions complete, we have an understanding of the effect of the magnetic body forces on instability. We have so far assumed two-dimensional flow, free of viscosity. In chapter 3 we stated that our experimental cell is a Hele-Shaw cell. Flows in Hele-Shaw cells are considered lubrication flow. In this chapter we describe in further detail what characterises a Hele-Shaw cell and introduce a viscous Stokes model to capture the radial flow field in a lubrication approximation.

6.1 The governing equations - Stokes flow

The equations derived in section 5.1 model the flow in two-dimensions, with $\mathrm{Re} \gg 1$, such that the viscous terms were neglected and pressure was balanced with the dominating inertial terms. We now consider the case when $\mathrm{Re} \to 0$, where the viscous term dominates the inertial momentum terms. To start, we

return to the dimensional governing model, (5.5)-(5.7),

$$\frac{\mathrm{D}\rho_j}{\mathrm{D}t} + \rho_j \boldsymbol{\nabla}\cdot\mathbf{u}_j = 0, \tag{6.1}$$

$$\frac{\mathrm{D}\mathbf{u}_j}{\mathrm{D}t} = -\frac{1}{\rho_j}\boldsymbol{\nabla}p_j - \boldsymbol{\Omega}\wedge(\boldsymbol{\Omega}\wedge\mathbf{r}) - 2\boldsymbol{\Omega}\wedge\mathbf{u}_j + \frac{\eta_j}{\rho_j}\nabla^2\mathbf{u}_j + \frac{\chi_j}{2\mu_0\rho_j}\boldsymbol{\nabla}B(r,z)^2, \tag{6.2}$$

$$\boldsymbol{\nabla}\cdot\mathbf{u}_j = 0, \tag{6.3}$$

where all quantities are as previously defined.

6.1.1 Dimensionless formulation

The length scale is as for the inviscid case with $[L] = a$. The velocity and time scales remain undetermined as there is not a natural scale to be used. The momentum equation becomes

$$\frac{[U]}{[T]}\frac{\mathrm{D}\mathbf{u}_j'}{\mathrm{D}t'} = -\frac{[P]}{\rho_0 a}\frac{1}{\rho_j'}\boldsymbol{\nabla}'p_j' + a\Omega^2 r'\mathbf{e}_r - 2[U]\Omega\mathbf{e}_z\wedge\mathbf{u}_j' + \frac{[U]\eta_0}{a^2\rho_0}\frac{\eta_j'}{\rho_j'}\nabla'^2\mathbf{u}_j' + \frac{\chi_j B_0^2}{2\mu_0 a\rho_0}\frac{1}{\rho_j'}\boldsymbol{\nabla}'B(r',z')^2, \tag{6.4}$$

where the prime notation is now reintroduced to represent dimensionless quantities. Reformulating, with the Reynold's number as

$$\mathrm{Re} = \frac{[U]a\rho_0}{\eta_0}, \tag{6.5}$$

the Navier-Stokes equations are written as

$$\frac{a}{[U][T]}\frac{\mathrm{D}\mathbf{u}_j'}{\mathrm{D}t'} = -\frac{[P]}{\rho_0[U]^2}\frac{1}{\rho'}\boldsymbol{\nabla}'p_j' - \frac{a^2\Omega^2}{[U]^2}r'\mathbf{e}_r - \frac{2a\Omega}{[U]}\mathbf{e}_z\wedge\mathbf{u}_j' + \frac{1}{\mathrm{Re}}\frac{\eta_j'}{\rho_j'}\nabla'^2\mathbf{u}_j' + \frac{\chi_j B_0^2}{2\mu_0\rho_0[U]^2}\frac{1}{\rho_j'}\boldsymbol{\nabla}'B(r',z')^2, \tag{6.6}$$

with the usual dimensionless incompressibility condition. Taking the time scale to be $[T] = [L]/[U]$ and multiplying through by the Reynolds number, the Navier-

Stokes equation becomes

$$\mathrm{Re}\frac{\mathrm{D}\mathbf{u}_j}{\mathrm{D}t} = \mathrm{Re}\left\{-\frac{[P]}{\rho_0[U]^2}\frac{1}{\rho_j}\boldsymbol{\nabla}p_j - [T]^2\Omega^2 r\mathbf{e}_r + 2\Omega[T]\mathbf{e}_z \wedge \mathbf{u}_j \right. \\ \left. -\frac{\chi_j B_0^2}{2\mu_0\rho_0[U]^2}\frac{1}{\rho_j}\boldsymbol{\nabla}B(r,z)^2\right\} + \frac{\eta_j}{\rho_j}\nabla^2\mathbf{u}_j, \quad (6.7)$$

where the prime notation has been dropped on the understanding that the quantities are dimensionless unless otherwise stated. We now suppose the vertical domain is small such that

$$z,\ \varepsilon \in \{\mathbb{R} \mid 0 < z < b,\ b = \varepsilon[L],\ \varepsilon \ll 1\}, \quad (6.8)$$

and define a further scaled vertical variable z^* such that $z = \varepsilon z^*$. By looking at the dimensionless incompressibility condition and substituting $z = \varepsilon z^*$ we have

$$\frac{1}{r}\frac{\partial(ru)}{\partial r} + \frac{1}{r}\frac{\partial v}{\partial\theta} + \frac{1}{\varepsilon}\frac{\partial w}{\partial z^*} = 0,$$

where, immediately, we must scale the vertical velocity field as $w = \varepsilon w^*$ in order for incompressibility to be satisfied. The Laplacian of the velocity field in cylindrical polar coordinates is

$$\nabla^2\mathbf{u} = \begin{pmatrix} \nabla^2 u - \frac{u}{r^2} - \frac{2}{r^2}\frac{\partial v}{\partial\theta} \\ \nabla^2 v - \frac{v}{r^2} + \frac{2}{r^2}\frac{\partial u}{\partial\theta} \\ \nabla^2 w \end{pmatrix}, \quad \text{where} \quad \nabla^2 = \frac{1}{r}\frac{\partial}{\partial r}\left(r\frac{\partial}{\partial r}\right) + \frac{1}{r^2}\frac{\partial^2}{\partial\theta^2} + \frac{\partial^2}{\partial z^2}.$$

Hence, with the new scaled variables, we have

$$\nabla^2\mathbf{u} = \begin{pmatrix} \frac{1}{\varepsilon^2}\left[\frac{\varepsilon^2}{r}\frac{\partial}{\partial r}\left(r\frac{\partial u}{\partial r}\right) + \frac{\varepsilon^2}{r^2}\frac{\partial^2 u}{\partial\theta^2} + \frac{\partial^2 u}{\partial z^{*2}} - \varepsilon^2\frac{u}{r^2} - \frac{2\varepsilon^2}{r^2}\frac{\partial v}{\partial\theta}\right] \\ \frac{1}{\varepsilon^2}\left[\frac{\varepsilon^2}{r}\frac{\partial}{\partial r}\left(r\frac{\partial v}{\partial r}\right) + \frac{\varepsilon^2}{r^2}\frac{\partial^2 v}{\partial\theta^2} + \frac{\partial^2 v}{\partial z^{*2}} - \varepsilon^2\frac{v}{r^2} + \frac{2\varepsilon^2}{r^{*2}}\frac{\partial u}{\partial\theta}\right] \\ \frac{\varepsilon}{\varepsilon^2}\left[\frac{\varepsilon^2}{r}\frac{\partial}{\partial r}\left(r\frac{\partial w^*}{\partial r}\right) + \frac{\varepsilon^2}{r^2}\frac{\partial^2 w^*}{\partial\theta^2} + \frac{\partial^2 w^*}{\partial z^{*2}}\right] \end{pmatrix}.$$

To leading order in the small aspect parameter, ε, the Laplacian simplifies to

$$\nabla^2\mathbf{u} = \frac{1}{\varepsilon^2}\begin{pmatrix} \frac{\partial^2 u}{\partial z^{*2}} + \mathcal{O}(\varepsilon^2) \\ \frac{\partial^2 v}{\partial z^{*2}} + \mathcal{O}(\varepsilon^2) \\ \varepsilon\frac{\partial^2 w^*}{\partial z^{*2}} + \mathcal{O}(\varepsilon^3) \end{pmatrix}.$$

The governing equation, (6.7), in component form is then

$$\mathbf{e}_r: \quad \mathrm{Re}\left[\frac{\mathrm{D}\mathbf{u}_j}{\mathrm{D}t}\right]_{\mathbf{e}_r} = \mathrm{Re}\left\{-\frac{[P]}{\rho_0[U]^2}\frac{1}{\rho_j}\frac{\partial p_j}{\partial r} + [T]^2\Omega^2 r - 2\Omega[T]v_j + \frac{\chi_j B_0^2}{2\mu_0\rho_0[U]^2}\frac{1}{\rho_j}\frac{\partial}{\partial r}B(r,z)^2\right\} + \frac{1}{\varepsilon^2}\left(\frac{\eta_j}{\rho_j}\frac{\partial^2 u_j}{\partial z^{*2}} + \mathcal{O}(\varepsilon^2)\right), \quad (6.9)$$

$$\mathbf{e}_\theta: \quad \mathrm{Re}\left[\frac{\mathrm{D}\mathbf{u}_j}{\mathrm{D}t}\right]_{\mathbf{e}_\theta} = \mathrm{Re}\left\{-\frac{[P]}{\rho_0[U]^2}\frac{1}{r\rho_j}\frac{\partial p_j}{\partial\theta} + 2\Omega[T]u_j\right\} + \frac{1}{\varepsilon^2}\left(\frac{\eta_j}{\rho_j}\frac{\partial^2 v_j}{\partial z^{*2}} + \mathcal{O}(\varepsilon^2)\right), \quad (6.10)$$

$$\mathbf{e}_z: \quad \mathrm{Re}\left[\frac{\mathrm{D}\mathbf{u}_j}{\mathrm{D}t}\right]_{\mathbf{e}_z} = \mathrm{Re}\left\{-\frac{[P]}{\varepsilon\rho_0[U]^2}\frac{1}{\rho_j}\frac{\partial p_j}{\partial z^*} + \frac{\chi_j B_0^2}{2\varepsilon\mu_0\rho_0[U]^2}\frac{1}{\rho_j}\frac{\partial}{\partial z^*}B(r,z)^2\right\} + \frac{1}{\varepsilon}\left(\frac{\eta_j}{\rho_j}\frac{\partial^2 w_j^*}{\partial z^{*2}} + \mathcal{O}(\varepsilon^3)\right). \quad (6.11)$$

Notice that, in the planar coordinate components $\mathbf{e}_r$ and $\mathbf{e}_\theta$, for $\varepsilon \ll 1$, the viscous term dominates the equations. Whereas, in the vertical component $\mathbf{e}_z$, viscosity

is balanced with the pressure. This indicates two possible choices for the pressure scale when balanced with the viscous term to keep at leading order in ε. By using the Reynolds number definition, the choice of pressure scales are

$$[P] = \frac{\rho_0[U]^2}{\varepsilon^2 \mathrm{Re}} = \frac{[U]\eta_0}{\varepsilon^2 a}, \quad \text{from the planar components} \tag{6.12}$$

$$[P] = \frac{\rho_0[U]^2}{\mathrm{Re}} = \frac{[U]\eta_0}{a}, \quad \text{from the vertical component} \tag{6.13}$$

A suitable choice for the pressure in the lubricated regime is one with the greatest variation to avoid the trivial solution of the velocity field. Hence, pressure is re-scaled with ε^{-2}, and taken to be the scale defined by the planar components. Consequently, by forcing a balance of centrifugal terms with pressure, the horizontal velocity scale is also re-scaled with ε^2 such that

$$[U] = \varepsilon^2 \frac{a^3 \Omega^2 \rho_0}{\eta_0}, \tag{6.14}$$

and a re-scaled Reynold's number is defined as

$$\mathrm{Re} = \varepsilon^2 \left(\frac{a^2 \Omega \rho_0}{\eta_0} \right)^2. \tag{6.15}$$

With the adjusted scales, (6.9)-(6.10) are multiplied through by ε^2 and (6.11) is multiplied through by ε^3 giving the components as

$$\begin{aligned} \mathbf{e}_r: \quad \varepsilon^2 \mathrm{Re} \left[\frac{\mathrm{D}\mathbf{u}_j}{\mathrm{D}t} \right]_{\mathbf{e}_r} &= -\frac{1}{\rho_j} \frac{\partial p_j}{\partial r} + r - 2\varepsilon \mathrm{Re}^{\frac{1}{2}} v_j \\ &\quad + \frac{\chi_j B_0^2}{2\mu_0 r_0^2 \Omega^2 \rho_0} \frac{1}{\rho_j} \frac{\partial}{\partial r} B(r,z)^2 + \frac{\eta_j}{\rho_j} \frac{\partial^2 u_j}{\partial z^{*2}} + \mathcal{O}(\varepsilon^3), \end{aligned} \tag{6.16}$$

$$\mathbf{e}_\theta: \quad \varepsilon^2 \mathrm{Re} \left[\frac{\mathrm{D}\mathbf{u}_j}{\mathrm{D}t} \right]_{\mathbf{e}_\theta} = -\frac{1}{r\rho_j} \frac{\partial p_j}{\partial \theta} + 2\varepsilon \mathrm{Re}^{\frac{1}{2}} u_j + \frac{\eta_j}{\rho_j} \frac{\partial^2 v_j}{\partial z^{*2}} + \mathcal{O}(\varepsilon^3), \tag{6.17}$$

$$\mathbf{e}_z: \quad \varepsilon^3 \mathrm{Re}\left[\frac{\mathrm{D}\mathbf{u}_j}{\mathrm{D}t}\right]_{\mathbf{e}_z} = -\frac{1}{\rho_j}\frac{\partial p_j}{\partial z^*} + \frac{\chi_j B_0^2}{2\mu_0 r_0^2 \Omega^2 \rho_0}\frac{1}{\rho_j}\frac{\partial}{\partial z^*}B(r,z)^2 + \varepsilon^2 \frac{\eta_j}{\rho_j}\frac{\partial^2 w_j^*}{\partial z^{*2}} + \mathcal{O}(\varepsilon^3). \quad (6.18)$$

Recall that the aspect ratio is defined to be a small number. As the Reynold's number is proportional to ε^2, then the relation $\varepsilon^2\mathrm{Re} \ll \varepsilon\mathrm{Re}^{\frac{1}{2}} \ll \mathrm{Re}$ holds. Notice that we recover the dimensional number relating magnetic pressure to inertial pressure as introduced in chapter 5 with

$$\mathrm{Mp}_j = \frac{\chi_j B_0^2}{2\mu_0 a^2 \Omega^2 \rho_0}. \quad (6.19)$$

and taking leading order terms in ε, the governing equations are reduced to

$$\mathbf{e}_r: \quad 0 = -\frac{\partial p_j}{\partial r} + \rho_j r + \mathrm{Mp}_j \frac{\partial}{\partial r}B(r,z)^2 + \eta_j \frac{\partial^2 u_j}{\partial z^2}, \quad (6.20)$$

$$\mathbf{e}_\theta: \quad 0 = -\frac{1}{r}\frac{\partial p_j}{\partial \theta} + \eta_j \frac{\partial^2 v_j}{\partial z^2} \quad (6.21)$$

$$\mathbf{e}_z: \quad 0 = -\frac{\partial p_j}{\partial z} + \mathrm{Mp}_j \frac{\partial}{\partial z}B(r,z)^2, \quad (6.22)$$

where the star notation has been dropped with the understanding that the vertical components have been scaled with ε and inertial and Coriolis terms are negligible compared with the dominating viscous effects as a consequence of the small geometry. Equations (6.20)-(6.22) are the dimensionless form of the governing lubrication model in our Hele-Shaw cell.

6.1.2 Depth averaged velocity field

A modified pressure function defined as

$$\mathrm{P}_{Mj}(r,\theta,z,t) = p_j(r,\theta,z,t) - \mathrm{Mp}_j B(r,z)^2 \quad (6.23)$$

is introduced to simplify the formulation. From (6.22) the modified pressure is found to be independent of z. Using the boundary conditions on the bottom

plate, $z = 0$, and top plate, $z = 1$, allows us to find $u_j(r, \theta, z, t)$ and $v_j(r, \theta, z, t)$ by integrating (6.20) and (6.21) twice, respectively, giving

$$\mathbf{u}_j = \frac{z(z-1)}{2\eta_j}\boldsymbol{\nabla}_H\left(\mathrm{P}_{Mj} - \frac{\rho_j r^2}{2}\right), \tag{6.24}$$

where we define a gradient function in planar coordinates (r, θ) as $\boldsymbol{\nabla}_H$ to be consistent with the notation used by Scase *et al.* [45]. Taking a depth averaged velocity across the vertical domain gives

$$\mathbf{v}_j = \int_{z=0}^{z=1} \mathbf{u}_j \, \mathrm{d}z = -\frac{1}{12\eta_j}\boldsymbol{\nabla}_H\left(\mathrm{P}_{Mj} - \frac{\rho_j r^2}{2}\right). \tag{6.25}$$

which is the effective Darcy law flow for rotational geometry as in Scase *et al.* [46] and is the basis of the linear model used by Schwartz [48] with the inclusion of rotational effects. The procedure that follows is similar to that described by the normal modes solutions in chapter 5. Differences arise within the boundary conditions due to the existence of the aspect ratio. We look for perturbation solutions to the hydrostatic background flow by writing

$$\mathbf{v}_j = \mathbf{v}_{0j} + \mathbf{V}_j(r, \theta, t), \tag{6.26}$$

$$\mathcal{P}_j = \mathcal{P}_{0j} + \epsilon\mathcal{P}_{1j}(r, t)\mathrm{e}^{i(m\theta+\omega t)} \tag{6.27}$$

where $\mathbf{v}_{0j} = \mathbf{0}$ and $\mathcal{P}_{0j}$ are the hydrostatic background velocity and modified pressure, respectively, and ϵ is the initial magnitude of the small disturbance. As the averaged velocity is now two-dimensional and incompressible, we can introduce a streamfunction for the flow as $\mathbf{v}_j = (r^{-1}\psi_{j\theta}, -\psi_r)$, where $\psi_j(r, \theta, t)$ is the streamfunction defined as in (5.24). Writing the averaged velocity components in terms of the defined streamfunction gives

$$\hat{\mathbf{r}}: \quad \epsilon\frac{im}{r}\phi_j(r)\mathrm{e}^{i(m\theta+\omega t)} = -\frac{1}{12\eta_j}\left(\frac{\partial\mathcal{P}_{0j}}{\partial r} + \epsilon\frac{\partial\mathcal{P}_{1j}}{\partial r}\mathrm{e}^{i(m\theta+\omega t)} - \rho_j r\right), \tag{6.28}$$

$$\hat{\theta}: \quad -\epsilon\phi_j(r)_r\mathrm{e}^{i(m\theta+\omega t)} = -\frac{1}{12\eta_j}\left(\frac{1}{r}\frac{\partial\mathcal{P}_{0j}}{\partial\theta} + \epsilon\frac{im\mathcal{P}_{1j}}{r}\mathrm{e}^{i(m\theta+\omega t)}\right), \tag{6.29}$$

where the averaged velocity components are introduced with bar notation, $\mathbf{v}_j = (\bar{u}_j, \bar{v}_j, 0)$ such that,

$$\bar{u}_j = \epsilon \frac{im}{r}\phi_j(r)\mathbb{E}, \quad \bar{v}_j = -\epsilon\phi_j(r)_r\mathbb{E}, \text{ where } \mathbb{E} = \mathrm{e}^{i(m\theta+\omega t)}. \tag{6.30}$$

Looking at the leading order solutions in ϵ we can obtain the initial pressure distribution of the hydrostatic background flow. This can be determined from the radial component and yields

$$\mathcal{P}_{0j}(r,\theta,t) = \frac{\rho_j r^2}{2} + p_{0j}(\theta,t),$$

where p_{0j} is a measured reference pressure. Furthermore, from the azimuthal component, we can see at leading order that $\mathcal{P}_{0j} = \mathcal{P}_{0j}(r,t)$ only. Therefore the reference pressure is only dependent on time; that is, $p_{0j} = p_{0j}(t)$. Taking the first order in ϵ we find, from the azimuthal component, that

$$\mathcal{P}_{1j} = -\frac{12i\eta_j\phi_{jr}r}{m}.$$

Hence, the modified pressure, (6.23), can be written as

$$\mathcal{P}_j(r,\theta,t) = \frac{\rho_j r^2}{2} + p_{0j} - \epsilon\frac{12i\eta_j r\phi_{jr}}{m}\mathrm{e}^{i(m\theta+\omega t)} \tag{6.31}$$

which can be rearranged for the fluid pressure when we substitute (6.23) into (6.31) to get

$$p_j(r,\theta,z,t) = p_{0j}(t) + \frac{\rho_j r^2}{2} + \mathrm{Mp}_j B(r,z)^2 - \epsilon\frac{12i\eta_j r\phi_{jr}}{m}\mathrm{e}^{i(m\theta+\omega t)}. \tag{6.32}$$

Substituting $\mathcal{P}_{1j}$ into the radial component, (6.28) finds a second order ODE for $\phi_j(r,t)$ a first order in ϵ

$$\frac{m^2}{r}\phi_j = \frac{\mathrm{d}}{\mathrm{d}r}(r\phi_{jr})$$

which yields solutions of the form

$$\phi_j(r) = c_{0,j} r^{-m} + c_{1,j} r^m.$$

As before, we consider two layers of fluid, an outer solution when $r > r_0$ and an inner solution when $r < r_0$. Further, we simplify the solutions by imposing regularity at the origin. That is, $|\phi_1(r)| < \infty$ as $r \to 0$ forcing $c_{0,1} = 0$. Additionally, on the boundary at $r = 1$, the outer velocity potential of the fluid must be zero so that $c_{1,2} = -c_{0,2}$. The solution in each layer is therefore

$$\phi_j(r) = \begin{cases} c_{1,1} r^m, & \text{when } j = 1, \text{ by velocity regularity,} \\ c_{0,2}\left(r^{-m} - r^m\right), & \text{when } j = 2, \text{ by no-penetration at } r = 1. \end{cases}$$

6.1.3 Boundary conditions

The boundary conditions are similar to that of chapter 5 but with changes to the dimensionless scales as a consequence of the small aspect ratio. The dimensional kinematic boundary condition is

$$\frac{\mathrm{D}\mathcal{I}}{\mathrm{D}t} = 0 \tag{6.33}$$

where $\mathcal{I}$ is the definition of the interface described by equation (5.19) and, the new time scale is taken to be

$$T = \frac{\eta_0}{\Omega^2 \rho_0 a^2}.$$

Substituting in the dimensionless averaged velocities, given by (6.30), we find at the first order in ϵ

$$-i\omega\mathbb{E} + \varepsilon^2 \frac{im}{r} \phi_j \mathbb{E} = 0,$$

which, at the interface, gives the kinematic condition as

$$\phi_j(r_0) = \frac{\omega r_0}{m\varepsilon^2}. \tag{6.34}$$

The kinematic condition is used to fully determine the potential functions as

$$\phi_1(r) = \frac{\omega r_0^{1-m}}{m\varepsilon^2} r^m, \qquad \text{with} \quad \frac{\partial}{\partial r}\phi_1(r) = \frac{\omega r_0^{1-m}}{\varepsilon^2} r^{m-1},$$
$$\phi_2(r) = \frac{\omega r_0}{m\varepsilon^2} \frac{(r^{-m} - r^m)}{(r_0^{-m} - r_0^m)}, \qquad \text{with} \quad \frac{\partial}{\partial r}\phi_2(r) = -\frac{\omega r_0}{\varepsilon^2} \frac{(r^{-m-1} + r^{m-1})}{(r_0^{-m} - r_0^m)}.$$

The dimensional stress tensor scales with pressure. As such, the dimensionless form of the stress tensor, reflecting the small aspect ratio is

$$\underline{\underline{\boldsymbol{\sigma}}}_j = \begin{pmatrix} -p_j + 2\varepsilon^2\eta_j \frac{\partial \bar{u}_j}{\partial r} & \varepsilon^2\eta_j \left(\frac{1}{r}\frac{\partial \bar{u}_j}{\partial \theta} + \frac{\partial \bar{v}_j}{\partial r} - \frac{\bar{v}_j}{r}\right) & 0 \\ \varepsilon^2\eta_j \left(\frac{1}{r}\frac{\partial \bar{u}_j}{\partial \theta} + \frac{\partial \bar{v}_j}{\partial r} - \frac{\bar{v}_j}{r}\right) & -p_j + 2\varepsilon^2\eta_j \left(\frac{\bar{u}_j}{r}\right) & 0 \\ 0 & 0 & -p_j \end{pmatrix}.$$

At first order in perturbations, $\mathcal{O}(\epsilon)$, we have the stress traction vector as

$$\underline{\underline{\boldsymbol{\sigma}}}_j \cdot \mathbf{n} = \begin{pmatrix} -p_j + 2\varepsilon^2\eta_j \frac{\partial \bar{u}_j}{\partial r} + \mathcal{O}(\epsilon^2) \\ \varepsilon^2\eta_j \left(\frac{1}{r}\frac{\partial \bar{u}_j}{\partial \theta} + \frac{\partial \bar{v}_j}{\partial r} - \frac{\bar{v}_j}{r}\right) + \epsilon\frac{im}{r}\mathrm{e}^{i(m\theta+\omega t)} p_j + \mathcal{O}(\epsilon^2) \\ 0 \end{pmatrix}.$$

Substituting (6.32) into the stress traction vector and evaluating on the interface by expanding at $r = r_0$ giving

$$\underline{\underline{\boldsymbol{\sigma}}} \cdot \mathbf{n} = \begin{pmatrix} \mathcal{F}_{1,j}(r_0, t) + \epsilon\mathcal{F}_{2,j}(r_0, t) + \mathcal{O}(\epsilon^2) \\ \epsilon\mathcal{G}_{1,j}(r_0, t) + \mathcal{O}(\epsilon^2) \\ 0 \end{pmatrix},$$

where we have introduced the functions $\mathcal{F}_{1,j}, \mathcal{F}_{2,j}$ and $\mathcal{G}_{1,j}$ for clarity as

$$\begin{aligned}
\mathcal{F}_{1,j}(r_0,t) &= -p_0(t) - \frac{r_0^2\rho}{2} - \mathrm{Mp}B(r_0,z)^2, \\
\mathcal{F}_{2,j}(r_0,t) &= \left\{ \frac{12i\eta_j r_0 \phi_{jr}(r_0)}{m} + \left[-\rho_j r_0 - \mathrm{Mp}_j \frac{\mathrm{d}}{\mathrm{d}r} B(r,z)^2 \Big|_{r=r_0} \right] \right. \\
&\qquad \left. + 2im\varepsilon^2\eta_j \left(\frac{\phi_{jr}(r_0)}{r_0} - \frac{\phi_j(r_0)}{r_0^2} \right) \right\} \mathbb{E}, \\
\mathcal{G}_{1,j}(r_0,t) &= \left\{ \varepsilon^2\eta_j \left(-\frac{m^2\phi_j(r_0)}{r_0^2} - \phi_{jrr}(r_0) + \frac{\phi_{jr}(r_0)}{r_0} \right) \right. \\
&\qquad \left. + im \left[p_{0j}(t) + \frac{r_0^2\rho_j}{2} + \mathrm{Mp}_j B(r_0,z)^2 \right] \right\} \mathbb{E}.
\end{aligned}$$

With the appropriate dimensional scales, the stress continuity is

$$\left[\underline{\underline{\boldsymbol{\sigma}}} \cdot \mathbf{n} \right]_-^+ = \frac{1}{\mathrm{We}} \left(\boldsymbol{\nabla} \cdot \mathbf{n} \right) \mathbf{n},$$

where the Weber number is defined as

$$\mathrm{We} = \frac{a^3\Omega^2\rho_0}{\gamma}.$$

The normal stress continuity is then expressed as

$$\left[\frac{12r_0 i\eta\phi_r(r_0)}{m} - \rho r_0 - \mathrm{Mp} \left. \frac{\partial B^2}{\partial r} \right|_{\substack{r=r_0 \\ z=z_0}} + 2im\varepsilon^2\eta \left(\frac{\phi_r(r_0)}{r_0} - \frac{\phi(r_0)}{r_0^2} \right) \right]_-^+ = -\frac{1}{\mathrm{We}} \frac{(m^2-1)}{r_0^2}. \quad (6.35)$$

6.1.4 Dispersion relation in a lubricated model

Substituting the known potential functions evaluated at the initial interface, the normal stress condition becomes

$$\begin{aligned}
&\frac{12ir_0\omega}{m\varepsilon^2} \left(\eta_1 + \eta_2 \frac{(1+r_0^{2m})}{(1-r_0^{2m})} \right) + (\rho_2 - \rho_1) r_0 + (\mathrm{Mp}_2 - \mathrm{Mp}_1) \left. \frac{\partial B^2}{\partial r} \right|_{\substack{r=r_0 \\ z=z_0}} \\
&\qquad + 2im\omega \left\{ \eta_1 + \eta_2 \frac{(1+r_0^{2m})}{(1-r_0^{2m})} + \frac{\eta_2 - \eta_1}{m} \right\} = -\frac{1}{\mathrm{We}} \frac{(m^2-1)}{r_0^2}, \quad (6.36)
\end{aligned}$$

which can be rearranged to give the dimensionless dispersion relation for the Hele-Shaw flow as

$$\omega(m) = \frac{im}{2}\left\{\mathcal{A}r_0 + \frac{(m^2-1)}{2r_0^2\mathrm{We}} + \frac{(\chi_2-\chi_1)}{4\mu_0\rho_0 a^2\Omega^2}B_0^2\left.\frac{\partial B^2}{\partial r}\right|_{\substack{r=r_0\\z=z_0}}\right\} \times\left\{\left[\frac{6r_0^2}{\varepsilon^2}+m^2\right]\left(\frac{1+\eta r_0^{2m}}{1-r_0^{2m}}\right)+m\eta\right\}^{-1}. \quad (6.37)$$

The dimensional form is recovered by the dimensional scales defined previously,

$$\omega(m) = \frac{imr_0}{2\eta_0}\left\{\mathcal{A}r_0\rho_0\Omega^2 + \frac{(m^2-1)\gamma}{2r_0^2} + \frac{(\chi_2-\chi_1)}{4\mu_0}\left.\frac{\partial B^2}{\partial r}\right|_{\substack{r=r_0\\z=z_0}}\right\} \times\left\{\left[\frac{6r_0^2}{b^2}+m^2\right]\left(\frac{a^{2m}+\eta r_0^{2m}}{a^{2m}-r_0^{2m}}\right)+m\eta\right\}^{-1}, \quad (6.38)$$

where all terms are now in dimensional form and $\eta = (\eta_2-\eta_1)/(\eta_2+\eta_1)$ is a number quantifying the viscosity contrast. In contrast to the inviscid dispersion relation, (5.58), this form is purely imaginary with no real solutions, concluding that there are no travelling wave solutions at $r = r_0$, only that perturbations to the interface will either grow or decay. This follows from the zero inertia assumption in the Stokes flow limit. By taking the unbounded domain limit $a \to \infty$, we immediately recover equation (3.75) from Scase & Hill [46], but with the additional magnetic forcing term.

The aim of the preceding section has been to introduce a robust model to predict the most unstable wavenumber in our experiments. As the experimental set-up includes a Hele-Shaw cell with a small gap, it follows that a Hele-Shaw model is an appropriate choice for prediction. We now make comparisons between the experimental data as collected in chapter 3 and the dispersion relation derived in (6.38).

6.2 Comparison and discussion

Here, we compare our theoretical predictions with our experimental results. We draw attention to and recall the experimental results presented in chapter 4. Figure 6.1 shows the fastest growing wavenumber for a range of angular velocities as determined experimentally. The data are as those in figure 4.18. By calculating the mean absolute error (MAE) as the mean average of the residuals with

$$\mathrm{MAE} = \frac{1}{n}\sum_{j=1}^{n}\left|\max_{m=2,\ldots,6}\left\{\frac{\partial\omega_j}{\partial m}\right\} - O_j\right|, \tag{6.39}$$

where the maximum is taken over all wave modes m; $n = 8$ is the number of data points and O_j is the $j-$th data point for the experiment with target angular velocity Ω_j, we find the MAE to be 0.65. The units of the MAE are dimensionless as they represent the error in the wavenumbers, implying that the average error in the residuals between experimental results and prediction is within one wavenumber. Additionally, the R^2 statistic measures 0.60, meaning that 60% of the variation in our data is explained by the model we used. The remaining 40% may be reduced if further experiments with different angular velocity parameters, were carried out.

Note that, the model is continuous in m, but non-integer m are not physically valid. By discretising the HS-model to find the fastest growing integer m at each Ω, we get a discrete variant of the HS-model with MAE is 0.62, and associated R^2 value of 0.55. Though the discrete model does account for as much data variation as the continuous model, the MAE is marginally improved. Therefore, the, the continuous HS-model is a more suitable choice for predicting the fastest growing wavenumber, as it can better account the random errors associated with experimental repetitions.

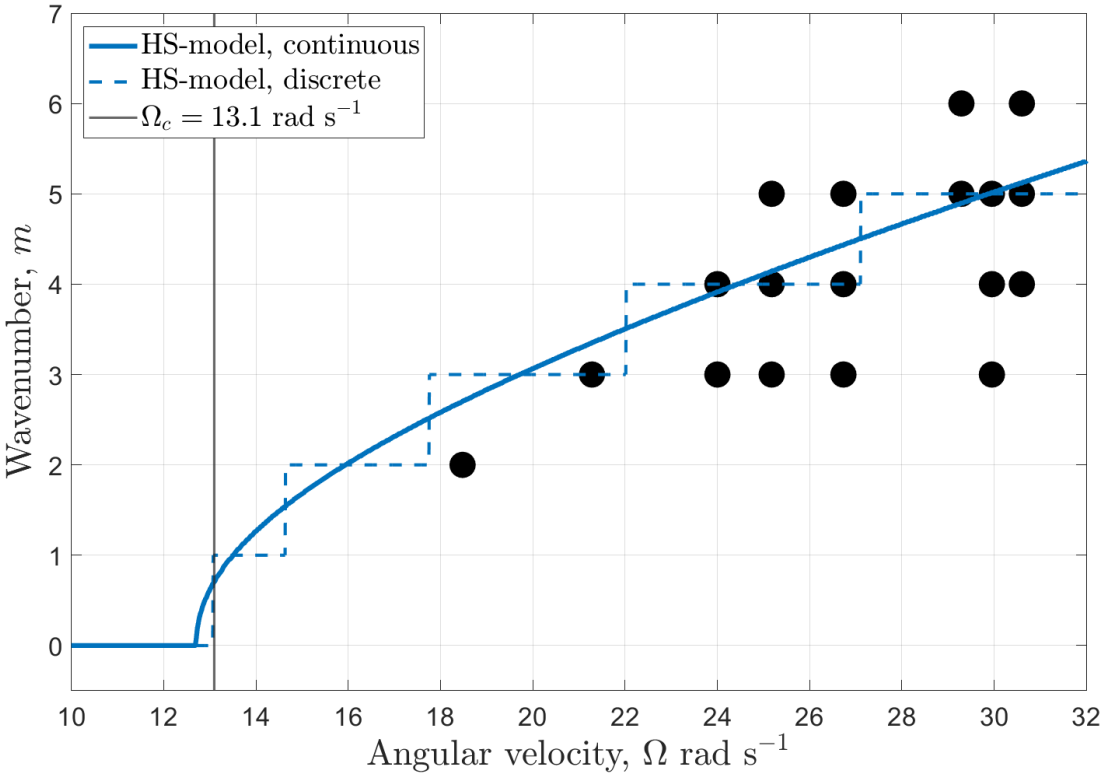

Figure 6.1: Fastest growing wavenumbers, as determined experimentally (reproduced from figure 4.18), in addition to the Hele-Shaw model (blue) in both its continuous and discrete form. The red stars are the mean value of the most dominant modes in our experiments.

Figure 6.2 shows the individual growth rates for each wavenumber as Ω increases. Normalising both the growth rates of the predictive model and the experimental results by the mean growth rate for each m, gives the result of figure 6.3 highlighting the qualitative similarity. While the initial fit is seen to be qualitatively acceptable, there is a clear quantitative discrepancy; predicting significantly greater growth rates than observed. Nevertheless, unstable growth rates at each measured angular velocity are all greater than a value of Ω_c which is consistent with our prediction, showing that each wavenumber is stable for $\Omega < \Omega_c$ given the parameters outlined in table 4.4. The quantitative discrepancy in figure 6.2 indicate that the theoretical model used may not be capturing the true properties of our experiments. In the model, the adhesive drag from fluid contact lines against the glass has been ignored as we took a two-dimensional velocity average in the formulation, neglecting the effect on the fluid flow of the

upper and lower glass plate boundaries present in the experiments. Though we took measures to reduce the effect of adhesive forces present from an advancing contact line, the molecular interactions at the $\mathrm{MC_{PC}} - \mathrm{PC_{MC}} -$ Glass Disc contact line will affect the macroscopic fluid motion under rotation, [52]. The properties of the fluid layers within the experiment may also change significantly to the original measurement in chapter 3, causing an apparent increase in growth rate suppression within the theoretical model.

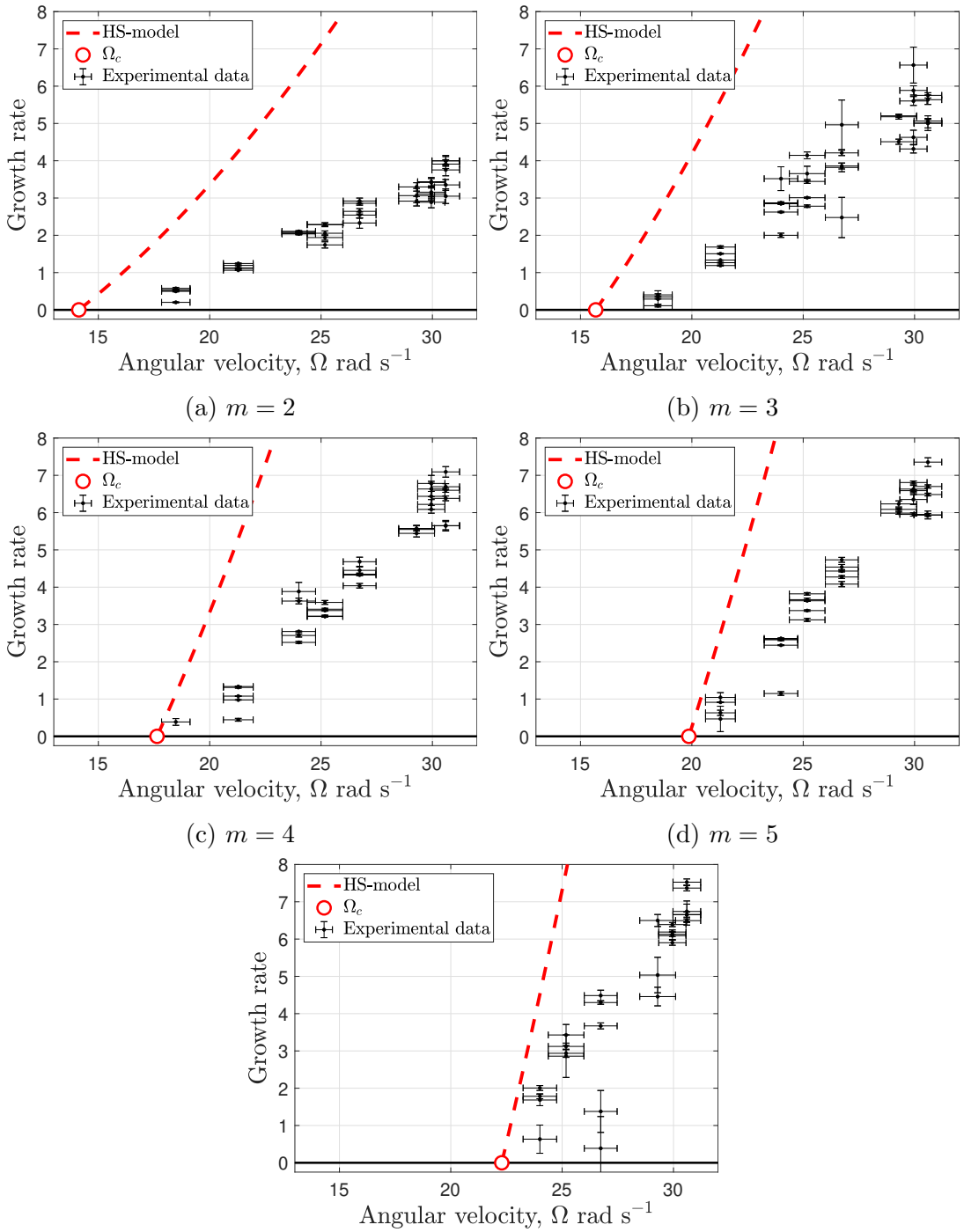

(a) $m = 2$ (b) $m = 3$

(c) $m = 4$ (d) $m = 5$

(e) $m = 6$

Figure 6.2: Wavenumber growth rate for $m = 2, 3, 4, 5, 6$. The HS-model is not a good prediction for the experimental data. All data points lie to the right of Ω_c. This is when $\Omega > \Omega_c$, the critical angular velocity for each wavenumber. The centrifugal force is inducing instability of each m with increasing growth rate as Ω increases.

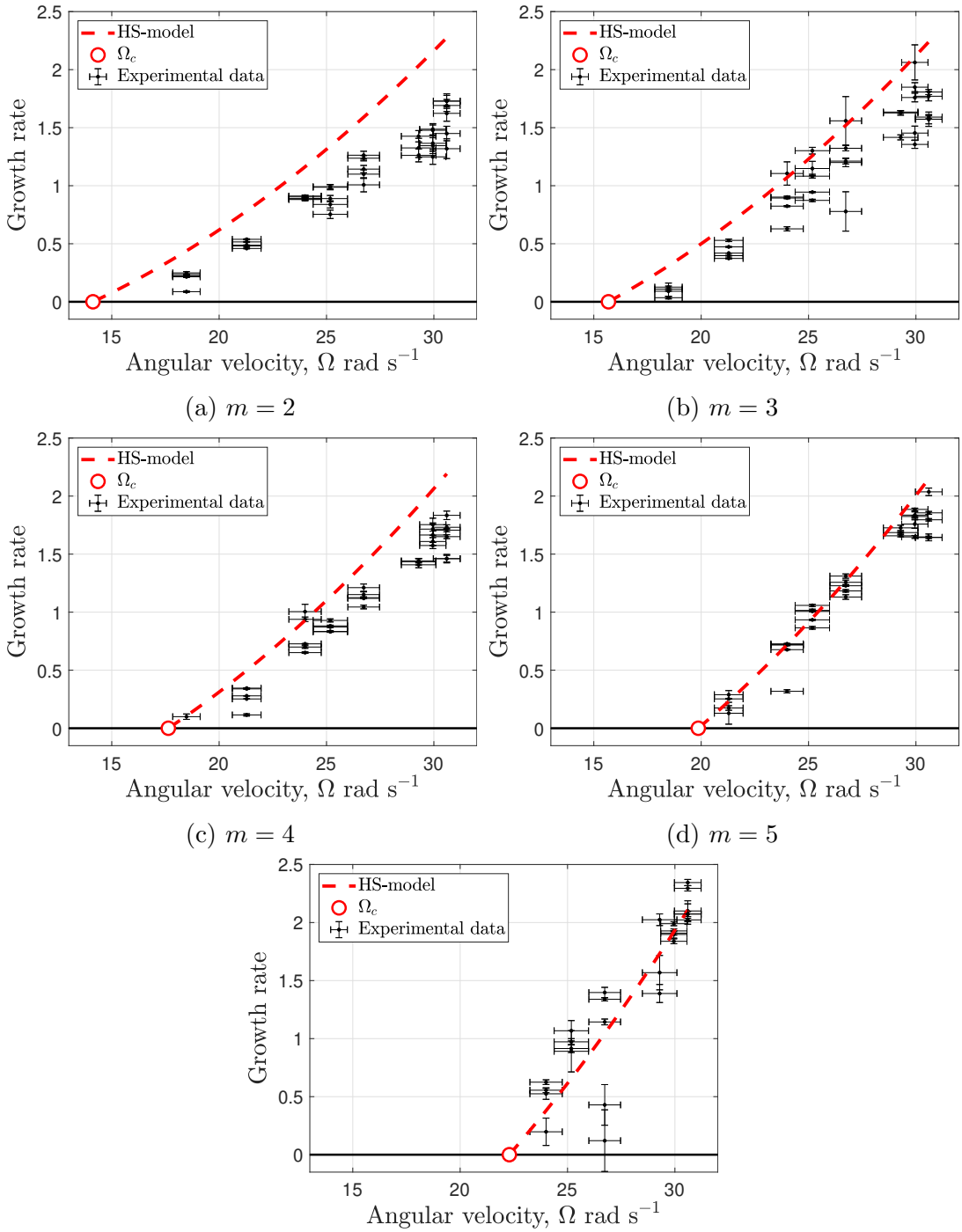

(a) $m = 2$ (b) $m = 3$

(c) $m = 4$ (d) $m = 5$

(e) $m = 6$

Figure 6.3: Normalised growth rate for $m = 2, 3, 4, 5, 6$. There is close agreement between the HS-model and experimental data.

During our experiments, the fact that (i) the model successfully predicts the most dominant wave mode, and that (ii) the growth rates predicted by the model agree with experiment once the growth rates are normalised as described above, suggests a possible error in the evaluation of the prefactor in (6.38). This pref-

actor includes the initial radius of the interface, r_0, and the mean viscosity η_0. The radius r_0 was measured experimentally but the viscosity was not. We have so far assumed that the dynamic viscosity of the propylene carbonate solution (PC_{MC}) is equal to that of pure propylene carbonate liquid, $\eta_1 = 2.8 \times 10^{-3}$ Pa s at 20°C, [22]. Similarly, we have assumed that the dynamic viscosity of the manganese chloride solution (MC_{PC}) is equal to that of water. We now question that assumption.

We fitted the model growth rates to the experimental data using non-linear curve-fitting, setting η_1 and η_2 as adjustable parameters. Doing so, we obtain the following values for the dynamic viscosity of each of the two fluids:

$$\eta_1^f = 7.7 \times 10^{-3} \pm 6.1 \times 10^{-4} \text{ Pa s}, \tag{6.40}$$

$$\eta_2^f = 5.8 \times 10^{-3} \pm 7.0 \times 10^{-4} \text{ Pa s}, \tag{6.41}$$

where η_1^f and η_2^f are the fitted dynamic viscosity for PC_{MC} and MC_{PC}, respectively. Figure 6.4 shows the results of the fit, with a MAE of at most 0.47 rad s^{-1} between our data and model. We note, however, that the values of η_1^f and η_2^f obtained by this fit are approximately 3 and 6 times larger than those of pure propylene carbonate and water, respectively, which is surprising. One possible explanation may lie in the conductivity of the fluids, which we have not so far considered. The presence of manganese and chlorine ions make both liquids conductive. It is well-known that a conducting fluid moving through a magnetic field experiences an additional dissipating force due to electromagnetic induction [13], which may appear as a viscous-like drag on the fluid flow. Further work is recommended to understand this effect.

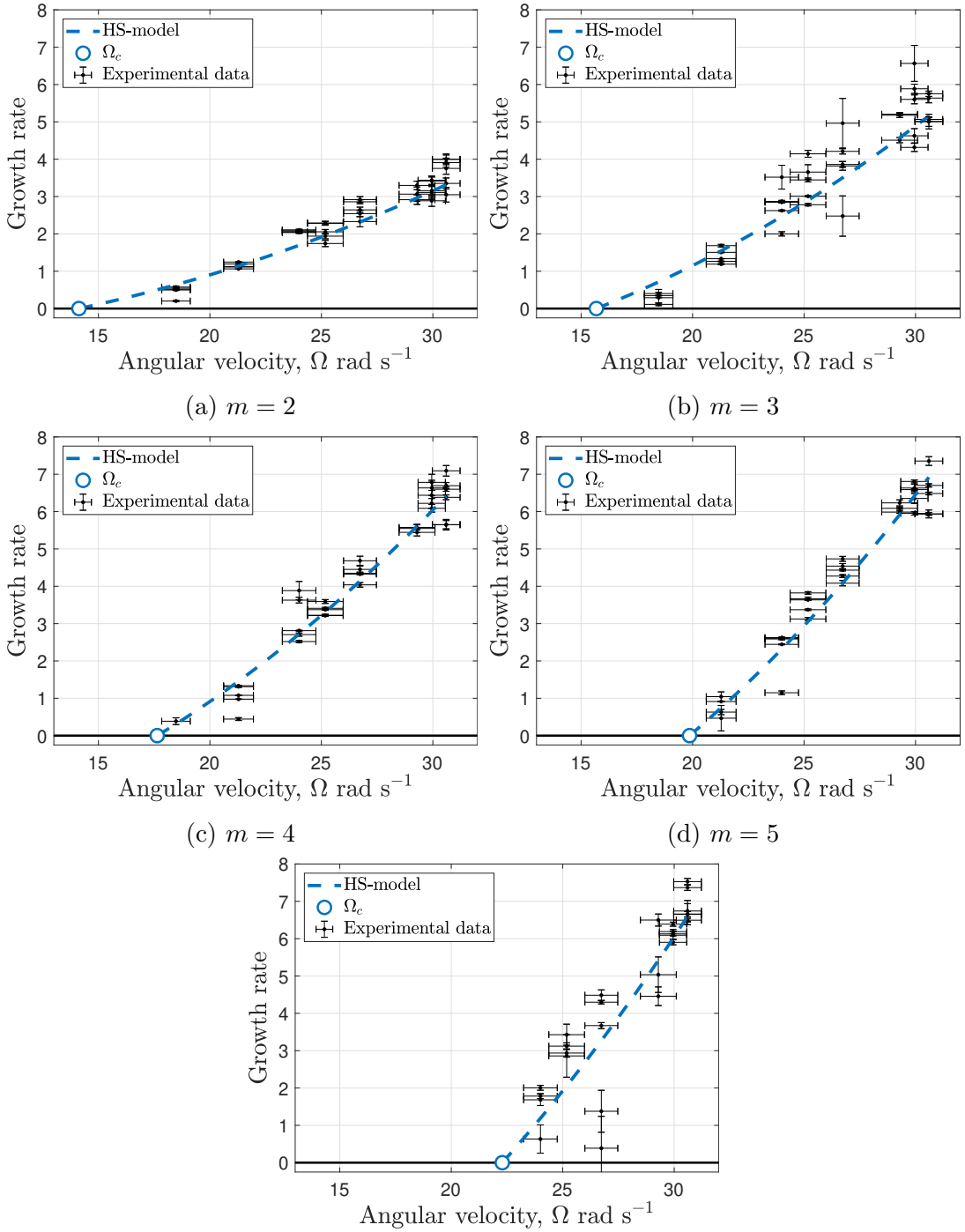

(a) $m = 2$ (b) $m = 3$

(c) $m = 4$ (d) $m = 5$

(e) $m = 6$

Figure 6.4: Growth rate for $m = 2, 3, 4, 5, 6$ without normalisation.

This chapter has been devoted to the further development of a theoretical model to capture the radial instabilities observed in our experiments, as well as the comparison to our experimental data. In contrast to experiments carried out in horizontal strata, where the fluid layers appear vertically aligned, a

novel approach using a magnetic field to set the initial conditions in a controlled environment was taken. There have been many approaches to inducing Rayleigh-Taylor instability (RTI) in experiments [3, 30, 37, 54], and all have intricate methodologies to ensure well-controlled results. These experiments investigate classical RTI in systems of one fluid overlying another in horizontal strata. Their focus has been to induce instability in the presence of a gravitational field. In our experiments, the magnetic field has benefited us by balancing the force of gravity and allowing us to perform radial instability in a cylindrical geometry, analogous to the horizontal cases of previous authors. Additionally, the presence of the magnetic field and the magnetic properties of the fluids involved allow us to separate the fluid layers without concern for the initial density difference, reducing experimental complexity.

Chapter 7

Conclusions and closing remarks

7.1 Thesis summary

The aim of this work has been to experimentally investigate radial instabilities under the influence of an externally applied magnetic field and make comparisons with theoretical models. At the start of this thesis we introduced the topic of fluid-fluid instabilities. It is area of research with applications in many fields such as geophysical fluid dynamics and astrophysics. In chapter 2 we described the forces at work in the problem under consideration, outlining the effects of magnetism on diamagnetic and paramagnetic objects. We found that the magnetic body force is conservative and that within the magnetic field of the solenoid magnet there are regions that can sustain diamagnetic levitation. This idea was extended to include the necessary conditions for this levitation to be stable. The magneto-Archimedes principle was introduced and described.

In chapter 3, we set out the experimental methodology. We described the challenges of conducting experiments within an open bore magnet. We also discussed the procedure of ensuring the experimental cell was free of air bubbles to increase the repeatability of our results. Physical properties of the fluids were measured and compared with known literature values, where available. By using the equilibrium points in the magnet bore, we were able to measure the difference

in volume magnetic susceptibilities between the two fluids. This also allowed us to obtain an empirical value for the volume magnetic susceptibility of propylene carbonate, in the absence of a literature source. Chapter 4 focused on extracting the data from the images. We discussed the experimental uncertainties to ensure that the data we were extracting was as close an approximation to the fluid-fluid interface as possible. We then used Fourier series to find the amplitudes of various wave modes contributing to the contour of the extracted interface. By taking the logarithm of the amplitudes over time, we were able to obtain the growth rates of wave modes $m = 2$ to $m = 6$. We were also able to determine the most unstable mode, i.e. the mode with the greatest growth rate. We presented our experimental results in section 4.5 and listed the growth rates of all our experiments with their associated uncertainties. We did not report data for modes $m = 0$ and $m = 1$ as we found that $m = 0, 1$ contributions were negligible in comparison with higher order modes.

In order to make comparisons with the experimental data. We derived the governing model for two-phase fluid instabilities by first assuming an inviscid two-dimensional system in chapter 5. We were able to examine the suppressing effect of surface tension on the growth of perturbations and discussed the requirements to induce instability by altering various parameters such as surface tension and the density stratification. We were able to show the effect of the magnetic field by varying the strength of the field at $B(0, 0)$. For $(\chi_1 - \chi_2) < 0$ the radial magnetic field acted with surface tension, opposing centrifugal forces to slow the growth of instability instability. Conversely, for $(\chi_1 - \chi_2) > 0$ the radial magnetic field acted in the same direction as centrifugal forces to further increase the growth rate of instability.

We extended the model to include viscous effects in a circular Hele-Shaw cell in chapter 6. Unlike the inviscid model, in the Stokes flow approximation, we found that the dispersion relation, given by (6.38), only has an imaginary part; the

instability has no travelling wave solutions. The comparisons made between the Hele-Shaw model and our experimental data show good agreement between the two when considering the fastest growing wavenumber. However, using our initial assumptions on the value of dynamic viscosity, η_1 and η_2, the theoretical model did not agree with the experimental data when we looked at the individual growth rates for each observed wavenumber, as can be seen in figure 6.2. Nevertheless the trend in the experimental data followed our growth model, given by (6.38), leading us to investigate the possibility of different dynamic viscosity values. Indeed, by assuming η_1 and η_2 to be unknown parameters, we were able to fit our model to the experimental data, see figure 6.4, suggesting other physical phenomena are affecting results. This conclusion calls for further work to be carried out to consider additional effects suppressing predicted growth rates.

7.2 Closing remarks and future work

One key difference between the theoretical model and our experiments is that the angular velocity was assumed to be instantaneous in the model. Indeed, for the Stokes approximation we find that the influence of angular acceleration is negligible due to the dominance of viscous forces over inertia. However, the presence of lower order wave modes in our results (figure 4.16) show that the acceleration phase is important and does affect results. During this phase, lower order wave modes are excited and contribute to instability. Investigating the angular acceleration phase in detail can be a topic for further research, with the aim of understanding the importance of contribution to interfacial instability.

The next natural step of this work is to look at ways of extending the experimental method for a rotating column of two fluids. We may be able to make direct comparisons with theoretical and numerical simulations provided by Scase and Sengupta [47]. As with the Hele-Shaw case, much consideration must be taken in the method for creating the initial condition.

Bibliography

[1] Alvarez-Lacalle, E., Ortin, J., and Casademunt, J. Low viscosity contrast fingering in a rotating hele-shaw cell. *Physics of Fluids 16*, 4 (2004), 908–924.

[2] Baldwin, K., Scase, M., and Hill, R. The inhibition of the rayleigh-taylor instability by rotation. *Scientific reports 5* (07 2015), 11706.

[3] Banerjee, A. Rayleigh-Taylor Instability: A Status Review of Experimental Designs and Measurement Diagnostics. *Journal of Fluids Engineering 142*, 12 (10 2020). 120801.

[4] Batchelor, G. K. *An Introduction to Fluid Dynamics*. Cambridge Mathematical Library. Cambridge University Press, 2000.

[5] Beaugnon, E., and Tournier, R. Levitation of organic materials. *Nature 349*, 6309 (Feb 1991), 470–470.

[6] Berry, M. V., and Geim, A. K. Of flying frogs and levitrons. *European Journal of Physics 18*, 4 (jul 1997), 307–313.

[7] Betti, R., and Hurricane, O. A. Inertial-confinement fusion with lasers. *Nature Physics 12*, 5 (May 2016), 435–448.

[8] Bongrand, G., and Tsai, P. A. Manipulation of viscous fingering in a radially tapered cell geometry. *Phys. Rev. E 97* (Jun 2018), 061101.

[9] Burger, W., and Burge, M. J. *Digital Image Processing*. Springer London, 2016.

[10] Carrillo, L., Magdaleno, F. X., Casademunt, J., and Ortín, J. Experiments in a rotating hele-shaw cell. *Phys. Rev. E 54* (Dec 1996), 6260–6267.

[11] Carrillo, L., Soriano, J., and Ortin, J. Radial displacement of a fluid annulus in a rotating hele–shaw cell. *Physics of Fluids 11*, 4 (1999), 778–785.

[12] Catherall, A. T., Eaves, L., King, P. J., and Booth, S. R. Magnetic levitation: Floating gold in cryogenic oxygen. *nat 422*, 6932 (apr 2003), 579.

[13] Davidson, P. A. *An introduction to magnetohydrodynamics*. Cambridge texts in applied mathematics ; 25. Cambridge University Press, 2001.

[14] Ding, L., and Goshtasby, A. On the canny edge detector. *Pattern Recognition 34*, 3 (2001), 721–725.

[15] Drazin, P. G. *Introduction to Hydrodynamic Stability*. Cambridge Texts in Applied Mathematics. Cambridge University Press, 2002.

[16] Edmund Optics. Sapphire windows. https://www.edmundoptics.co.uk/f/sapphire-windows/12234/. Accessed: 18.08.2021.

[17] Feynman, R., Leighton, R. B., and Sands, M. *The Feynman lectures on physics, volume II: Mainly electromagnetism and matter*. Basic books, 2011.

[18] Feynman, R., Leighton, R. B., and Sands, M. *The Feynman lectures on physics, volume III: Quantum mechanics*. Basic books, 2011.

[19] Gross, S., and Reusken, A. Numerical simulation of continuum models for fluid-fluid interface dynamics. *The European physical journal. ST, Special topics 222*, 1 (2013), 211–239.

[20] Hachisu, I., Matsuda, T., Nomoto, K., and Shigeyama, T. Rayleigh-taylor instabilities and mixing in the helium star models for type ib/ic supernovae. *The Astrophysical Journal 368* (01 1991), L27–L30.

[21] Hansen, F., and Rødsrud, G. Surface tension by pendant drop: I. a fast standard instrument using computer image analysis. *Journal of Colloid and Interface Science 141*, 1 (1991), 1–9.

[22] Haynes, W. M., Lide, D. R., and Bruno, T. J. *CRC handbook of chemistry and physics : a ready-reference book of chemical and physical data*, ninety-seven edition ed. Boca Raton, Florida ; London, [England] ; New York : CRC Press, 2017.

[23] Heister, S. Boundary element methods for two-fluid free surface flows. *Engineering analysis with boundary elements 19*, 4 (1997), 309–317.

[24] Hirota, N., Ikezoe, Y., Uetake, H., Kaihatsu, T., Takayama, T., and Kitazawa, K. Magneto-archimedes levitation and its application. *RIKEN Rev. 44* (01 2002).

[25] Hoskins, R. Chapter 6 - fourier series and transforms. In *Delta Functions (Second Edition)*, R. Hoskins, Ed., second edition ed. Woodhead Publishing, 2011, pp. 128–153.

[26] Keulegan, G. H. Interfacial instability and mixing in stratified flows. *Journal of research of the National Bureau of Standards 43* (1949), 487.

[27] Kittel, C. *Introduction to solid state physics / Charles Kittel.*, 7th ed. ed. Wiley, New York, 1996.

[28] Krüger, T., Frijters, S., Günther, F., Kaoui, B., and Harting, J. Numerical simulations of complex fluid-fluid interface dynamics. *The European physical journal. ST, Special topics 222*, 1 (2013), 177–198.

[29] Kuchel, P., Chapman, B., Bubb, W., Hansen, P., Durrant, C., and Hertzberg, M. Magnetic susceptibility: Solutions, emulsions, and cells. *Concepts in Magnetic Resonance Part A 18A*, 1 (2003), 56–71.

[30] Lawrie, A. G. W., and Dalziel, S. B. Rayleigh-taylor mixing in an otherwise stable stratification. *Journal of Fluid Mechanics 688* (Dec 10 2011), 507–527. Copyright - Copyright © Cambridge University Press 2011; Document feature - ; Last updated - 2015-08-15.

[31] Lewis, D. J. The instability of liquid surfaces when accelerated in a direction perpendicular to their planes. II. *Proceedings of the London Mathematical Society 202*, 1068 (1950), 81–96.

[32] Liao, L. *Diamagnetic levitation of liquid-grain systems and liquid drops.* PhD thesis, University of Nottingham, 2016.

[33] Lord Rayleigh. Investigation of the character of the equilibrium of an incompressible heavy fluid of variable density. *Proceedings of the London Mathematical Society s1-14*, 1 (1882), 170–177.

[34] Mahady, K., Afkhami, S., and Kondic, L. A volume of fluid method for simulating fluid/fluid interfaces in contact with solid boundaries. *Journal of computational physics 294* (2015), 243–257.

[35] Mangin, P., and Kahn, R. *TYPE II SUPERCONDUCTORS.* Springer International Publishing, Cham, 2017, pp. 111–145.

[36] McRobbie, D. W., Moore, E. A., Graves, M. J., and Prince, M. R. *MR: What's the Attraction?*, 3 ed. Cambridge University Press, 2017, p. 1–8.

[37] Morgan, R. V., Likhachev, O. A., and Jacobs, J. W. Rarefaction-driven rayleigh-taylor instability. part 1. diffuse-interface linear stability measurements and theory. *Journal of Fluid Mechanics 791* (Mar 25 2016), 34–60. Copyright - © 2016 Cambridge University Press; Document feature - ; Last updated - 2017-04-13.

[38] Moumouzias, G., and Ritzoulis, G. Viscosities and densities for propylene carbonate + toluene at 15, 20, 25, 30, and 35.degree.c. *Journal of Chemical & Engineering Data 37*, 4 (1992), 482–483.

[39] Nixon, M. S., and Aguado, A. S. Chapter 4 - low-level feature extraction (including edge detection). In *Feature Extraction and Image Processing for Computer Vision (Third Edition)*, M. S. Nixon and A. S. Aguado, Eds., third edition ed. Academic Press, Oxford, 2012, pp. 137–216.

[40] Novotny, P., and Sohnel, O. Densities of binary aqueous solutions of 306 inorganic substances. *Journal of Chemical and Engineering Data 33*, 1 (1988), 49–55.

[41] Porth, O., Komissarov, S. S., and Keppens, R. Rayleigh–Taylor instability in magnetohydrodynamic simulations of the Crab nebula. *Monthly Notices of the Royal Astronomical Society 443*, 1 (07 2014), 547–558.

[42] Purcell, E. M. *Electricity and magnetism / Edward M. Purcell, David J. Morin.*, 3rd ed. ed. Cambridge University Press, Cambridge, 2013.

[43] Ribeyre, X., Tikhonchuk, V. T., and Bouquet, S. Compressible rayleigh–taylor instabilities in supernova remnants. *Physics of Fluids 16*, 12 (2004), 4661–4670.

[44] Rosensweig, R. E. *Ferrohydrodynamics*. Dover Books on Physics. Dover Publications, Newburyport, 2013.

[45] Scase, M. M., Baldwin, K. A., and Hill, R. J. A. Rotating rayleigh-taylor instability. *Phys. Rev. Fluids 2* (Feb 2017), 024801.

[46] Scase, M. M., and Hill, R. J. A. Centrifugally forced rayleigh–taylor instability. *Journal of Fluid Mechanics 852* (2018), 543–577.

[47] Scase, M. M., and Sengupta, S. Cylindrical rotating rayleigh–taylor instability. *Journal of Fluid Mechanics 907* (2021), A33.

[48] Schwartz, L. W. Instability and fingering in a rotating hele–shaw cell or porous medium. *Physics of Fluids A: Fluid Dynamics 1*, 2 (1989), 167–169.

[49] Sharp, D. An overview of rayleigh-taylor instability. *Physica D: Nonlinear Phenomena 12*, 1 (1984), 3–18.

[50] Smirnov, E., Peljo, P., and Girault, H. H. Self-assembly and redox induced phase transfer of gold nanoparticles at a water–propylene carbonate interface. *Chem. Commun. 53* (2017), 4108–4111.

[51] Smith Metal. Polytetrafluoroethylene data sheet. https://www.smithmetal.com/ptfe.htm. Accessed: 22.09.2021.

[52] Snoeijer, J. H., and Andreotti, B. Moving contact lines: Scales, regimes, and dynamical transitions. *Annual Review of Fluid Mechanics 45*, 1 (2013), 269–292.

[53] Taylor, G. I. The instability of liquid surfaces when accelerated in a direction perpendicular to their planes. I. *Proceedings of the London Mathematical Society 201*, 1065 (1950), 192–196.

[54] Waddell, J. T., Niederhaus, C. E., and Jacobs, J. W. Experimental study of rayleigh–taylor instability: Low atwood number liquid systems with single-mode initial perturbations. *Physics of Fluids 13*, 5 (2001), 1263–1273.